Arculus, R.J., Ishizuka, O., Bogus, K., and the Expedition 351 Scientists, 2015
Proceedings of the International Ocean Discovery Program Volume 351
publications.iodp.org

doi:10.14379/iodp.proc.351.103.2015

Site U1438[1]

R.J. Arculus, O. Ishizuka, K. Bogus, M.H. Aljahdali, A.N. Bandini-Maeder, A.P. Barth, P.A. Brandl, R. do Monte Guerra, L. Drab, M.C. Gurnis, M. Hamada, R.L. Hickey-Vargas, F. Jiang, K. Kanayama, S. Kender, Y. Kusano, H. Li, L.C. Loudin, M. Maffione, K.M. Marsaglia, A. McCarthy, S. Meffre, A. Morris, M. Neuhaus, I.P. Savov, C.A. Sena Da Silva, F.J. Tepley III, C. van der Land, G.M. Yogodzinski, and Z. Zhang[2]

Keywords: International Ocean Discovery Program, IODP, *JOIDES Resolution*, Expedition 351, Site U1438, Izu Bonin Mariana, arc origins, subduction initiation, Earth connections, Amami Sankaku Basin, Kyushu-Palau Ridge, basalt, volcanic ash, breccia-conglomerate, biostratigraphy, magnetostratigraphy, oceanic crust, arc basement, Neogene, Paleogene, foraminifers, radiolarians, volcaniclastic, back arc, tuffaceous mud, hemipelagic, East Asian Monsoon, subduction factory

Contents

Background and objectives

Understanding how subduction zones are initiated and continental crust forms in intraoceanic arcs requires knowledge of the inception and evolution of a representative intraoceanic arc, such as the Izu-Bonin-Mariana (IBM) arc system. An intraoceanic setting is mandatory to avoid the obscuring geochemical, geophysical, and structural veils of preexisting continental crust and the practicality of recovery depth of basement cores by drilling. The IBM satisfies these criteria. Understanding the evolution of the IBM system, particularly in the more recent half of its 50 My history, has improved considerably over the past three decades, not the least from studies of ash and other pyroclastic material recovered by ocean drilling. However, we have poorer records for the nature of arc development in the first half of the system's history and very limited understanding of how this (or any other) arc was initiated. International Ocean Discovery Program (IODP) Expedition 351 targeted, in particular, evidence for the earliest evolution of the IBM system following inception.

Site U1438 (proposed Site IBM-1; Figure **F1**) is located in the Amami Sankaku Basin (ASB), <100 km west of the northern portion of the Kyushu-Palau Ridge (KPR). The KPR is a remnant arc of the intraoceanic IBM arc in the western Pacific on the northern part of the Philippine Sea plate. Site U1438 is located at the intersection of two seismic reflection profiles (Lines D98-A and D98-8) obtained by the Japan Oil, Gas, and Metals National Corporation (JOGMEC) (Figures **F2**, **F3**). For a more detailed discussion of the regional setting for Site U1438, see **Regional setting** in the Expedition 351 summary chapter (Arculus et al., 2015b).

Site U1438 was chosen as an ideal location because it fulfilled the following criteria: (1) there are remnants of drillable oceanic crust that existed in the region immediately before arc inception, (2) the initial IBM magmatic record is preserved and includes geological evidence of the tectonic setting at subduction initiation, (3) temporal variations of magmatism in the rear IBM arc are preserved in a sequence of volcaniclastic sediments and tephra, and (4) the effects of along-strike variation are minimized or well understood, which highlights the temporal evolution of the IBM arc crust.

There were two primary targets during Expedition 351: the basement and the overlying sedimentary sequence of Site U1438. Recovering oceanic basement samples allows us to determine the petrological, geochemical, and age characteristics of the pre-KPR (IBM) crust and mantle in the region prior to subduction initiation in the middle Eocene. Overlying sediments preserve a volcanic and geologic record spanning the pre-arc, arc initiation, and remnant arc stages of the IBM. These sediments, combined with basement samples, identify and help model the subduction initiation process and initial arc formation. They also help constrain the geophysical properties of the ASB. Sediment samples permit determination of the Paleogene compositional evolution of the IBM arc and the evolution of the Ryukyu-Kyushu arc, located west of the ASB, through an extensive ash record. The sedimentary record further aids in environmental reconstructions in the western Pacific, including the onset and persistence of the East Asian Monsoon.

During Expedition 351, Site U1438 was cored using all of the IODP coring systems: advanced piston corer (APC), half-length APC, extended core barrel (XCB), and rotary core barrel (RCB). Overall, we accomplished 1611.0 m of penetration, 1461.08 m in the sediment sequence and 150 m into basement. Of the drilled intervals, we recovered 1182 m of sediments and 44 m of basement (see **Operations**).

---

[1] Arculus, R.J., Ishizuka, O., Bogus, K., Aljahdali, M.H., Bandini-Maeder, A.N., Barth, A.P., Brandl, P.A., do Monte Guerra, R., Drab, L., Gurnis, M.C., Hamada, M., Hickey-Vargas, R.L., Jiang, F., Kanayama, K., Kender, S., Kusano, Y., Li, H., Loudin, L.C., Maffione, M., Marsaglia, K.M., McCarthy, A., Meffre, S., Morris, A., Neuhaus, M., Savov, I.P., Sena Da Silva, C.A., Tepley, F.J., III, van der Land, C., Yogodzinski, G.M., and Zhang, Z., 2015. Site U1438. *In* Arculus, R.J., Ishizuka, O., Bogus, K., and the Expedition 351 Scientists, *Proceedings of the International Ocean Discovery Program, Expedition 351: Izu-Bonin-Mariana Arc Origins:* College Station, TX (International Ocean Discovery Program). http://dx.doi.org/10.14379/iodp.proc.351.103.2015

[2] **Expedition 351 Scientists' addresses.**

MS 351-103: Published 25 August 2015

Figure F1. Location map of the Philippine Sea region. The Izu-Bonin and Mariana arcs and associated trenches form the eastern boundary of the Philippine Sea plate. The western boundary includes the Ryukyu-Kyushu and Philippine arcs and trenches. Back-arc basins such as the Shikoku Basin, Parece Vela Basin, and Mariana Trough were created by seafloor spreading between the formerly contiguous remnant arc (Kyushu-Palau and West Mariana Ridges) and eastward-migrating active volcanic arcs, now represented by the Izu-Bonin and Mariana arcs. Site U1438 (pink star) is in the Amami Sankaku Basin.

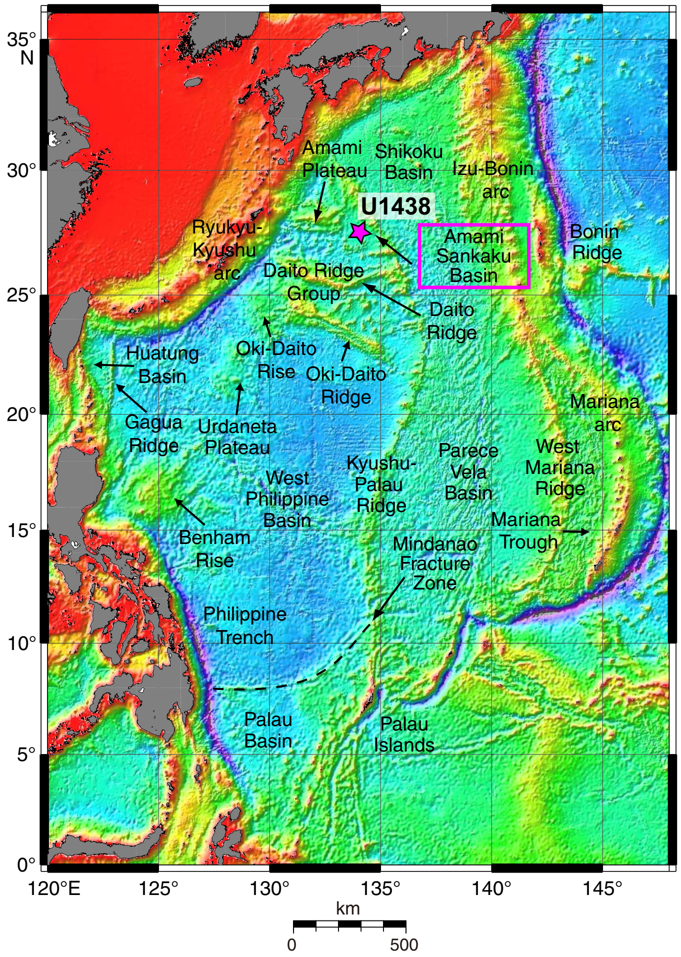

Figure F2. Track map of multichannel seismic survey Lines D98-A and D98-8. Site U1438 is located at the intersection of the two lines.

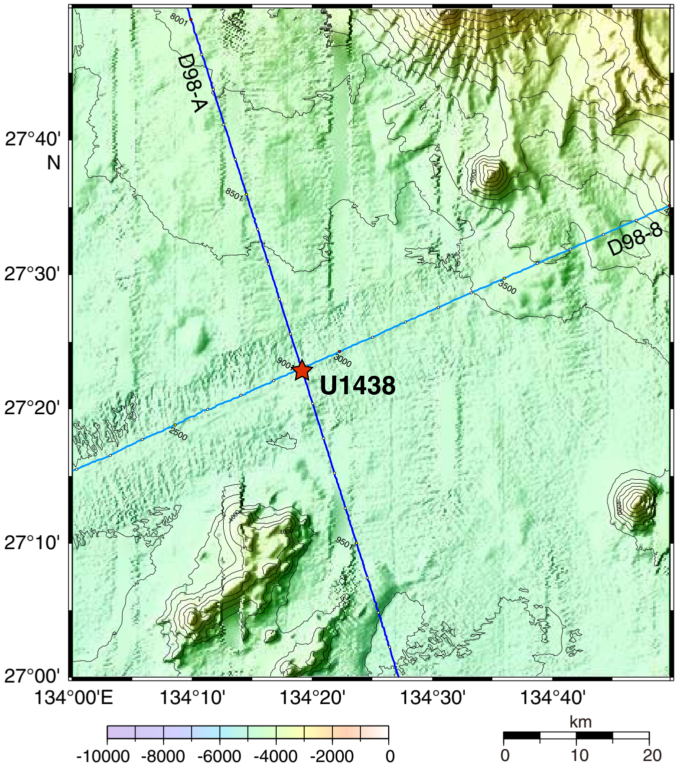

Figure F3. Seismic reflection images, Site U1438. Top two panels comprise MCS Line D98-8 (upper) and interpreted major reflectors (lower). Bottom two panels show MCS Line D98-A (upper) and interpreted major reflectors (lower).

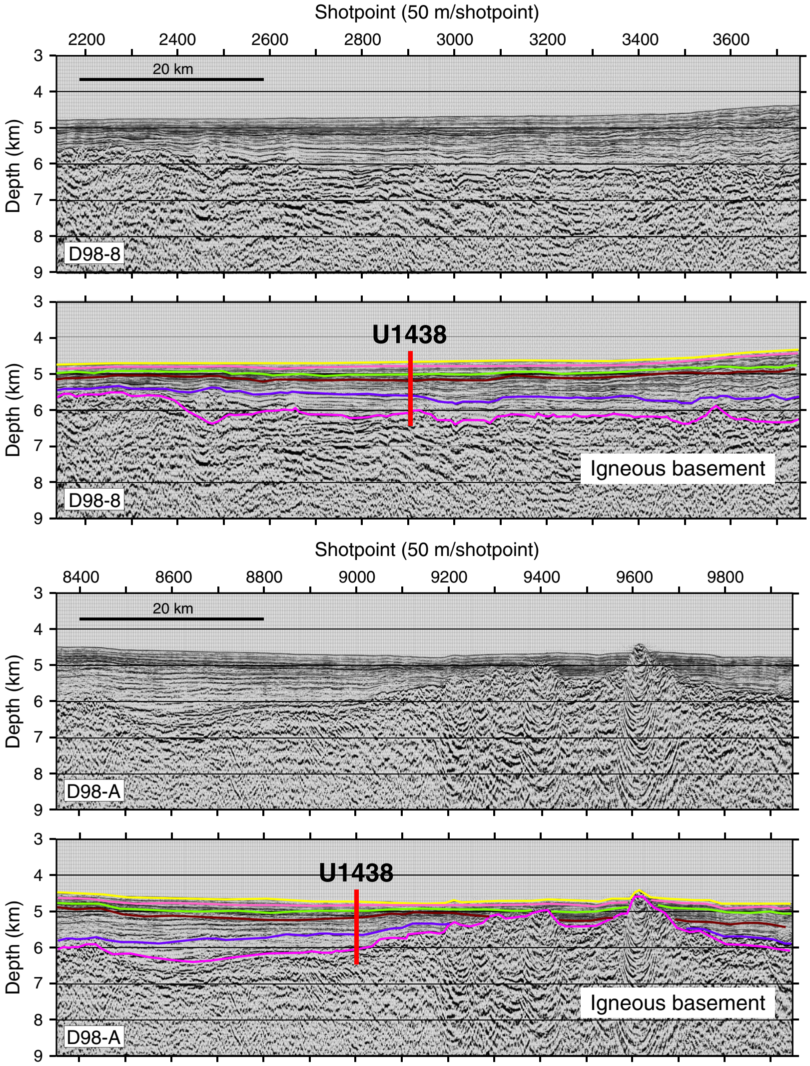

Operations

Transit to Site U1438

Expedition 351 departed from Yokohama, Japan, on 4 June 2014 at 0552 h. The transit was uneventful until we were advised of an immigration issue involving several technicians and scientists. At ~1800 h on 4 June, the ship reversed course and prepared for a rendezvous with a tug boat at 2308 h. Once documents were transferred to allow revision of the passengers' visas, the ship headed back toward Site U1438. The 562 nmi transit to Site U1438 was completed at 0245 h on 7 June, and the ship stabilized over the site location.

Prior to commencing rig floor operations, we conducted a visual seafloor survey using the subsea camera system. We systematically moved in an expanding box pattern out to 50 m using the dynamic positioning console. No seafloor features were observed. At the outer area of the survey, an acoustic positioning beacon was deployed (Falmouth Scientific BAP-547, SN 1008, 15 kHz, 211 dB), and the ship was moved back to the original site coordinates. An observed seafloor tag with the drill string indicated a water depth of 4700 m for the site. Thereafter, the subsea camera system was recovered and preparations for coring were made.

Drilling, coring, and logging operations

The APC, half-length APC, XCB, and RCB systems were all used during Expedition 351. The APC, half-length APC, and XCB systems were used to recover sediment cores in Holes U1438A and U1438B, and the RCB system was used to recover sediment and basement cores in Holes U1438D and U1438E (Table **T1**; Figure **F4**; see Table **T1** in the Expedition 351 summary chapter [Arculus et al., 2015b]).

Hole U1438A

Hole U1438A (27°23.0108′N, 134°19.1020′E) was spudded on 8 June 2014, and three APC cores were recovered to 26.5 mbsf before terminating the hole (at 1400 h). Recovery for the entire hole was

Table T1. Coring summary, Site U1438. (Continued on next three pages.) **Download table in .csv format.**

Core	Date (2014)	Time UTC (h)	Top depth drilled DSF (m)	Bottom depth drilled DSF (m)	Advanced (m)	Recovered length (m)	Curated length (m)	Top depth cored CSF (m)	Bottom depth recovered (m)	Recovery (%)	Sections (*N*)
351-U1438A-											
1H	8 Jun	0215	0	7.5	7.5	7.50	7.50	0	7.50	100	6
2H	8 Jun	0335	7.5	17.0	9.5	7.79	7.79	7.5	15.29	82	8
3H	8 Jun	0445	17.0	26.5	9.5	9.61	9.61	17.0	26.61	101	8
			Hole U1438A totals:		26.5	24.90	24.90				22
351-U1438B-											
1H	8 Jun	0640	0	7.2	7.2	7.26	7.26	0	7.26	101	8
2H	8 Jun	0755	7.2	16.7	9.5	9.09	9.09	7.2	16.29	96	7
3H	8 Jun	0925	16.7	26.2	9.5	9.05	9.05	16.7	25.75	95	7
4H	8 Jun	1045	26.2	35.7	9.5	9.61	9.61	26.2	35.81	101	8
5H	8 Jun	1215	35.7	45.2	9.5	9.26	9.26	35.7	44.96	97	8
6H	8 Jun	1345	45.2	54.7	9.5	9.83	9.83	45.2	55.03	103	8
7H	8 Jun	1507	54.7	64.2	9.5	9.49	9.49	54.7	64.19	100	8
8H	8 Jun	1615	64.2	73.7	9.5	4.48	4.48	64.2	68.68	47	3
9H	8 Jun	1736	73.7	83.2	9.5	9.99	9.99	73.7	83.69	105	8
10H	8 Jun	1845	83.2	92.7	9.5	8.02	8.02	83.2	91.22	84	7
11H	8 Jun	1945	92.7	102.2	9.5	9.57	9.57	92.7	102.27	101	7
12H	8 Jun	2055	102.2	111.7	9.5	9.87	9.87	102.2	112.07	104	8
13H	8 Jun	2200	111.7	121.2	9.5	9.77	9.77	111.7	121.47	103	8
14H	8 Jun	2300	121.2	130.7	9.5	6.73	6.73	121.2	127.93	71	6
15H	9 Jun	0005	130.7	140.2	9.5	9.17	9.04	130.7	139.74	97	7
16H	9 Jun	0110	140.2	149.7	9.5	8.84	8.84	140.2	149.04	93	7
17H	9 Jun	0215	149.7	159.2	9.5	9.44	9.44	149.7	159.14	99	8
18H	9 Jun	0330	159.2	166.7	7.5	7.56	7.56	159.2	166.76	101	6
19H	9 Jun	0445	166.7	168.9	2.2	2.18	2.18	166.7	168.88	99	3
20F	9 Jun	0625	168.9	173.6	4.7	4.84	9.68	168.9	173.74	103	4
21F	9 Jun	0730	173.6	177.8	4.2	4.25	4.25	173.6	177.85	101	4
22F	9 Jun	0855	177.8	180.6	2.8	2.87	2.87	177.8	180.67	103	3
23X	9 Jun	1100	180.6	189.4	8.8	8.92	8.92	180.6	189.52	101	7
24X	9 Jun	1205	189.4	199.1	9.7	4.08	4.08	189.4	193.48	42	4
25X	9 Jun	1315	199.1	208.8	9.7	4.29	4.29	199.1	203.39	44	4
26X	9 Jun	1420	208.8	218.5	9.7	8.46	8.46	208.8	217.26	87	7
27X	9 Jun	1525	218.5	228.2	9.7	5.69	5.69	218.5	224.19	59	4
28X	9 Jun	1640	228.2	237.9	9.7	7.16	7.16	228.2	235.36	74	6
29X	9 Jun	1745	237.9	247.6	9.7	7.74	7.74	237.9	245.64	80	6
30X	9 Jun	1855	247.6	257.3	9.7	9.53	9.53	247.6	257.13	98	8
			Hole U1438B totals:		257.3	227.04	231.75				189
351-U1438C-											
11	10 Jun	0030	0	65	65		***** Jet-in test from 0 to 65.0 mbsf *****				
			Hole U1438C totals:		65						
351-U1438D-											
11	11 Jun	1015	0	219.0	219.0		***** Drilled from 0 to 219.0 mbsf *****				
2R	11 Jun	1120	219.0	228.5	9.5	3.68	3.68	219.0	222.68	39	4
3R	11 Jun	1230	228.5	229.5	1.0	1.66	1.66	228.5	230.16	166	2
4R	11 Jun	1345	229.5	238.2	8.7	2.21	2.21	229.5	231.71	25	3
5R	11 Jun	1445	238.2	247.9	9.7	1.42	1.42	238.2	239.62	15	2
6R	11 Jun	1550	247.9	257.6	9.7	2.13	2.13	247.9	250.25	22	3
7R	11 Jun	1650	257.6	267.3	9.7	2.34	2.34	257.6	259.94	24	3
8R	11 Jun	1755	267.3	277.0	9.7	2.64	2.64	267.3	269.94	27	4
9R	11 Jun	1905	277.0	286.7	9.7	3.76	3.76	277.0	280.76	39	4
10R	12 Jun	0310	286.7	296.4	9.7	4.10	4.10	286.7	290.80	42	4
11R	12 Jun	0435	296.4	306.1	9.7	4.93	4.93	296.4	301.33	51	5
12R	12 Jun	0540	306.1	315.8	9.7	4.29	4.29	306.1	310.39	44	4
13R	12 Jun	0700	315.8	325.5	9.7	7.13	7.13	315.8	322.93	74	6
14R	12 Jun	0825	325.5	335.2	9.7	6.88	6.88	325.5	332.38	71	6
15R	12 Jun	1030	335.2	344.9	9.7	8.28	8.28	335.2	343.48	85	7
16R	12 Jun	1335	344.9	354.6	9.7	9.89	9.89	344.9	354.79	102	8
17R	12 Jun	1500	354.6	364.3	9.7	9.95	9.95	354.6	364.55	103	8
18R	12 Jun	1730	364.3	374.0	9.7	9.70	9.70	364.3	374.00	100	8
19R	12 Jun	1935	374.0	383.7	9.7	7.22	6.91	374.0	380.91	74	6
20R	12 Jun	2135	383.7	393.4	9.7	7.87	7.87	383.7	391.57	81	7
21R	12 Jun	2315	393.4	403.1	9.7	3.91	3.91	393.4	397.31	40	4
22R	13 Jun	0125	403.1	412.8	9.7	10.09	10.09	403.1	413.19	104	8
23R	13 Jun	0315	412.8	422.5	9.7	6.69	6.69	412.8	419.49	69	6
24R	13 Jun	0520	422.5	432.2	9.7	6.18	6.18	422.5	428.68	64	6
25R	13 Jun	0720	432.2	441.9	9.7	8.85	8.85	432.2	441.05	91	7

Table T1 (continued). (Continued on next page.)

Core	Date (2014)	Time UTC (h)	Top depth drilled DSF (m)	Bottom depth drilled DSF (m)	Advanced (m)	Recovered length (m)	Curated length (m)	Top depth cored CSF (m)	Bottom depth recovered (m)	Recovery (%)	Sections (*N*)
26R	13 Jun	0930	441.9	451.6	9.7	8.83	8.83	441.9	450.73	91	8
27R	13 Jun	1120	451.6	461.3	9.7	4.02	4.02	451.6	455.62	41	4
28R	13 Jun	1340	461.3	471.0	9.7	5.90	5.90	461.3	467.20	61	6
29R	13 Jun	1530	471.0	480.7	9.7	10.04	10.04	471.0	481.04	104	8
30R	13 Jun	1745	480.7	490.4	9.7	2.79	2.79	480.7	483.49	29	3
31R	13 Jun	1945	490.4	500.1	9.7	8.74	8.74	490.4	499.14	90	8
32R	13 Jun	2145	500.1	509.8	9.7	9.96	9.96	500.1	510.06	103	8
33R	14 Jun	0025	509.8	519.5	9.7	9.81	9.81	509.8	519.61	101	8
34R	14 Jun	0220	519.5	529.2	9.7	10.02	10.02	519.5	529.52	103	8
35R	14 Jun	0420	529.2	538.9	9.7	9.40	9.40	529.2	538.60	97	8
36R	14 Jun	0605	538.9	548.6	9.7	9.80	9.80	538.9	548.70	101	8
37R	14 Jun	0755	548.6	558.3	9.7	7.17	7.17	548.6	555.77	74	6
38R	14 Jun	0945	558.3	568.0	9.7	7.40	7.40	558.3	565.70	76	7
39R	14 Jun	1140	568.0	577.7	9.7	8.84	8.84	568.0	576.84	91	7
40R	14 Jun	1325	577.7	587.4	9.7	10.00	10.00	577.7	587.70	103	8
41R	14 Jun	1500	587.4	597.1	9.7	10.00	10.00	587.4	597.40	103	8
42R	14 Jun	1700	597.1	606.8	9.7	2.43	2.43	597.1	599.53	25	3
43R	14 Jun	1900	606.8	616.5	9.7	6.02	6.02	606.8	612.82	62	5
44R	14 Jun	2055	616.5	626.2	9.7	8.35	8.35	616.5	624.85	86	7
45R	14 Jun	2245	626.2	635.9	9.7	9.33	9.33	626.2	635.53	96	8
46R	15 Jun	0050	635.9	645.6	9.7	9.44	9.44	635.9	645.34	97	9
47R	15 Jun	0335	645.6	655.3	9.7	7.05	7.05	645.6	652.65	73	6
48R	15 Jun	0535	655.3	665.0	9.7	8.83	8.83	655.3	664.13	91	8
49R	15 Jun	0730	665.0	674.7	9.7	9.34	9.34	665.0	674.34	96	8
50R	15 Jun	0925	674.7	684.4	9.7	8.82	8.82	674.7	683.52	91	8
51R	15 Jun	1115	684.4	694.1	9.7	9.24	9.24	684.4	693.64	95	8
52R	15 Jun	1305	694.1	703.8	9.7	7.33	7.33	694.1	701.43	76	7
53R	15 Jun	1440	703.8	713.5	9.7	9.85	9.85	703.8	713.65	102	9
54R	15 Jun	1635	713.5	723.2	9.7	9.90	9.90	713.5	723.40	102	8
55R	15 Jun	1830	723.2	732.9	9.7	9.99	9.99	723.2	733.19	103	8
56R	15 Jun	2020	732.9	742.6	9.7	8.97	8.97	732.9	741.87	92	8
57R	15 Jun	2240	742.6	752.3	9.7	8.21	8.21	742.6	750.81	85	7
58R	16 Jun	0025	752.3	762.0	9.7	9.67	9.67	752.3	761.97	100	8
59R	16 Jun	0235	762.0	771.7	9.7	9.32	9.32	762.0	771.32	96	7
60R	16 Jun	0445	771.7	781.4	9.7	9.92	9.92	771.7	781.62	102	9
61R	16 Jun	0650	781.4	791.1	9.7	9.23	9.23	781.4	790.63	95	8
62R	16 Jun	0905	791.1	800.8	9.7	8.53	8.53	791.1	799.63	88	7
63R	16 Jun	1130	800.8	810.5	9.7	8.36	8.36	800.8	809.16	86	7
64R	16 Jun	1340	810.5	820.2	9.7	7.87	7.85	810.5	818.35	81	7
65R	16 Jun	1640	820.2	829.9	9.7	8.83	8.83	820.2	829.03	91	8
66R	16 Jun	1845	829.9	839.6	9.7	7.97	7.97	829.9	837.87	82	8
67R	16 Jun	2040	839.6	849.3	9.7	8.25	8.25	839.6	847.85	85	7
68R	16 Jun	2235	849.3	859.0	9.7	9.98	9.98	849.3	859.28	103	9
69R	17 Jun	0030	859.0	868.7	9.7	6.96	6.96	859.0	865.96	72	6
70R	17 Jun	0225	868.7	878.4	9.7	4.61	4.61	868.7	873.31	48	4
71R	17 Jun	0445	878.4	888.1	9.7	5.06	5.06	878.4	883.46	52	5
72R	17 Jun	0710	888.1	897.8	9.7	6.99	6.99	888.1	895.09	72	6
			Hole U1438D totals:		678.8	523.17	522.84				461
351-U1438E-											
11	22 Jun	0300	0	60.1	60.1	0	0	0	0	0	0
21	24 Jun	0540	60.1	613.0	552.9	0	0	60.1	60.10	0	0
31	29 Jun	2325	613.0	867.3	254.3	0	0	613.0	613.00	0	0
4R	30 Jun	0145	867.3	876.8	9.5	4.00	4.00	867.3	871.30	42	4
5R	30 Jun	0400	876.8	886.5	9.7	9.08	9.08	876.8	885.88	94	8
6R	30 Jun	0620	886.5	896.2	9.7	7.32	7.32	886.5	893.82	75	7
7R	30 Jun	0845	896.2	905.9	9.7	9.39	9.39	896.2	905.59	97	8
8R	30 Jun	1130	905.9	915.6	9.7	7.38	7.38	905.9	913.28	76	6
9R	30 Jun	1350	915.6	925.3	9.7	5.45	5.45	915.6	921.05	56	5
10R	30 Jun	1605	925.3	935.0	9.7	9.99	9.99	925.3	935.29	103	8
11R	30 Jun	1830	935.0	944.7	9.7	8.93	8.93	935.0	943.93	92	7
12R	30 Jun	2040	944.7	954.4	9.7	9.92	9.92	944.7	954.62	102	8
13R	30 Jun	2305	954.4	964.1	9.7	8.25	8.25	954.4	962.65	85	7
14R	1 Jul	0125	964.1	973.8	9.7	5.95	5.95	964.1	970.05	61	5
15R	1 Jul	0400	973.8	983.5	9.7	9.04	9.04	973.8	982.84	93	8
16R	1 Jul	0620	983.5	993.2	9.7	8.71	8.71	983.5	992.21	90	7
17R	1 Jul	0850	993.2	1002.9	9.7	8.86	8.86	993.2	1002.06	91	8
18R	1 Jul	1705	1002.9	1012.6	9.7	8.90	8.90	1002.9	1011.80	92	8

Table T1 (continued). (Continued on next page.)

Core	Date (2014)	Time UTC (h)	Top depth drilled DSF (m)	Bottom depth drilled DSF (m)	Advanced (m)	Recovered length (m)	Curated length (m)	Top depth cored CSF (m)	Bottom depth recovered (m)	Recovery (%)	Sections (*N*)
19R	1 Jul	2000	1012.6	1022.3	9.7	9.53	9.53	1012.6	1022.13	98	8
20R	1 Jul	2235	1022.3	1032.0	9.7	8.37	8.37	1022.3	1030.67	86	7
21R	2 Jul	0055	1032.0	1041.7	9.7	9.01	9.01	1032.0	1041.01	93	8
22R	2 Jul	0325	1041.7	1051.4	9.7	9.68	9.68	1041.7	1051.38	100	8
23R	2 Jul	0605	1051.4	1061.1	9.7	9.25	9.25	1051.4	1060.65	95	8
24R	2 Jul	0845	1061.1	1070.8	9.7	7.71	7.71	1061.1	1068.81	79	7
25R	2 Jul	1145	1070.8	1080.5	9.7	8.25	8.25	1070.8	1079.05	85	7
26R	2 Jul	1430	1080.5	1090.2	9.7	5.88	5.88	1080.5	1086.38	61	5
27R	2 Jul	1710	1090.2	1099.9	9.7	9.87	9.87	1090.2	1100.07	102	8
28R	2 Jul	1930	1099.9	1109.6	9.7	9.98	9.98	1099.9	1109.88	103	8
29R	2 Jul	2155	1109.6	1119.3	9.7	9.62	9.62	1109.6	1119.22	99	8
30R	3 Jul	0005	1119.3	1129.0	9.7	9.09	9.09	1119.3	1128.39	94	8
31R	3 Jul	0220	1129.0	1138.7	9.7	9.03	9.03	1129.0	1138.03	93	7
32R	3 Jul	0440	1138.7	1148.4	9.7	6.93	6.93	1138.7	1145.63	71	6
33R	3 Jul	0655	1148.4	1158.1	9.7	9.63	9.63	1148.4	1158.03	99	7
34R	3 Jul	0915	1158.1	1167.8	9.7	9.74	9.74	1158.1	1167.84	100	8
35R	3 Jul	1130	1167.8	1177.5	9.7	9.23	9.23	1167.8	1177.03	95	8
36R	3 Jul	1405	1177.5	1187.2	9.7	8.19	8.19	1177.5	1185.69	84	8
37R	3 Jul	1625	1187.2	1196.9	9.7	9.73	9.73	1187.2	1196.93	100	8
38R	3 Jul	1905	1196.9	1206.6	9.7	8.81	8.81	1196.9	1205.71	91	7
39R	3 Jul	2205	1206.6	1216.3	9.7	4.29	4.29	1206.6	1210.89	44	4
40R	4 Jul	0105	1216.3	1226.0	9.7	4.73	4.73	1216.3	1221.03	49	5
41R	4 Jul	0420	1226.0	1235.7	9.7	4.66	4.66	1226.0	1230.66	48	4
42R	4 Jul	0700	1235.7	1245.4	9.7	2.63	2.63	1235.7	1238.33	27	3
43R	4 Jul	1035	1245.4	1255.1	9.7	5.23	5.23	1245.4	1250.63	54	5
44R	4 Jul	1410	1255.1	1264.6	9.5	7.06	7.06	1255.1	1262.16	74	7
45R	4 Jul	1755	1264.6	1273.8	9.2	6.67	6.67	1264.6	1271.27	73	6
46R	4 Jul	2205	1273.8	1283.0	9.2	5.94	5.94	1273.8	1279.74	65	5
47R	5 Jul	0135	1283.0	1292.2	9.2	7.54	7.54	1283.0	1290.54	82	7
48R	5 Jul	0450	1292.2	1301.4	9.2	4.93	4.93	1292.2	1297.13	54	5
49R	5 Jul	0725	1301.4	1310.6	9.2	2.13	2.13	1301.4	1303.53	23	3
50R	5 Jul	1045	1310.6	1319.8	9.2	1.30	1.30	1310.6	1311.90	14	2
51R	11 Jul	1950	1319.8	1329.5	9.7	2.92	2.92	1319.8	1322.72	30	3
52R	11 Jul	2240	1329.5	1339.2	9.7	4.79	4.79	1329.5	1334.29	49	5
53R	12 Jul	0225	1339.2	1348.9	9.7	2.44	2.44	1339.2	1341.64	25	3
54R	12 Jul	0620	1348.9	1358.6	9.7	3.81	3.81	1348.9	1352.71	39	4
55R	12 Jul	0930	1358.6	1367.8	9.2	4.06	4.06	1358.6	1362.66	44	4
56R	12 Jul	1230	1367.8	1376.9	9.1	1.44	1.44	1367.8	1369.24	16	2
57R	12 Jul	1600	1376.9	1386.2	9.3	2.49	2.49	1376.9	1379.39	27	3
58R	12 Jul	1940	1386.2	1395.7	9.5	1.91	1.91	1386.2	1388.11	20	3
59R	12 Jul	2355	1395.7	1400.3	4.6	1.49	1.49	1395.7	1397.19	32	2
60R	13 Jul	0355	1400.3	1404.9	4.6	1.43	1.43	1400.3	1401.73	31	2
61R	13 Jul	0845	1404.9	1410.3	5.4	3.50	3.50	1404.9	1408.40	65	4
62R	13 Jul	1220	1410.3	1419.5	9.2	2.80	2.80	1410.3	1413.10	30	3
63R	13 Jul	1810	1419.5	1428.7	9.2	2.87	2.87	1419.5	1422.37	31	3
64R	13 Jul	2145	1428.7	1437.9	9.2	4.90	4.90	1428.7	1433.6	53	4
65R	14 Jul	0100	1437.9	1447.1	9.2	2.65	2.65	1437.9	1440.55	29	3
66R	14 Jul	0420	1447.1	1451.7	4.6	2.28	2.28	1447.1	1449.38	50	3
67R	14 Jul	0730	1451.7	1456.3	4.6	2.15	2.15	1451.7	1453.85	47	3
68R	14 Jul	1050	1456.3	1460.9	4.6	3.04	3.04	1456.3	1459.34	66	3
69R	14 Jul	1350	1460.9	1465.5	4.6	1.79	1.79	1460.9	1462.69	39	2
70R	14 Jul	1745	1465.5	1470.1	4.6	1.97	1.97	1465.5	1467.47	43	3
71R	14 Jul	2140	1470.1	1474.7	4.6	3.47	3.96	1470.1	1474.06	75	3
72R	15 Jul	1520	1474.7	1484.4	9.7	1.50	1.74	1474.7	1476.44	15	2
73R	15 Jul	2150	1484.4	1494.1	9.7	1.99	2.48	1484.4	1486.88	21	2
74R	16 Jul	450	1494.1	1503.8	9.7	1.56	1.74	1494.1	1495.84	16	2
75R	16 Jul	1005	1503.8	1506.8	3.0	0.96	1.10	1503.8	1504.9	32	1
76R	16 Jul	1725	1506.8	1510.8	4.0	3.48	3.97	1506.8	1510.77	87	3
77R	16 Jul	2130	1510.8	1515.4	4.6	2.44	2.83	1510.8	1513.63	53	3
78R	17 Jul	0150	1515.4	1524.5	9.1	4.36	4.83	1515.4	1520.23	48	4
79R	17 Jul	0655	1524.5	1533.6	9.1	3.80	4.32	1524.5	1528.82	42	4
80R	17 Jul	1405	1533.6	1542.9	9.3	1.78	1.93	1533.6	1535.53	19	2
81R	17 Jul	2240	1542.9	1552.0	9.1	1.50	1.97	1542.9	1544.87	16	2
82R	18 Jul	0410	1552.0	1561.4	9.4	3.07	3.54	1552.0	1555.54	33	3
83R	19 Jul	0020	1561.4	1571.1	9.7	2.63	3.29	1561.4	1564.69	27	3
84R	19 Jul	0735	1571.1	1579.1	8.0	0.78	1.01	1571.1	1572.11	10	1
85R	19 Jul	1450	1579.1	1584.9	5.8	1.00	1.50	1579.1	1580.60	17	1

Table T1 (continued).

Core	Date (2014)	Time UTC (h)	Top depth drilled DSF (m)	Bottom depth drilled DSF (m)	Advanced (m)	Recovered length (m)	Curated length (m)	Top depth cored CSF (m)	Bottom depth recovered (m)	Recovery (%)	Sections (*N*)
86R	19 Jul	2345	1584.9	1594.0	9.1	1.61	2.14	1584.9	1587.04	18	2
87R	20 Jul	0915	1594.0	1603.1	9.1	2.96	3.28	1594.0	1597.28	33	3
88R	20 Jul	1530	1603.1	1611.0	7.9	1.3	1.50	1603.1	1604.60	16	1
				Totals:	1611	450.73	457.67				413
351-U1348F-											
11	24 Jul	1000	0	700	700			***** Dedicated logging hole *****			
				Hole U1438E totals:	700						
				Site U1438 totals:	3557.6	1225.84	1237.16				1085

Figure F4. Hole configuration, Site U1438.

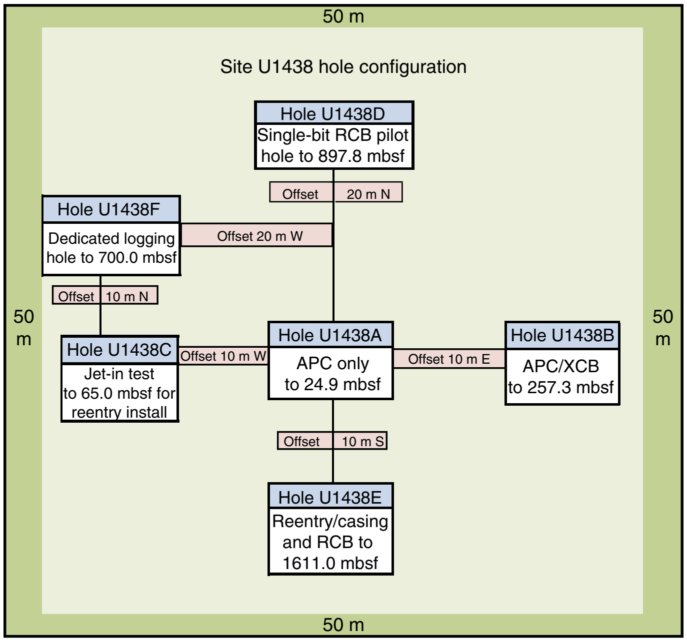

94% (24.9 m recovered). This hole was intended only to gain additional material for higher resolution sampling of the upper 20 m, so no discrete samples were taken for shipboard analyses.

Hole U1438B

The ship was offset 10 m east of Hole U1438A, and Hole U1438B (27°23.0111′N, 134°19.1087′E) was spudded on 8 June 2014. Six successful temperature measurements were taken using the advanced piston corer temperature (APCT-3) tool on Cores 3H, 4H, 5H, 6H, 7H, and 9H at 26.2, 35.7, 45.2, 54.7, 64.2, and 83.2 mbsf, respectively. Oriented APC coring continued in this hole through Core 19H to 168.9 mbsf. Incomplete strokes on the last two core barrels and 65,000 lb of overpull indicated that APC refusal had been reached. The unoriented half-length APC coring system was then used to recover Cores 20F through 22F (to 180.6 mbsf) before refusal, after which the XCB coring system was used. XCB coring (9–10 June) continued until the decision was made to terminate the hole in the interest of time. XCB coring ended with Core 30X (257.3 mbsf). In total, 19 full-length APC cores were recovered (168.9 m penetration; 159.2 m recovered; 94.2% recovery), 3 cores were collected with the half-length (4.7 m core barrels) APC (11.7 m penetration; 11.96 m recovered; 102% recovery), and 8 cores were recovered with the XCB (76.6 m penetration; 55.9 m recovered; 73% recovery). Overall recovery for the hole was 227.04 m (88%).

Hole U1438C

The ship was then offset 20 m west of Hole U1438B (and thus 10 m west of U1438A) for the reentry cone jet-in test (Hole U1438C; 27°22.9963′N, 134°19.0883′E). Controlled jetting reached 65.0 mbsf in ~2.5 h. After successfully completing the jet-in test, the bit was pulled clear of the seafloor and Hole U1438C concluded on 11 June 2014.

Hole U1438D

Hole U1438D (27°23.0218′N, 134°19.1023′E) was intended as the pilot hole for reentry operations. It was spudded on 11 June 2014 and drilled without coring to 219 mbsf. Coring began with nonmagnetic core barrels to 286.7 mbsf and recovered up to Core 9R before coring was halted on 12 June. At this point, the weather had deteriorated significantly; a forecasted low-pressure system was upgraded to a full-blown tropical storm and passed directly over the site. RCB coring resumed later the same day and continued until 17 June to a total depth of 897.8 mbsf with the recovery of Core 72R. In all, 71 cores were collected over a cored interval of 678.9 m, totaling 523.2 m of material (77% recovery).

The hole was surprisingly stable with no detected fill on connections, overpull, or drag. As a result of the excellent hole conditions, a single casing string (10.75 inches) was deemed necessary for the reentry hole (Hole U1438E). The hole was then swept and displaced with heavy mud in preparation for wireline logging. Before logging, however, the drill string was raised to 304 mbsf and a free-fall funnel (FFF) was deployed as a contingency plan if the reentry hole (U1438E) encountered problems. After releasing the bit on the seafloor, the hole was reentered and the end of the drill string was positioned at logging depth (95 mbsf). Rig-up of the first tool string began on 19 June. The triple combination (triple combo) tool string, measuring temperature, resistivity, density, porosity, and natural gamma (see **Physical properties and downhole measurements**), downlog reached 303 mbsf, where the tool string encountered a bridge. As the depth of the obstruction corresponded to the depth of the pipe during deployment of the FFF, it was concluded that the pipe itself created the bridge. An attempt to pursue further logging operations was organized. The pipe was lowered to 328.15 mbsf (below the bridge), and the triple combo tool string was run back into the hole. Unfortunately, another bridge was encountered at 362 mbsf. Because of the difficulty of passing through the bridge and the shallow depth, it was decided to stop logging operations for Hole U1438D. No uplog was recorded for the second phase of logging, and the seafloor was cleared on 20 June. Hole U1438D officially ended on 20 June.

Hole U1438E

Hole U1438E (27°23.0153′N, 134°19.0898′E) was spudded on 21 June 2014 when the reentry cone and casing assembly was jetted-in to 60.1 mbsf. Afterward, a 14.75 inch hole was drilled to 613.0 mbsf, finishing on 24 June. The hole was swept multiple times with high-viscosity sepiolite mud, and only one wiper trip was conducted because of the good borehole conditions. On 25 June, preparations began for making up and deploying the 10.75 inch casing string. On 27 June, the 10.75 inch casing string was lowered into the hole to 605 mbsf escorted by a mud motor–powered underreamer and a 9.875 inch tricone pilot bit. Drilling then continued to 867.3 mbsf with the RCB center bit.

At 0900 h on 30 June, RCB coring began in Hole U1438E. Coring continued to 1319.8 mbsf. Coring stopped at 1825 h on 5 July because of impending severe weather. A super typhoon (Neoguri) necessitated our transit to a safe standby location east of Site U1438. At 0600 h on 7 July, the ship was positioned 144 nm east of Site U1438. Upon arriving back on site at 0830 h on 10 July, we continued to wait for sea conditions to moderate enough to resume operations. At 1315 h on 11 July, we deployed the subsea camera system, and Hole U1438E was reentered at 1655 h. RCB coring resumed with nonmagnetic core barrels on 12 July. Coring continued to 1461 mbsf, where the sediment/basement contact was identified (top of Core 69R). RCB coring continued through basaltic basement rocks to a total depth for the hole, and site, of 1611 mbsf. In total, 85 RCB cores were recovered from this hole. For a total of 743.7 m cored, 450.73 m was recovered (61%). More specifically, 407 m of sediment was recovered from 593.6 m cored (69%), and 44 m of basement was recovered from 150 m cored (29%).

In general, coring conditions were good, but there were several times when remedial hole conditioning was required. The sediment/basement contact was the depth at which the drill string had the most trouble rotating. As a result, a wiper trip was conducted prior to wireline logging operations. Heavy mud was not used, as it was suspected to have affected conditions in Hole U1438D. The drill pipe was pulled to 190 mbsf (inside the casing), and the triple combo was readied. Because of the difficult hole conditions, the radioactive source was removed and a “hole finder” was attached at the bottom of the tool string. The triple combo was deployed and reached 1186 mbsf, where it encountered a bridge and was unable to pass after several attempts. During the uplog, caliper measurements indicated that the hole diameter was >18 inches for the entire logged depth. This precluded the use of the vertical seismic imager (VSI) and Formation MicroScanner–sonic (FMS-sonic) tool strings. However, the Göttingen Borehole Magnetometer (GBM) is not affected by borehole diameter. The GBM was deployed and reached the same total depth as the triple combo (1186 mbsf). Logging operations were completed and the hole was terminated on 22 July.

Hole U1438F

Hole U1438F (27°23.0167′N, 134°19.0905′E), offset 10 m north of Hole U1438C and 20 m west of Hole U1438A, was a dedicated wireline logging hole. The hole was drilled to 700 mbsf, and logging operations began on 25 July. Hole preparation for logging included a wiper trip and circulation with seawater, after which the pipe was pulled to 95 mbsf. The triple combo began a downlog on 25 July. The triple combo reached ~700 mbsf and began an uplog. The triple combo was recovered on 26 July, after which the VSI was run to take advantage of full daylight hours. The VSI was rigged up and deployed. Protected species observation began at sunrise (~0500 h), and ramp-up of the air guns began 1 h later, as no protected species were observed in the 940 m diameter exclusion zone for this site. The air guns fired every 5–10 min. The VSI took measurements at nine stations on the uplog. The last deployment was the FMS-sonic tool string to 689 mbsf. Logging operations were completed late on 26 July. With the recovery of the drill string on 27 July, operations for Expedition 351 concluded.

Lithostratigraphy

During Expedition 351, Site U1438 was drilled in the ASB primarily to investigate the sedimentary record of Izu-Bonin arc initiation and the nature of the underlying oceanic basement. The lithostratigraphic record at this site is composed of sediment, sedimentary rocks, and igneous rocks recovered in Holes U1438A, U1438B, U1438D, and U1438E.

Sediments and sedimentary rocks at Site U1438 were sampled from the seafloor to 1461 mbsf (Figure **F5**) and are divided into four lithostratigraphic units. The thin upper sediment layer at Site U1438, Unit I, is primarily terrigenous and volcaniclastic mud with interspersed ash layers, as well as rare biogenic ooze layers. The much thicker, underlying sedimentary section is split into three units based on textural attributes, degree of lithification, and proportions of rock types. Unit II sedimentary rocks are tuffaceous mudstone and fine sandstone with localized moderate to intense deformation. Unit III sedimentary rocks are on average coarser grained than those of Unit II, including tuffaceous mudstone, tuffaceous sandstone, and conglomerate with volcanic and rare sedimentary clasts commonly up to pebble and rarely cobble size. A diverse suite of sedimentary rocks comprises Unit IV, including medium to coarse sandstone, siltstone, and mudstone with radiolarians, together with three 10–20 cm intervals of igneous rock.

Approximately 150 m of igneous basement rock was cored beneath the sedimentary rocks of Unit IV. This interval was described as a single basement Unit 1 composed of sparsely vesicular, microcrystalline to fine-grained, aphyric to sparsely porphyritic basalt.

Unit I (Holes U1438A and U1438B)

Intervals: 351-U1438A-1H-1, 0 cm, to 3H-CC, 60 cm (all of Hole U1438A); 351-U1438B-1H-1, 0 cm, to 18H-1, 109 cm
Thickness: 160.3 m
Depths: Hole U1438A = 0–24.9 mbsf; Hole U1438B = 0–160.3 mbsf
Age: recent to latest Oligocene (Pleistocene in Hole U1438A)
Lithology: tuffaceous mud, mud with ash, mud, and clay with some discrete ash beds

Unit I sediments were identified in the combined records of Hole U1438A and the upper part of Hole U1438B. A total of 24.9 m of sediment was recovered in Hole U1438A. The first two sections of Core 351-U1438A-1H, at and within the first few meters below the mudline, were soupy with high water content, below which relatively intact sediments were recovered. The ship was offset 10 m east, and a total of 257 m of sediment and sedimentary rocks were drilled in Hole U1438B. In this second hole, significant downhole changes in grain size, lithification, and degree of bioturbation were observed in the recovered section deeper than that reached at the bottom of Hole U1438A, and these changes continue into Hole U1438D, drilled 20 m north (Figure **F6**). These observations allow division of the upper part of the section at Site U1438 into two major stratigraphic units, Units I and II (Table **T2**).

Figure F5. Lithostratigraphic overview of Site U1438, including sediment and sedimentary rock lithostratigraphic Units I–IV and oceanic igneous basement Unit 1. Maximum bedding thickness corresponds to the thickest graded bed present in each core as determined by visual observation: *** = >1 m, ** = 1–0.3 m, * = <0.3 m. # = no reliable estimates because of unconsolidated sediment, drilling disturbance, and/or faulting. Bed width corresponds to the average grain size averaged over 5 m bins. Average grain size is for 5 m thick intervals. Owing to 5 m bin size, features on the order of core section length may not be evident. Grain size classes: Cl = clay, Si = silt, Vfs–fs = very fine and fine sand, Ms–vcs = medium to very coarse sand, Gr = granules.

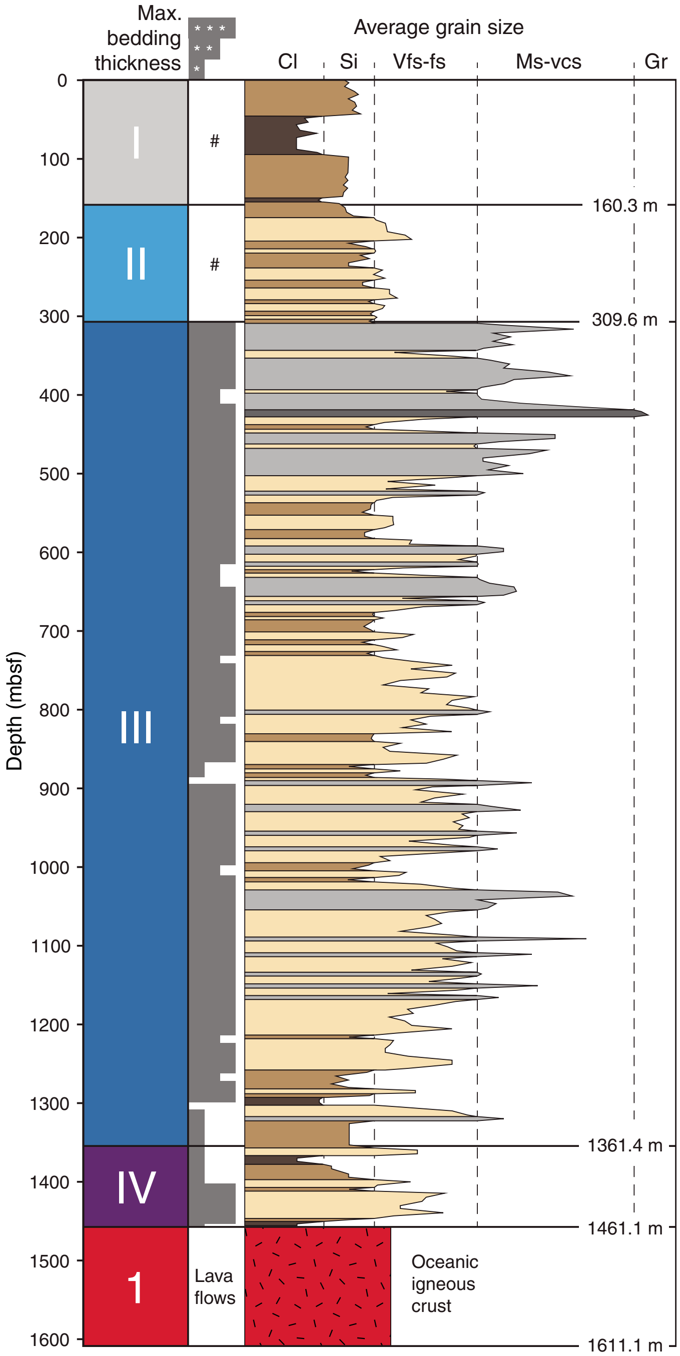

Figure F6. Downhole plots of modal grain size, degree of bioturbation, sedimentary structures and bedding orientation, using data from Holes U1438B and U1438D. Characteristics were averaged over 2 m intervals, which may mask features on the order of core section length.

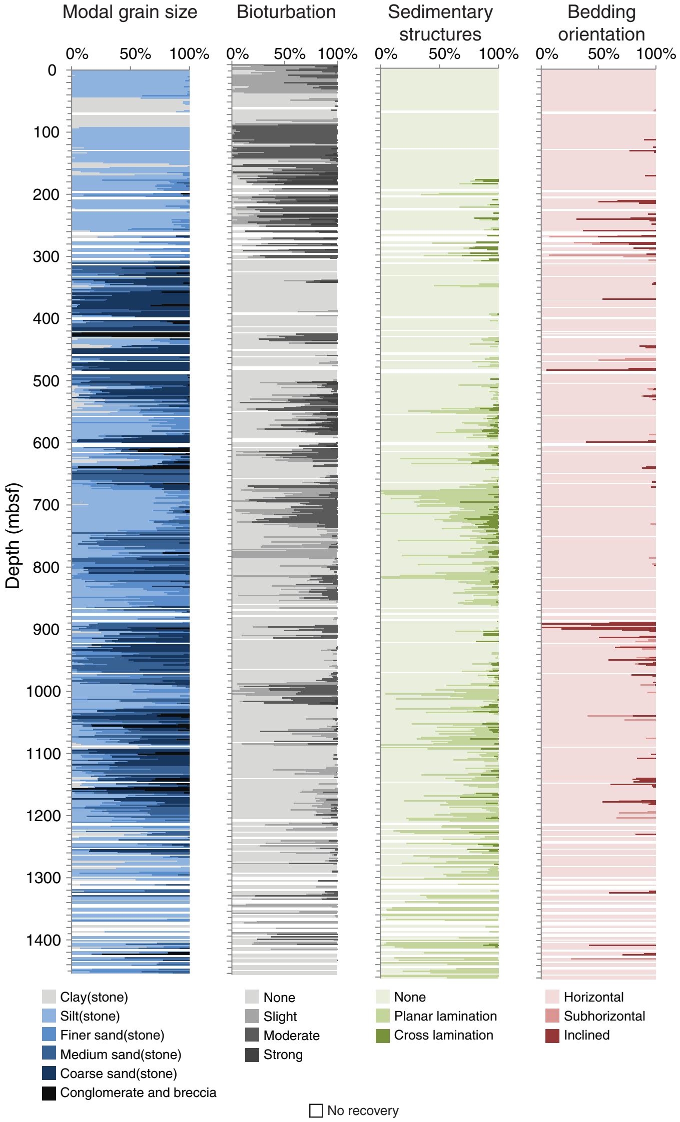

Description

The cores from Holes U1438A and U1438B that make up Unit I consist of a range of fine-grained sediments from pelagic and hemipelagic to volcaniclastic in origin. Based on color and textural variations in the sediments and smear slide analysis of selected sediment intervals, Unit I has been broadly divided into two parts: an upper mud interval with a significant biogenic component and a lower mud interval that transitions downhole into hemipelagic clay near the contact with Unit II (Figures **F6**, **F7**; Table **T2**). Superimposed on this change in background sedimentation is variable ash content, resulting in both discrete ash layers and intervals with disseminated ash. Hole U1438A cores comprise solely muddy sediment with a biogenic component, whereas in Hole U1438B, such sediments extend to 28.6 mbsf at the base of tuffaceous foraminifer ooze in Section 351-U1438B-4H-2, 90 cm. These sediments have been slightly to moderately mixed by burrowing organisms, resulting in various degrees of bioturbation throughout the cored interval.

The pelagic biogenic components in the upper muddy interval are dominantly siliceous in Cores 351-U1438A-1H and 351-U1438B-1H, ranging up to 22% in some intervals; radiolarians are most abundant with fewer diatoms, sponge spicules, and silicoflagellates. This composition is reflected in the nomenclature used to

Table T2. Lithostratigraphic summary, Site U1438. **Download table in .csv format.**

Lith. unit	Age	Interval	Depth (mbsf)	Lithologies (decreasing order of importance)
		351-		
I	recent to latest Oligocene (Pleistocene in Hole U1438A)	U1438A-1H-1, 0 cm, to U1438A-3H-CC, 60 cm U1438B-1H-1, 0 cm, to U1438B-18H-1, 110 cm	0–26.5 0–160.3	Major: tuffaceous mud, mud with ash, mud, clay, ash Minor: radiolarian-rich mud, foraminifer ooze, foraminifer mud (found in Cores 351-U1438A-1H, 2H, and 3H and 351-U1438B-1H, 2H, 3H, and 4H)
II	Oligocene	U1438B-18H-1, 109 cm, to U1438B-30X-CC, 29 cm	160.3 –257.3	Major: tuffaceous mudstone, siltstone, and fine sandstone with nannofossils, nannofossil mud, and mudstone
		U1438D-2R-1, 0 cm, to U1438D-12R-3, 75 cm	219.0 – 309.6	Minor: ash, tuff, sandy mud/silt, clay; zone of soft-sediment deformation at base of Hole U1438B and top of Hole U1438D
III	Oligocene to Eocene	U1438D-12R-3, 75 cm, to U1438D-72R-CC, 35 cm U1438 E-4R-1, 0 cm, to U1438E-55R-3, 5 cm	309.6–895.1 867.3–1361.35	Major: tuffaceous sandstone, tuffaceous breccia-conglomerate Minor: tuffaceous siltstone, tuffaceous mudstone, tuff
IV	Eocene	U1438E-55R-3, 5 cm, to U1438E-69R-1, 18 cm	1361.35–1461.08	Major: mudstone with radiolarians, tuffaceous siltstone and sandstone Minor: breccia-conglomerate, basaltic andesite
1	Eocene(?)	U1438E-69R-1, 18 cm, to U1438E-88R-1, 150 cm	1461.08–1611.0	Major: basalt Minor: limestone

Figure F7. Overview of component proportions for Units I and II based on smear-slide data (see Smear slides in **Core descriptions**).

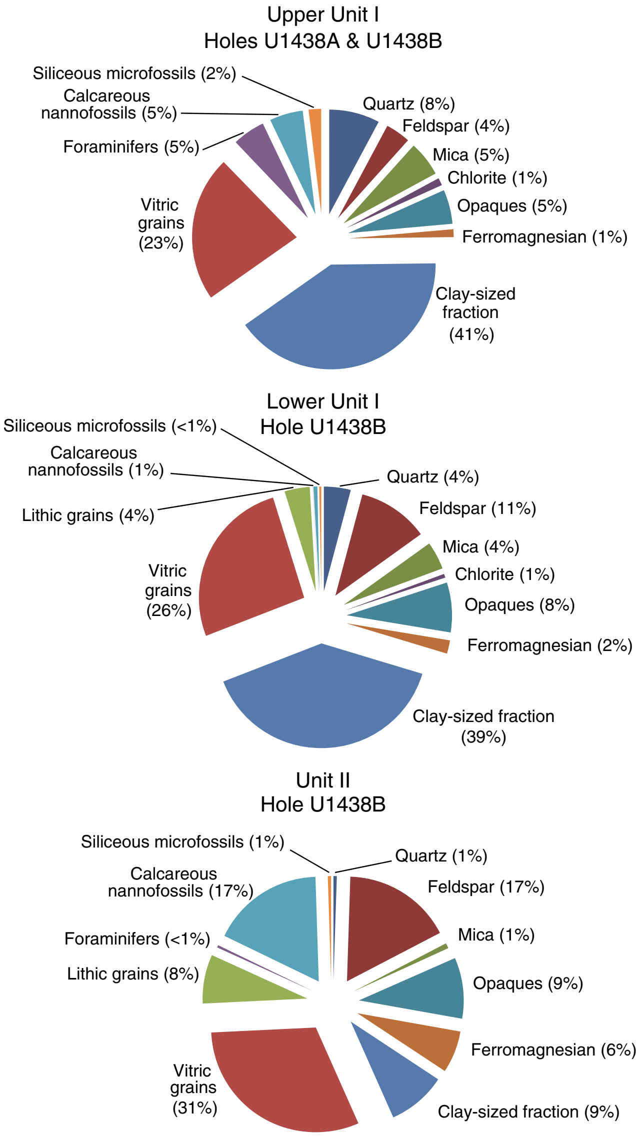

Figure F8. Upper contact between tuffaceous foraminifer ooze layers and overlying mud in correlative beds in Holes U1438A (left) and U1438B (right). Note the soupy texture of the ooze in each core and the large dark scoria clast in the Hole U1438B deposit.

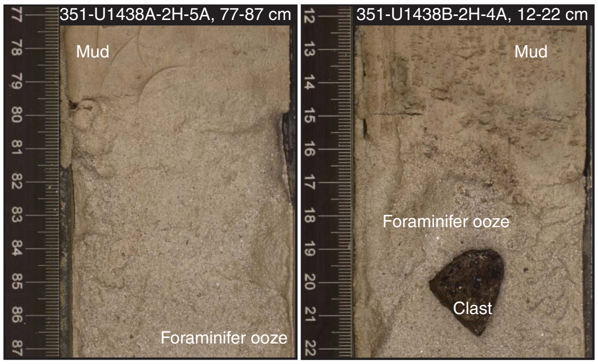

describe the core (see **Lithostratigraphy** in the Expedition 351 methods chapter [Arculus et al., 2015a]) with the modifier "radiolarian-rich" or suffix "with radiolarians" used in several intervals. In Cores 351-U1438A-2H and 351-U1438B-2H, the pelagic biogenic components are dominant over the terrigenous and volcaniclastic components, particularly in the lighter colored layers, where foraminifers and nannofossils compose 32%–60% of the sediments (see **Geochemistry** carbonate content), and are classified as foraminifer/nannofossil mud or foraminifer ooze, respectively (Figure **F8**). There are also traces (up to <1%) of organic matter, spores, and plant remains preserved in Core 351-U1438A-1H (see Smear slides in **Core descriptions**).

The color of the biogenic muddy intervals exhibits rhythmic alternation between more brownish (moderate yellowish brown, 10YR 5/4, to pale yellowish brown, 10YR 6/2) and greenish gray (light olive-gray, 5Y 5/2) colors at a meter to decimeter scale. These color variations become more pronounced downhole through the three Hole U1438A cores and are particularly distinct in Core 351-U1438A-3H, where smear slide analysis of the end-members indicates no observable differences in their mineralogical compositions (see discussion below). The color changes are gradational and may reflect the addition of trace amounts of Fe oxides in the brown intervals, perhaps due to the oxidation state of iron.

The lower muddy sediments are primarily composed of tuffaceous mud, mud with ash, mud, and clay, with some discrete ash beds (Figure **F9**). There are traces of sponge spicules and radiolarian fragments in a few smear slides in the uppermost section of Core 351-U1438B-15H, but no biogenic sediment modifiers were used in their description. The rhythmic alternation between more olive-gray (5Y 5/2) or yellowish brown (10YR 4/2) to moderate yellowish brown (10YR 5/4) sediment at meter to decimeter scale continues, albeit in a more inconsistent fashion, through Core 351-U1438B-9H. Core 10H is fairly uniform moderate yellowish brown (10YR 5/4) with slightly darker sections being more clay rich than lighter colored intervals, as shown by smear slides from these intervals. From Core 11H to the top of 18H, the sediment becomes progressively darker, with distinctly lighter intervals and burrow fills. Reaction with hydrogen peroxide indicates the presence of Mn oxides in the core. These Mn oxides in the lower section impart a dark yellowish brown (10YR 4/2) to dusky yellowish brown (10YR 2/2) color to the mud. The lighter intervals and regions of the core in this lower section are in some cases rich in ash or are composed of mud or clay without the Mn oxide stain.

The lower interval of muddy sediment locally exhibits slight to moderate bioturbation. Bioturbated intervals are rare in Cores 351-U1438B-4H through 10H and common in Cores 11H through 18H (Figure **F6**). It is likely that intervals where no discrete burrows were noted may instead be thoroughly homogenized by burrowing organisms. The contacts change from more gradational in the upper cores (4H through 13H) to more bioturbated in the lower part (Cores 14H through 18H). The sharp contacts are commonly associated with variations in ash or clay content. Discrete burrows and bioturbated contacts may be more recognizable where the color contrast between alternating muds is strongest. Some burrows filled by ash are noted as "ash pods" in the core. There is one thicker ash bed that shows normal grading and fining upward in Core 351-U1438B-16H (Figure **F9**).

Representative X-ray diffraction (XRD) patterns of samples from Cores 351-U1438B-1H through 17H (Figure **F10**) illustrate the variation in mineral composition throughout Unit I. The relative abundances of minerals present in bulk samples from Cores 351-U1438B-1H through 10H, which were modeled from the XRD data, are shown in Table **T3**. These model results indicate that the mud samples are dominated by quartz, plagioclase feldspar, chlorite (clinochlore), and an undifferentiated mixture of sheet silicate minerals (muscovite; illite + other clays). Significant calcite is evident in only one of the analyzed samples, near the top of Hole U1438B at 10.5 mbsf (Sample 351-U1438B-2H-3, 42–44 cm). Small quantities of halite also appear to be present in several samples.

No difference in mineralogy between the yellowish brown and gray-green muds in the lower sediments is revealed in the XRD data, but samples from the muddy intervals deeper than Core 351-U1438B-10H have progressively less variable and lower quantities of quartz (Figures **F10**, **F11**). The compositions of plagioclase feldspars present in lower Hole U1438B mud samples also appear to be more variable and more calcic than in shallower parts of the core, where database searches returned primarily albite. Samples deeper than Core 10H appear to have higher quantities of clay and zeolite minerals, which produce a broad peak at less than 8°2θ. Database searches appear to confirm the presence of clinoptilolite and phillipsite in lower Unit I mud samples, but other zeolite minerals may also be present. Because the clay and zeolite minerals have not been thoroughly characterized, the mineralogy of mud samples from Cores 11H through 17H is not well constrained and was not modeled.

Figure F9. Lower part of Unit I. Left: light-colored ash pods in a variegated, bioturbated mud. Right: lighter ash layer with a sharp basal contact with underlying dark brown mud, which grades into slightly bioturbated tuffaceous mud and then moderately bioturbated mud.

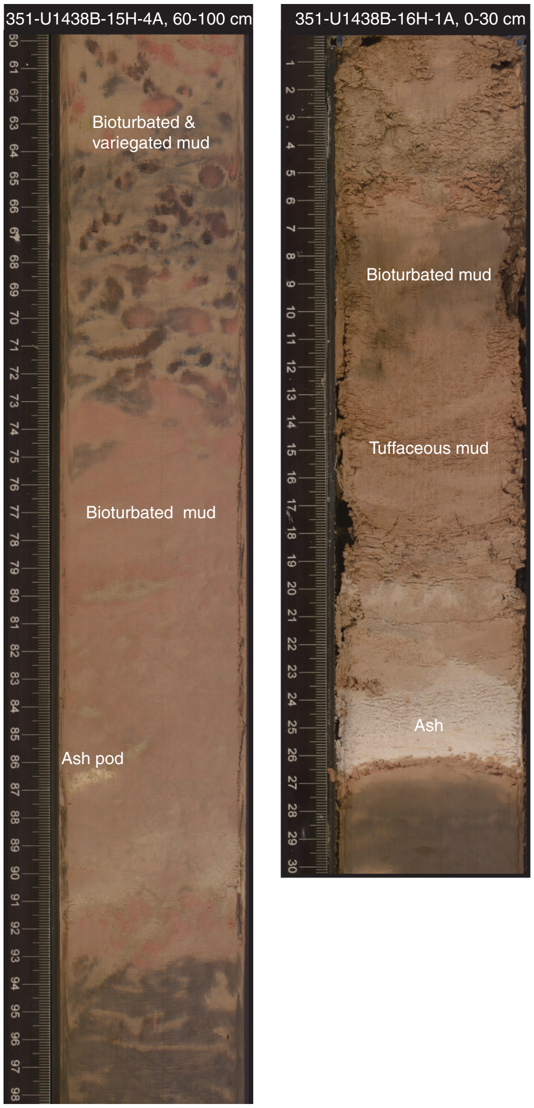

Potential authigenic mineral phases include fine (<63 µm) euhedral opaque minerals locally concentrated in darker mud intervals and ash layers. Magnetic susceptibility data suggest that these are Fe-bearing minerals or mineral mixtures (see **Physical properties and downhole measurements**). Mn enrichment at the bottom of Unit I culminates in Section 351-U1438B-17H-3, where small (<1 cm) Mn nodules were noted. The first occurrence of zeolite minerals was noted in a smear slide from Sample 351-U1438B-11H-5, 138 cm. In this core, there are also minor amounts of rhombic authigenic carbonate and opaque minerals. These increase in Sample 351-U1438-12H-3, 75 cm, where a smear slide contains authigenic carbonate (3%), zeolites (trace), and clay minerals (1%). Authigenic clay minerals are in the form of birefringent rims on silt grains. In Sections 14H-1 through 14H-3, several layers are interpreted as altered ash, where the vitric component had been replaced by clay minerals and/or zeolites. Faint Fe-rich circular features in one sample (351-U1438B-14H-1, 125 cm) may be hydration rims in former vesicular glass.

Figure F10. X-ray diffractograms for mud lithologies in cores through Unit I, Hole U1438B. Prominent peaks include quartz (Qz), plagioclase (P), muscovite + illite (M + I), chlorite (C), chlorite + zeolite minerals (C & Z), and calcite (Ca), which produce a broad peak at low 2θ angles for many samples collected in Cores 351-U1438B-11H through 17H.

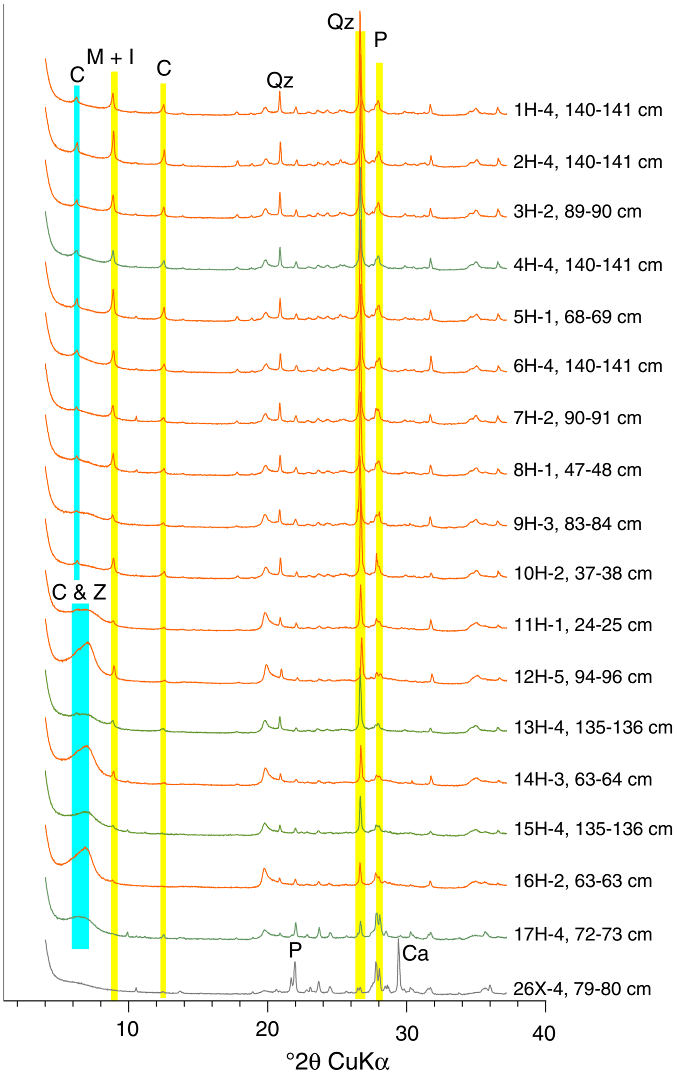

Table T3. Results of modeled XRD data (semi-quantitative, expressed as relative abundances totaling 1.00), Hole U1438B. **Download table in .csv format.**

Volcanic ash is concentrated in several discrete layers (Table **T4**), ranging in thickness from 1 to 13 cm and in grain size up to lapilli (e.g., ~2 mm in Core 14H). In addition to discrete ash layers, we observed significant but variable downcore amounts of disseminated ash in mud intervals as noted in the visual core descriptions (VCDs). In discrete ash beds, the bases are often sharp, with tops grading into tuffaceous or bioturbated mud (Figures **F9**, **F12**). The ash-dominated intervals exhibit a range of colors from pale red (10R 6/2) in Core 351-U1438B-4H, to yellowish brown (10YR 6/2, 10YR 5/4, 10Y 4/2), to shades of gray (N8, 5Y 5/2, 5YR 5/2) through Core 13H, and then, in underlying cores, locally becomes more pinkish (5YR 7/2). In Core 14H, ash-bearing intervals are composed of a complex alternation of ash beds and tuffaceous muds.

Figure F11. Intensity of quartz peaks at 26.6°2θ for Unit I mud samples, Hole U1438B. The downhole decrease in variability and intensity of quartz peaks in XRD scans correspond to downhole changes in the color of Unit I mud and the transition from hemipelagic mud to deep-sea clay.

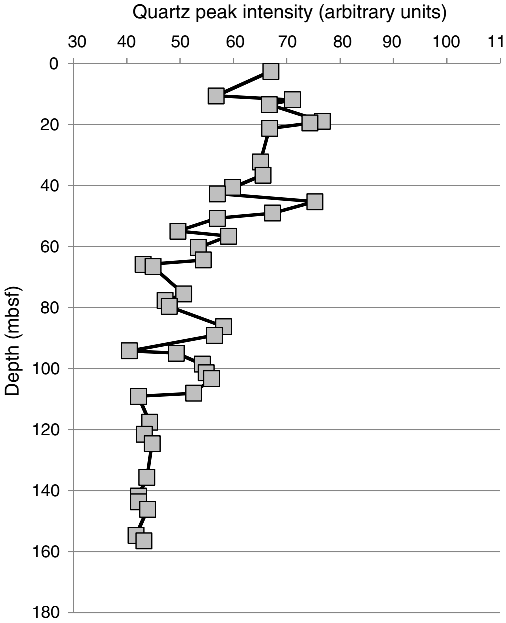

Table T4. Occurrence of ash/tuff layers in Units I, II, and III, in Holes U1438A, U1438B, and U1438D as determined from a combination of visual description, smear slide (SS), and/or thin section (TS) analysis, and intensity of magnetic susceptibility (MS) measurements. **Download table in .csv format.**

The pyroclastic components are dominantly colorless vitric pumice and shards with traces of brown vitric fragments. Phenocrysts and isolated volcanogenic crystals were noted by smear slide examination using transmitted light microscopy as well as by observation of the >63 µm and chemically leached clay-free fraction of the core catcher samples used by the radiolarian specialist. These include pyroxene, opaque minerals, plagioclase, minor biotite, and quartz. Some ash fractions are notably enriched in lithic fragments and crystals. It is possible that the less robust vitric components have been entirely dissolved, as we observed abundant zeolites in many of the ash-rich beds (e.g., Sample 351-U1438B-11H-5, 138 cm). As there are muddy intervals with crystals but lacking distinct vitric components (e.g., mud with crystals in Core 10H), it is uncertain if glass was present but has been dissolved (see below and **Geochemistry**).

Correlation between holes

The top two cores of Hole U1438B are essentially the same part of the stratigraphy encountered in Hole U1438A (Unit I), and the two holes can be correlated on a bed-by-bed scale (Figure **F13**). A gap in recovery was identified in the transition between Cores 351-U1438A-2H and 3H using two key tie points (ash layers) found in each hole. The first correlated pair occurs in intervals 351-U1438B-2H-CC, 5–10 cm, and 351-U1438A-3H-1, 13–17 cm. The second is the ash bed found in intervals 351-U1438A-3H-1, 88–90 cm, and 351-U1438B-3H-1, 51–60 cm. These pairs indicate that there is material missing between Cores 351-U1438A-2H and 3H that was likely lost owing to a mechanical failure of the core liner.

Figure F12. Core and smear slide images for selected ash intervals, Hole U1438B. Top: left, thin light gray ash bed (19 cm) grades into shallower darker tuffaceous mud underlain by gray mud (8H-3A, 13–19 cm). Right, ash (14–15 cm) has blocky glass shards and pumice fragments. Note glass fragment size may have been artificially modified by grain crushing during smear slide production. Middle: left, dark ash lamina (8H-2A, 22–25 cm) at 24–25 cm; right shows green clinopyroxene and feldspar-bearing mafic to intermediate ash with both darker brown mafic vitric shards (center) and colorless glass. Bottom: left, light gray ash (14H-4A, 140–141 cm) shows right, large brown biotite crystals and colorless glass shards. All photomicrographs taken in plane polarized light (PPL).

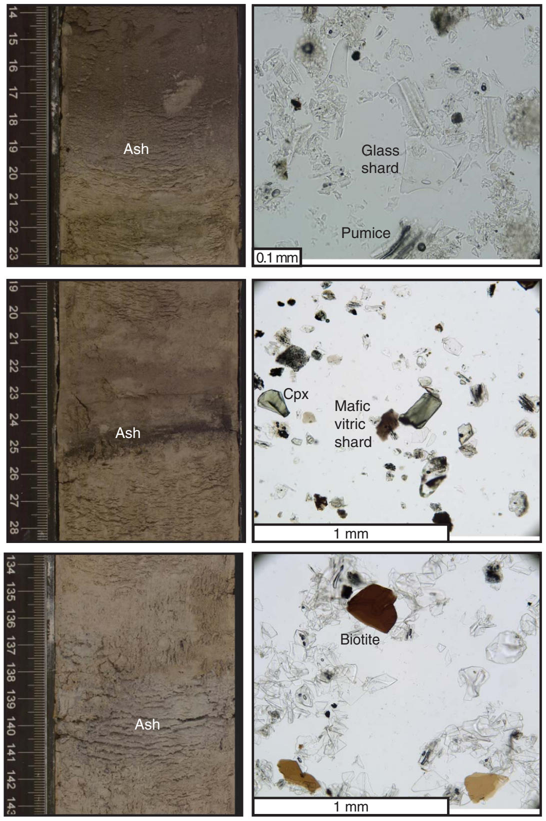

Unit II (Holes U1438B and U1438D)

Intervals: 351-U1438B-18H-1, 109 cm, to 30X-CC, 29 cm (bottom of Hole U1438B); 351-U1438D-2R-1, 0 cm (top of cored interval in Hole U1438D), to 12R-3, 75 cm
Thickness: 139.4 m (9.9 m offset in bedding between Holes U1438B and U1438D)
Depths: Hole U1438B = 160.3 mbsf; Hole U1438D = 309.6 mbsf
Age: Oligocene
Lithology: tuffaceous mudstone, siltstone, and fine sandstone

Unit I is underlain by Unit II, which was recovered in Holes U1438B and U1438D. Over the length of Core 351-U1438B-18H, there is a change over several meters from brown mud to lighter colored tuffaceous sediments. The upper contact of Unit II was chosen as the bottom of a mud layer in Section 351-U1438B-18H-1, 109 cm (Table **T2**). Deeper than this level, sediments become progressively more lithified, have coarser average grain sizes, and have higher carbonate contents and magnetic susceptibilities, defining Unit II (see **Physical properties and downhole measurements** and **Geochemistry**). Though complicated by poor recovery, the lower two-thirds of Unit II is also identified in Hole U1438D (see **Correlation between holes**, this section).

Figure F13. Correlation between the first three cores in Holes U1438A and U1438B created by visual inspection of core images. Selected ash-bearing and foraminifer/nannofossil intervals are correlated where determined to be similar in appearance, composition, and texture.

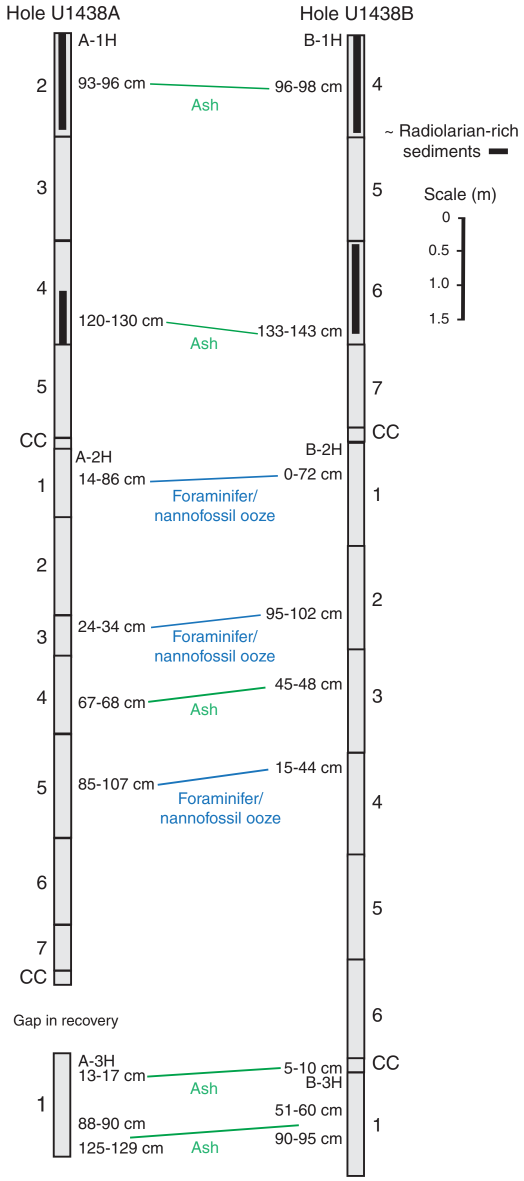

Description

Hole U1438B cores that comprise Unit II can be broadly described as intercalated <1 m intervals of medium to dark greenish gray tuffaceous mud/mudstone (5G 4/1, N5), silt/siltstone (N5, N4), and sand/sandstone (N3, N2) with intervening pale brown (5YR 5/2) ash/tuff layers (Figure **F14**). In Hole U1438D, these transition down to intercalated decimeter-scale intervals of medium to greenish gray, to dark greenish gray, to dark gray tuffaceous siltstone and mudstone (5GY 4/1, 5GY 6/1) and bluish gray tuffaceous mudstone (5B 5/1). Collectively, they are similar to the lithified sediments defined in Unit III but are less consolidated. Nannofossils are ubiquitous throughout the mud/mudstone, typically composing 10%–40% based on smear slide analysis. This increase correlates with a pronounced increase in measured carbonate content in Unit II: 5%–38% versus 0.4% in the overlying Unit I (see **Geochemistry**).

Figure F14. Bedding/lamination features in unconsolidated tuffaceous sediments from Unit II, Hole U1438B. Left: normally graded tuffaceous silt to sand layer at 4–10 cm marks the boundary between Units I and II. Right: two graded intervals comprise tuffaceous mud to fine sand.

Figure F15. Normally graded sandstone–mudstone bed with bioturbated top.

Tuffaceous mudstone, siltstone, and sandstone intervals form normally graded beds with sharp lower boundaries at the siltstone or sandstone base and bioturbated mudstone caps (Figures **F15**, **F16**). A typical sequence (bed) comprises sandstone overlying a sharp, often scoured contact with underlying mudstone normally graded uphole into laminated and then cross-laminated siltstone, locally deformed, and then mudstone with increasing bioturbation uphole.

Smear slides of the mud to fine sand components indicate they contain 25%–75% volcanic vitric and lithic grains in addition to minerals of volcanic origin such as plagioclase, pyroxene, amphibole, and opaque oxides. Both brown and colorless glass fragments are present. Nonvolcanogenic constituents are mainly clay derived in part from altered volcanic glass, as well as biogenic debris. Biogenic debris is mainly nannofossils with minor sponge spicules. Nannofossil-bearing, nannofossil-rich, and nannofossil mudstones, siltstones, and sandstones are found throughout Unit II.

In Unit II there are two intervals with abundant coarse sandstone at ~177 and 198–208 mbsf and two intervals dominated by mud at 162–168 and 223–227 mbsf. Prominent, relatively thick (0.7–1.6 m) dark gray sandstone layers are found in Sections 351-U1438B-21H-2 (176.4–178.1 mbsf), 25X-1 (200.0–200.7 mbsf), and 30X-6 (255.1–256.7 mbsf). Tuffaceous coarse sandstone with gravel and breccia-conglomerate are present in Hole U1438D only as heavily fractured intervals and within biscuits (core disturbances associated with drilling, e.g., Figure **F16**) and may have been lost during drilling, as suggested by the locally overall poor recovery. The coarse rocks are similar to those in several intervals in Unit II, Hole U1438B: polymictic matrix-supported dark gray (N3) sandstone to breccia-conglomerate, with clasts including pumice and a variety of volcanic rock fragments.

Ash/tuff layers occur throughout Unit II in Hole U1438B (Figure **F17**; Table **T4**). These are typically light brown in color and featureless with no bioturbation or lamination. Smear slide observations

Figure F16. Bedding/lamination features in tuffaceous siltstones, sandstones, and breccia-conglomerates from Unit II, Holes U1438B and U1438D. Top left: cross-laminated fine tuffaceous sandstone grades downward into coarse poorly consolidated tuffaceous sandstone (20–40 cm). Bottom left: soft-sediment deformation features in tuffaceous siltstone (88–99 cm). Right: tuffaceous coarse sandstone to breccia-conglomerate “biscuits” (0–22 cm) overlie bioturbated tuffaceous mudstone.

Figure F17. Two crystal-vitric tuff layers in Unit II, Hole U1438B.

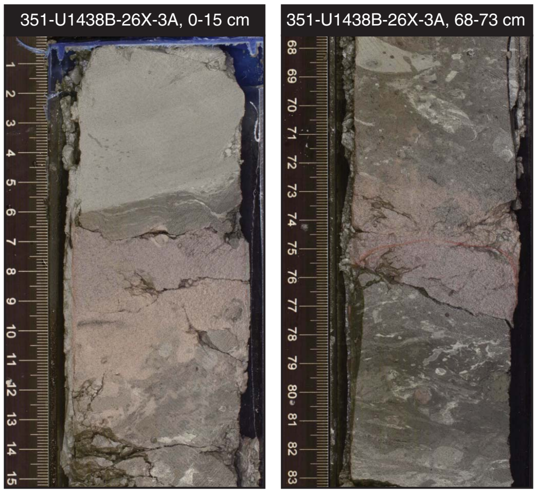

show them to contain colorless glass shards (up to 90%), volcanic lithic grains (up to 40%), and igneous mineral grains including feldspars, ferromagnesian silicates, and opaque minerals.

Identification of tuff beds (consolidated ash layers) in Unit II is complicated by the presence of the graded beds described above, which comprise sharp-based beds of tuffaceous siltstone grading upward into bioturbated mudstone, except locally where they have an interval of darker tuffaceous sandstone at the base. Some decimeter-thick tuffaceous siltstone beds (e.g., interval 351-U1438B-23X-1, 4–30 cm) are composed entirely of well-preserved vitric shards and feldspar, mirroring the mineralogy of tuff, with nannofossils. The contrast between volcanic tuff beds and tuffaceous deposits associated with these graded beds may be identified at the macroscopic scale by identifying the morphology of lower boundaries of individual sequences, as is illustrated by interval 351-U1438B-23X-4, 60–100 cm. Here, the white crystal vitric tuff, which grades from coarser grained crystal vitric tuff to finer grained vitric tuff, overlies a tuffaceous mudstone with a sharp contact at 99 cm, suggesting a volcanic air fall deposit. On the other hand, the upper part of Figure **F18** shows a dark-colored, crystal-rich (altered feldspar; hornblende), tuffaceous fine-grained sandstone, the base of which appears to be a scoured contact, suggesting erosional processes during deposition, more consistent with a higher energy gravity-flow deposit. Glass shards and minerals are fresh in both lithologic types, as shown in smear slides (Figure **F19**).

Tuff beds are rare in Unit II in Hole U1438D or perhaps only rarely identified owing to the intense drilling disturbance and poor recovery in the upper part of the hole. However, one specific reddish gray (5YR 5/2) ash layer is located within interval 351-U1438D-4R-1, 56–62 cm, and is described in detail below.

Correlation between holes

Holes U1438B and U1438D were cored 22.4 m from each other. Hole U1438B was cored from the surface to 257 mbsf, and Hole U1438D was cored from 219 to 897 mbsf. The 38 m of overlap between the two holes was complicated by initial relatively poor recovery in Hole U1438D and by the presence of dipping beds and faults in both holes at the level of the overlap (Figure **F19**). The overlap zones between the two holes were examined in detail, and a distinctive 1 m thick sequence of beds was identified in Cores 351-U1438B-27X and 351-U1438D-4R, consisting of a dark gray tuffaceous sandstone bed and a pale red ash layer intercalated with moderately bioturbated tuffaceous mudstone. This distinctive sequence of layers occurs in intervals 351-U1438B-27X-1, 57–74 cm (219.07–220.24 mbsf), and 351-U1438D-4R-1, 40–64 cm (229.90–230.14 mbsf) (Figure **F20**).

The dark gray (N2) laminated tuffaceous sandstone is 5 cm thick in Core 351-U1438B-27X and 4 cm thick in Core 351-U1438D-4R. The top contact with the tuffaceous mudstone shows a wavy boundary in both Cores 351-U1438B-27X and 351-U1438D-4R. The bottom contact with the tuffaceous mudstone is a sharp boundary in Core 351-U1438B-27X, whereas in Core 351-U1438D-4R, the bottom contact is lost by drilling disturbance. The tuffaceous sandstone is composed of fine to medium sand-sized vesiculated fresh pumice and contains opaque minerals, colorless glass shards, plagioclase, hornblende, clinopyroxene, magnetite, and minor sponge

Figure F18. Left: Fining-upward white tuff at 88–99 cm with a sharp bottom contact. Notice the strong bioturbation of the overlying tuffaceous mudstone and the scoured contact at the base of the darker tuffaceous sandstone. Top right: Vitric-rich (70% vitric glass) tuffaceous siltstone. Middle right: Upper finer grained vitric tuff seen in left image. Bottom right: White vitric tuff from left image shows coarse-grained vitric glass and crystals, feldspar (Feld), and hornblende (Hbld). All photomicrographs taken in PPL.

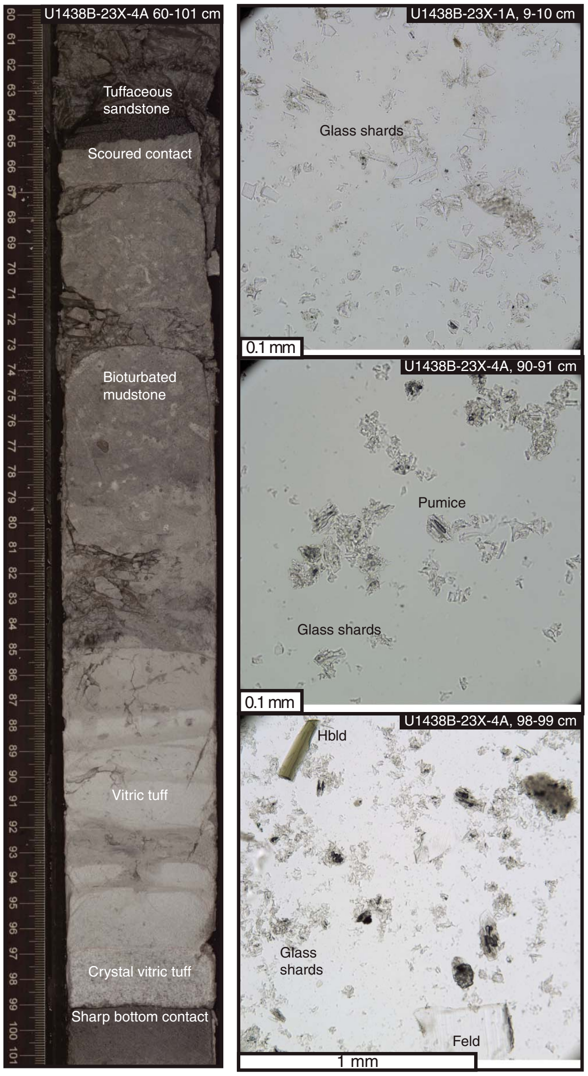

spicules, radiolarians, and nannofossils. The presence of biogenic grains mixed with fresh volcanogenic materials and sedimentary lamination indicate the tuffaceous sandstone is reworked ash.

The slightly bioturbated pale red (10R 6/2) ash marker horizon occurs between 6 and 12 cm deeper than the bottom of the dark gray tuffaceous sandstone in Cores 351-U1438B-27X and 351-U1438D-4R. Thickness of the layer is 5 and 7 cm in Cores 351-U1438B-27X and 351-U1438D-4R, respectively. The top contact with the tuffaceous mudstone shows an irregular shape because of bioturbation. The bottom contact with the tuffaceous mudstone is sharp. In Core 351-U1438D-4R, the pale red ash and lower tuffaceous mudstone are cut by a reverse fault dipping steeply relative to the orientation of the core. The ash consists of silt to medium sand-sized fresh, colorless glass shards and vesiculated pumice containing opaque minerals, plagioclase, clinopyroxene, hornblende, and magnetite.

Figure F19. Schematic column and structural features for the lower part of Hole U1438B (24X–30X) and upper part of Hole U1438D (2R–12R). Two arrows show the position of key beds (dark gray tuffaceous sandstone and pale red ash). Zones enclosed by blue lines indicate deformed or slightly deformed zones.

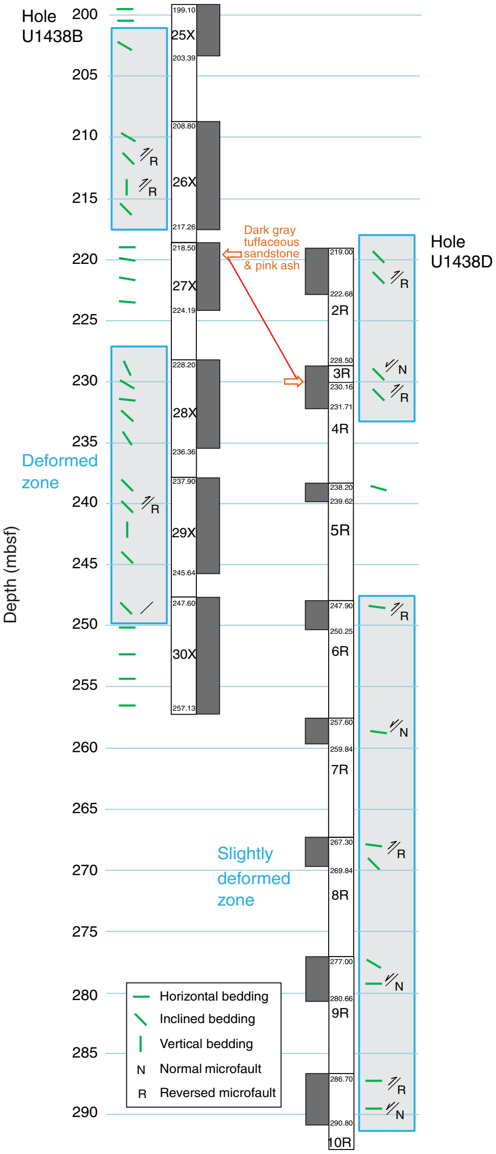

The 9.9 m difference between the depths of the marker horizon in the two cores is probably related to the structures that are present in the cores at the depths of the overlap. These consist of moderately dipping (40°–60°) faults that offset bedding (Figure **F21**). Most of the offsets show a reverse or thrust geometry with respect to the orientation of the fault plane. The zone of faulting and the steep dips of the beds occur in the same area, suggesting drag of bedding around a small reverse fault. Small 10 m offsets of major reflectors are present in the east–west seismic sections near the drill site (Figure **F22**).

Unit III (Holes U1438D and U1438E)

Intervals: 351-U1438D-12R-3, 75 cm, to 72R-CC, 35 cm (bottom of Hole U1438D); 351-U1438E-4R-1, 0 cm, to 55R-3, 5 cm

Figure F20. Key correlative marker beds in cores from Holes U1438B and U1438D, characterized by a pair of dark gray tuffaceous sandstone and pale red ash layers intercalated with moderately bioturbated tuffaceous mudstone.

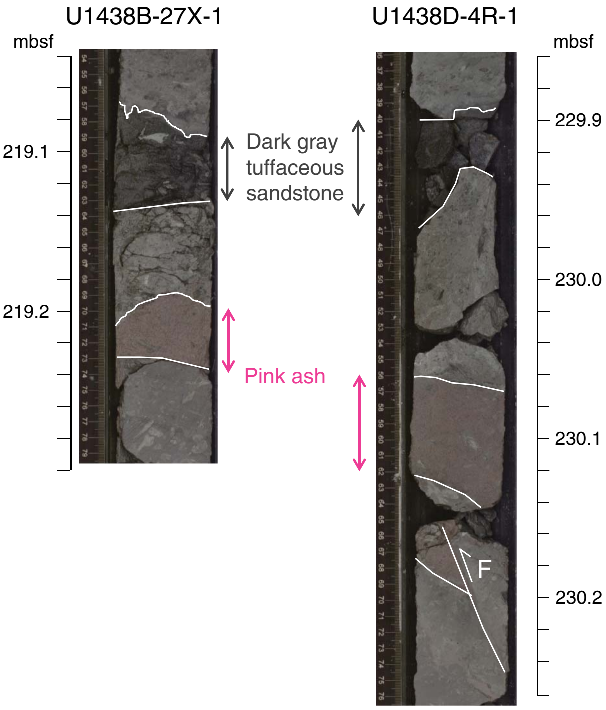

Thickness: 1046.38 m (5.4 m offset in bedding between Holes U1438D and U1438E)
Depths: Hole U1438D = 309.6–895.09 mbsf; Hole U1438E = 867.3–1361.35 mbsf
Age: Oligocene to Eocene
Lithology: tuffaceous sandstone, tuffaceous mudstone, tuffaceous breccia-conglomerate

Unit II is underlain by Unit III, which comprises the bulk of the stratigraphic interval recovered in Hole U1438D. The base of Unit II was chosen as the top of a prominent coarse sandstone interval in Section 351-U1438D-12R-3, 75 cm (Table T2). Deeper than this interval in Holes U1438D and U1438E, coarse-grained sedimentary rocks predominate in Unit III. When viewed as a whole, Unit III is characterized by repetitive conglomerate- and sandstone-dominated intervals with thinner intervening mudstone-dominated intervals lacking discrete conglomerate horizons. The base of Unit III is transitional into Unit IV, with progressively finer and thinner greenish sandstone to siltstone beds passing down into thicker intervals of reddish radiolarian-bearing mudstone in Core 351-U1438E-55R. The boundary between Units III and IV was chosen at the top of the first thick interval of red mudstone with radiolarians in Section 351-U1438E-55R-3, 5 cm.

Description

Tuffaceous mudstone is predominantly present between 500 and 590, 610 and 640, 660 and 730, and 860 and 870 mbsf in Hole U1438D and in Hole U1438E from 1225 mbsf to the base of Unit III. It is a minor component in the remaining intervals dominated by tuffaceous coarse sandstones and breccia-conglomerates, for example, between 890 and 910, 1085 and 1095, 1025 and 1035, and 1110 and 1155 mbsf in Hole U1438E. Tuffaceous mudstone can be either homogeneous or moderately to intensely bioturbated or show planar- to cross-laminated sedimentary structures where silt content is

Figure F21. Steeply inclined beds of tuffaceous mudstone with normal and reverse microfaults.

Figure F22. Southwest–northeast seismic section through the Site U1437 highlighting a putative fault showing offset of apparent bedding (from Japan National Oil Corporation, 1998).

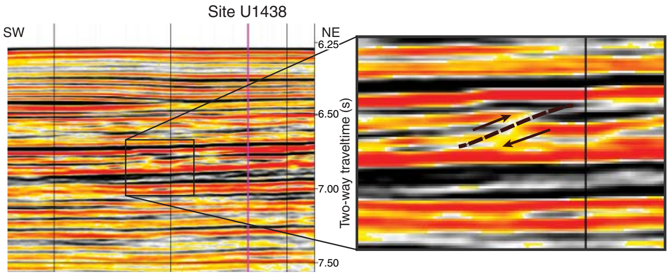

high. Mudstone colors range from gray (N5) and dark gray (5YR 4/1) to dark greenish gray (5G 4/1) and grayish red (10R 4/2) (Figure **F23**). Tuffaceous mudstone intervals are mainly 5–20 cm thick and are usually found as the upper part of an upward-fining sequence from tuffaceous fine sandstone or tuffaceous siltstone or as individual thin to medium beds with sharp and sometimes scoured basal contacts. Tuffaceous mudstones show a downhole change starting at Core 351-U1438D-43R toward slight to moderately bioturbated centimeter-thick mudstone beds alternating between very dark brown (10YR 2/2), dusky red (10R 3/4), and dark greenish gray (5G 4/1), with the occasional presence of alternating fine (<3 cm) beds of dark greenish gray fine sandstone.

Thin section examination shows that the mudstone is composed of clay-sized material, biogenic material, and mineral grains including plagioclase, pyroxene, and opaque oxides. In bioturbated areas, clay and opaque minerals are redistributed but the overall mineral content does not change. Smear slides reveal the presence of nannofossils, which decrease in abundance downhole.

In Unit III, tuffaceous siltstone layers are usually well sorted, but individual layers span the range in grain size from clay (fine) to sand (coarse) and overlie graded but poorly sorted tuffaceous sandstone and breccia-conglomerate. Compared with the coarser grained rock types, siltstone is more commonly laminated, frequently in sequences with planar-laminated, fine sandstone grading upward to siltstone, in turn grading upward into intervals with finely cross-laminated and ripple–cross laminated siltstone (Figure **F23**). Colors are typically medium to dark gray (N3 or N5), except in the interval marked by alternating dusky red (10R 3/4) and dark greenish gray (5G 4/1). Tuffaceous siltstone is particularly common from 985 to 1025 and 1245 to 1305 mbsf in Hole U1438E.

In thin section, tuffaceous siltstone consists of volcanic lithic fragments mixed with mineral grains, fresh and altered glass, and clay-sized material. Biogenic material is less abundant than in the tuffaceous mud and sandstone. Downhole, zeolite minerals replace or displace clay-sized and silt-sized mineral grains in the siltstone beds, in some cases forming abundant ~1 mm spheres (micronodules) of mixed zeolite and magnetite (Figure **F24**) or large (1 cm) pods of coarse zeolite aggregates. The alternating green and red mudstone and siltstone that are abundant from 600 to 875 mbsf consist of green clay, zeolites, and opaque oxides (Figure **F24**; see **Downhole changes in mineralogy (diagenesis and alteration)** for detailed analysis).

Tuffaceous sandstone is one of the main components of Unit III, as layers intercalated with tuffaceous breccia-conglomerate or alternating with tuffaceous mudstone. This sandstone may be in gradational contact with underlying conglomerate/breccia or show abrupt scoured to planar contact with underlying finer grained sedimentary rocks. Abundant normal grading is present in sandstone intervals throughout the unit. This grading may begin with breccia-conglomerate grading upward into sandstone or just a graded sandstone bed with no lower coarser interval, which, in turn, may grade upward into siltstone and mudstone. Planar lamination, cross-lamination, and inverse grading are also common. In thin section, tuffaceous sandstone samples are composed of approximately 10%–20% crystals and volcanic clasts regardless of their grain size or gravel content (Figure **F25**). Clasts are divided into three types: highly vesiculated vitric clasts (scoria), lithic clasts, and pumice. Pumice is the dominant clast type in tuffaceous sandstone, and the pumice content has an inverse correlation with crystal content. Based on percentage estimates, scoria is present with tuffaceous breccia conglomerate at 310–370 and 630–680 mbsf.

Figure F23. Features of Unit III tuffaceous mudstones and siltstones. Left: three sequences of planar laminated fine sandstone to siltstone, overlain by cross-laminated siltstone, overlain by bioturbated mudstone. Middle: thin laminated sandstone/siltstone layer, overlain by cross-laminated siltstone and bioturbated mudstone. Right: laminated fine sandstone and siltstone with dewatering structures.

Figure F24. Features in Unit IV siltstone and mudstones. Top: authigenic spheres composed of zeolites and magnetite in siltstone. Bottom: alternating red and dark green layers in siltstones and mudstones (PPL).

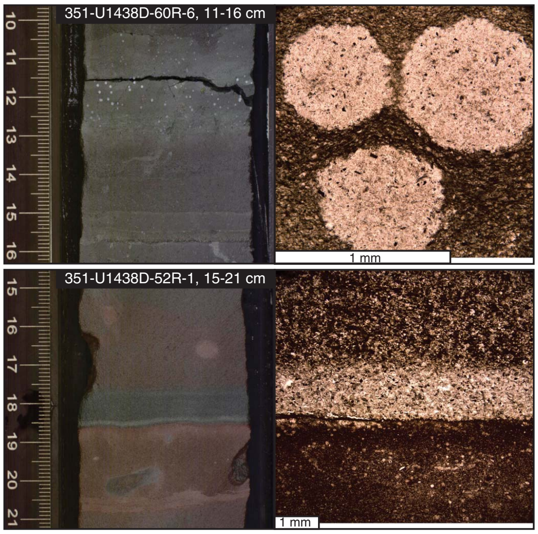

Abundant tuffaceous breccia-conglomerate beds and intervals are a defining characteristic of Unit III; these show increasing abundance in the interval 310–440 mbsf in Hole U1438D and occur locally between 520 and 800 mbsf in Hole U1438D; in Hole U1438E they are common from 1030 to 1060 and 1090 to 1180 mbsf, deeper than which gravel clasts are only found dispersed in Unit III sand-

Figure F25. Estimated volume of tuffaceous sandstone components in thin section. Left: total components in sandstone. Right: simplified volume estimation without grain size <silt, pores, and cement materials. Phenocrysts in volcanic clasts are counted as "clast." Fine, medium, and coarse sands are included, but gravel is excluded.

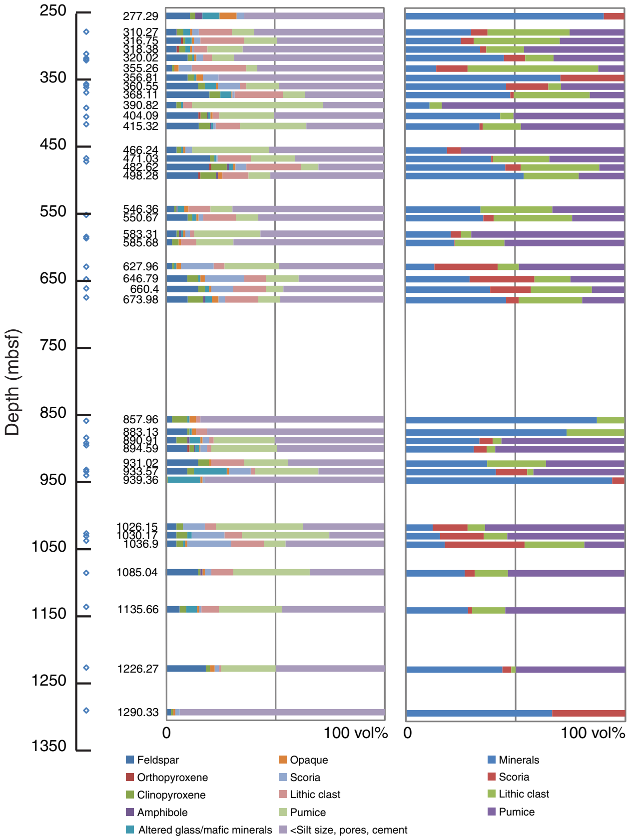

stone (Figure **F26**). Typically, the tuffaceous breccia-conglomerate beds form the base and/or midlayer of coarse volcaniclastic sequences with sharp lower boundaries (bedding planes) and range in color from grayish black to dark grayish green to grayish green (N3 to 5BG 5/2 to 5G 5/2), with a weak red (10R 4/2) variety at 899–900 mbsf in Hole U1438E. There is a continuum between two common types of tuffaceous breccia-conglomerate (Figure **F26**): (1) monomict or nearly monomict clast-supported pumice breccia-conglomerate, most abundant in the upper section (Cores 351-U1438D-13R through 27R); and (2) polymict clast-supported breccia-conglomerate with clasts of a variety of volcanic rocks, including pumice, scoria, and lava throughout Unit III. A third type may be represented by a layer of dark colored 3–4 mm lapilli (lapillistone) in Section 351-U1438D-40R-6 (Figure **F27**); these lapilli are also observed deeper in Unit III.

Pumice clasts range up to ~2 cm in size. In thin section, the groundmass is glassy or contains plagioclase microlites with isolated large (1 mm) plagioclase, pyroxene, opaque oxide phenocrysts, or glomerocrysts (clusters of phenocrysts) (Figure **F28**). The matrix for the breccia-conglomerate consists of clay- through sand-sized particles of pale- and dark-colored glass and volcanic minerals, including plagioclase, pyroxene, hornblende, opaque minerals, and biogenic material (foraminifers and radiolarians). Clasts are typically rounded and matrix grains angular.

The most common type of lava clast has plagioclase microlites and phenocrysts in a nearly opaque groundmass of glass and oxide minerals (Figure **F27**). These range in size from 2 cm to sand size and increase in abundance relative to other clast types downhole. Scoriaceous versions of this clast type are often red-colored from oxidation. Gray- and tan-colored holocrystalline clasts contain large (up to 2 mm) blocky plagioclase, clinopyroxene, and oxide pheno-

Figure F26. Top: monomict clast-supported tuffaceous breccia conglomerate with pumice clasts. Bottom: polymict clast-supported tuffaceous breccia conglomerate with clasts of holocrystalline volcanic rock, scoria, and pumice.

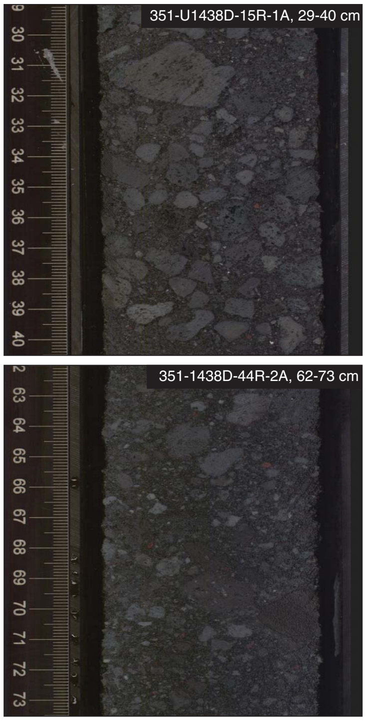

Figure F27. Top: A single 3 cm thick mafic lapillistone. Bottom left: lapillistone (PPL). Bottom right: same view as in bottom left but between crossed polars (XPL) which illustrates that lapilli are replaced by a brown clay mineral and zeolite (see **Veins and alteration**).

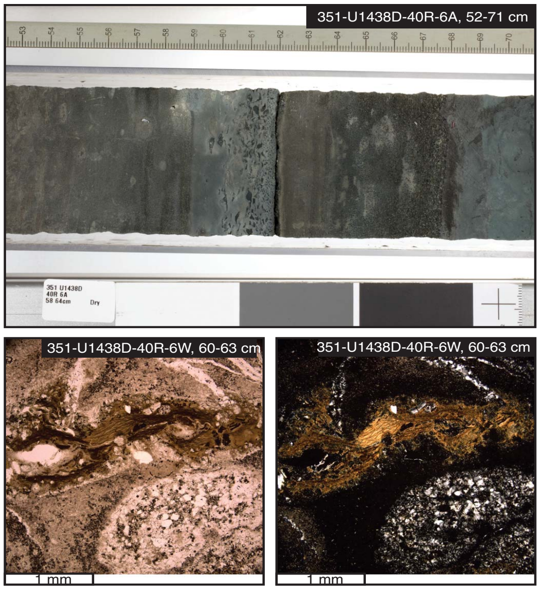

Figure F28. Common types of clasts in Unit III breccia-conglomerates (PPL, left), (XPL, right). Top: pumice clasts. Middle: black and gray volcanic rock clasts, with fresh plagioclase, pyroxene, and oxide (opaque) phenocrysts. Bottom: clast with euhedral inclusion-bearing hornblende phenocrysts, together with plagioclase.

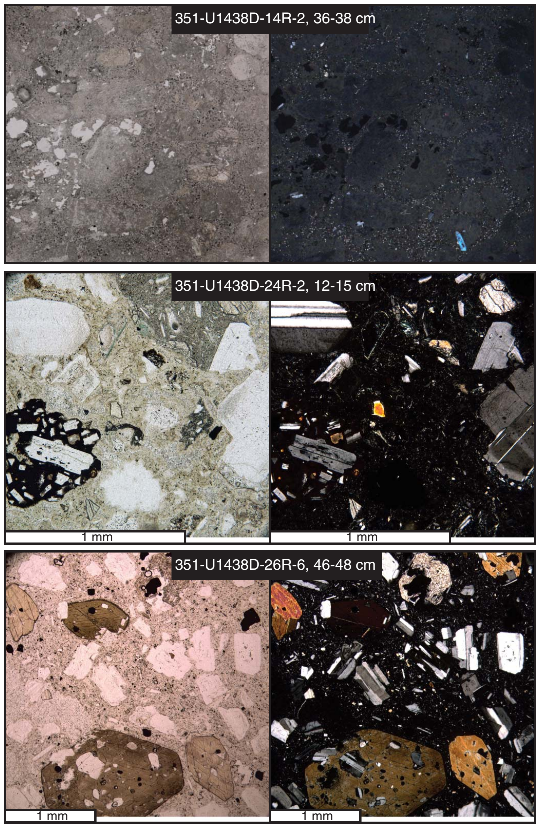

crysts. One clast with large hornblende phenocrysts was found in Core 351-U1438D-26R (Figure **F28**). Matrix for the polymict breccia/conglomerate intervals consists of progressively smaller lithic fragments and isolated angular mineral grains of volcanic origin, similar to the monomict pumice-rich breccia-conglomerate beds.

In the upper cores of Unit III shallower than approximately Core 351-U1438D-30R, a minority of pumice clasts and clear and brown glass fragments are fresh, but volcanic minerals are generally unaltered (Figure **F29**). Glass alters to light brown clay and then green clay with depth in the core. In Core 351-U1438D-53R and deeper, pumice clasts are replaced by anhydrite. Deeper than Core 351-U1438D-30R, plagioclase grains and matrix become more heavily altered and are replaced with green clay and zeolites. By Core 351-U1438D-46R, most feldspar is replaced by zeolites, whereas pyroxene grains are fresh (see **Downhole changes in mineralogy (diagenesis and alteration)** for detailed analysis).

Rare 1–9 cm thick tuff beds (Figures **F27**, **F30**) with sharp bottom contacts are present in Section 351-U1438D-40R-6 and are composed of a light olive-gray (5Y 6/1) clay containing pale green (5G 7/2) elongated, rounded, and/or angular shaped coarse ash and lapilli (pumice) clasts. Fresh glass shards, clinopyroxene, and feldspar crystals in the clay-sized fraction are rarely distinguishable, owing to pervasive zeolitization and chloritization (see **Downhole changes in mineralogy (diagenesis and alteration)**). The coarse

Figure F29. Alteration features in breccia-conglomerate clasts and matrix in the deeper cores of Unit III (PPL, left), (XPL, right). Top: green clay mineral cementation (note rims on grains) and replacement of some mineral grains with green clay. Middle: pumice clasts in a breccia-conglomerate completely replaced by anhydrite. Bottom: breccia-conglomerate matrix, clast groundmass, and a former ferromagnesian mineral, possibly olivine, are largely replaced by chlorite and zeolites, plagioclase is partially replaced by zeolites, and clinopyroxene is relatively unaltered.

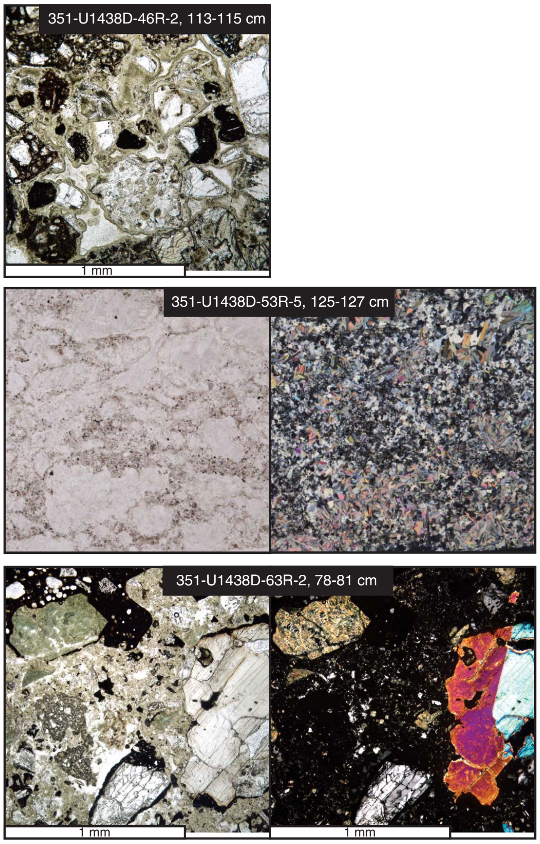

Figure F30. Left: 9 cm thick mafic tuffaceous sandstone or tuff bed with a sharp bottom contact and gradational upper contact into tuffaceous mud. Top right: aphyric and porphyritic coarse ash grains in zeolite-dominated matrix (PPL). Bottom right: aphyric coarse ash grain dominated by oriented euhedral feldspar microphenocrysts (PPL).

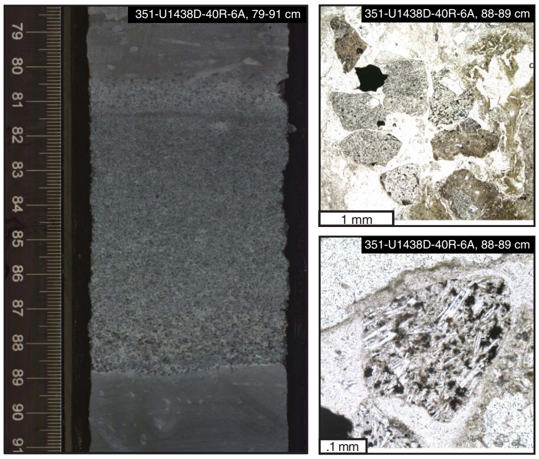

ash and lapilli clasts range from 0.5 to 5 mm in size and mostly preserve their original magmatic textures. These include vesiculated, aphyric, porphyritic, and/or pilotaxitic (dacitic) textures that are dominated by elongated euhedral to subhedral feldspar and clinopyroxene phenocrysts/laths, as well as microphenocrysts of the same minerals. Ash components <0.5 mm in size tend to be more spherical, whereas larger lapilli-size pumices tend to be elongated, oriented parallel to the bedding, and altered to chlorite and clay minerals.

Other possible 1–3 cm thick tuff beds are found in Cores 351-U1438D-65R, 67R, and 68R (Table **T4**). These have been interpreted as tuff on the basis of sharp contacts with the surrounding tuffaceous mudstones and gray colors contrasting with the green mudstones. In thin section, we also recognize higher concentrations of opaque minerals, colorless glass shards (now mostly altered to zeolites), and poorly preserved pumice fragments. Large plagioclase and subhedral clinopyroxene crystals appear to be well preserved within these tuffs. Mafic lithic fragments with dark brown (in plane polarized light) groundmass and phenocrysts of feldspar and clinopyroxene are also present.

Correlation between holes

Holes U1438D and U1438E are located 30 m from each other, with Hole U1438D cored from 219 to 895 mbsf and Hole U1438E cored from 867 to 1361 mbsf. Cores spanning the 28 m of overlap between the two holes were examined in detail, and there is a good overlap sequence of rocks that occur in Sections 351-U1438D-72R-3 and 351-U1438E-7R-1 based on the patterns in magnetic susceptibility and gamma ray intensity and on visual inspection of grain size, rock type, and the presence of key beds. The key marker beds are characterized by decimeter-scale beds of dusky red (10R 3/4) tuffaceous siltstone within a larger domain of greenish black (5G 2/1) tuffaceous medium to coarse sandstone. These layers occur in intervals 351-U1438D-72R-3, 127–142 cm (891.93–892.08 mbsf), and 351-U1438E-7R-1, 110–128 cm (897.30–897.48 mbsf) (Figure **F31**). The apparent 5.4 m difference between the depths of the marker horizon in the two cores is probably related to poor core recovery across this interval.

Unit IV (Hole U1438E)

Interval: 351-U1438E-55R-3, 5 cm, to 351-U1438E-69R-1, 18 cm
Thickness: 99.72 m
Depth: 1361.35–1461.08 mbsf
Age: Eocene
Lithology: mudstone with radiolarians, tuffaceous siltstone and siltstone, tuffaceous sandstone and sandstone, breccia-conglomerate

Unit IV is the most lithologically diverse suite of rocks encountered at Site U1438. Although it contains several thin siltstone/sandstone beds and laminae similar to those in the lower part of Unit III, Unit IV is distinct in that it comprises significant intervals of mudstone with radiolarians, with the top of Unit IV chosen at the first occurrence of a thick mudstone interval in Section 351-U1438E-55R-3. Deeper than this, radiolarian-bearing mudstone dominates the recovery for 50 m (~1352–1405 mbsf). The bottom half of the unit is characterized by an interval of medium to coarse sandstone and breccia-conglomerate passing downcore into an assemblage of fine to coarse tuffaceous rocks. The lower contact with igneous rocks of Unit 1 is overlain by a 4 m section of dark reddish mudstone and sandstone (see further description of contact in **Unit 1 (Hole U1438E)**). Drilling deformation and poor recovery in some intervals make lithologic relationships hard to decipher.

Description

Mudstone dominates both the upper and the lower part of Unit IV and is interbedded with the coarser grained rocks in the middle part. Radiolarians are a prominent part of the mudstone in the upper part of the unit, forming up to 20% of the rocks. The upper part is mainly reddish in color, and some of the lighter colored intervals also contain zeolite concretions (up to 5 mm in diameter) that give the mudstone an uneven texture. Deeper in the hole toward the contact with the basement, the mudstone is darker and more brown in color. Unlike the mudstone intervals in the younger lithostratigraphic units, bioturbation in Unit IV is either slight or absent (Figure **F6**). In thin section, the mudstone consists of variously recrystallized radiolarians and rare plagioclase, clinopyroxene, and opaque crystals in a fine-grained, dark, clay-size matrix. Some mudstone (e.g., in Core 351-U1438E-58R) contains large (up to 10 mm) altered (chloritized) and deformed (flattened) pumice with plagioclase phenocrysts. Fish teeth and bone fragments were noted toward the top of the unit (e.g., in Core 351-U1438E-55R).

Thin siltstone laminae within the radiolarian-bearing mudstone in the upper part of Unit IV range from black (N2.5) to dusky blue green (5BG 3/2) in color and are locally mottled with reddish hues, often because of bioturbation and/or alteration. Lower in the unit, starting in Core 351-U1438E-61R, tuffaceous siltstone is present as part of graded sandy intervals that become thicker in Core 351-U1438E-64R and grade vertically down into sandstone. In contrast to the siltstone in the upper part of the unit, smear slide and thin section observations indicate the siltstone in the lower part ranges from crystal rich to tuffaceous and is very dark gray (N3) to grayish black (N2) to weak red (9R 4/2) in color. Throughout the unit, siltstone intervals locally exhibit parallel and cross laminae. The siltstone intervals are in some cases only a few centimeters thick and too thin to be indicated on the VCDs.

A few laminae of greenish gray (5G 6/1) tuffaceous fine sandstone with pebbles and dispersed sand grains occur within the mudstone in the upper half of the unit. In the lower half of the unit, starting in Core 351-U1438E-61R, centimeter- to decimeter-scale layers of fine to medium to coarse sandstone beds range in color from dark gray (5YR 4/1) and dark greenish gray (5G 4/1) to very dark gray (N3) (Figure **F32A**). These layers exhibit normal grading, lamination, cross lamination, and in one instance, high-angle cross-bedding, in some cases starting at a scoured base. They locally contain irregularly shaped lithic fragments of porphyritic basalt. As with the associated siltstone beds, these are thickest in Core 351-U1438E-64R. Thin sections from Cores 351-U1438E-61R through 66R show that the sandstone intervals consist of common to abundant volcanic rock fragments exhibiting microlitic to vesicular to pumiceous textures, in addition to rounded to subangular grains of plagioclase, pyroxene, amphibole, and opaque minerals (Figure **F32**). Sedimentary (siltstone/mudstone) rock fragments are rare in these cores, which also contain some black tachylitic glass fragments with plagioclase microlites. The feldspar, ferromagnesian minerals, and volcanic grains are variably altered to zeolites and clay minerals, which also occur as cementing phases, although clinopyroxene grains are unaltered. In Core 351-U1438E-68R, sandstone laminae are unusual in that they are crystal rich and dominantly plagioclase and green amphibole. These also contain some red amphibole and amphibole-bearing volcanic fragments with felsic groundmass.

Figure F31. Key marker beds associated with the correlation between the bottom of Hole U1438D and the top of Hole U1438E. Correlations are based on patterns in MS, NGR intensity, and visual inspection of key beds.

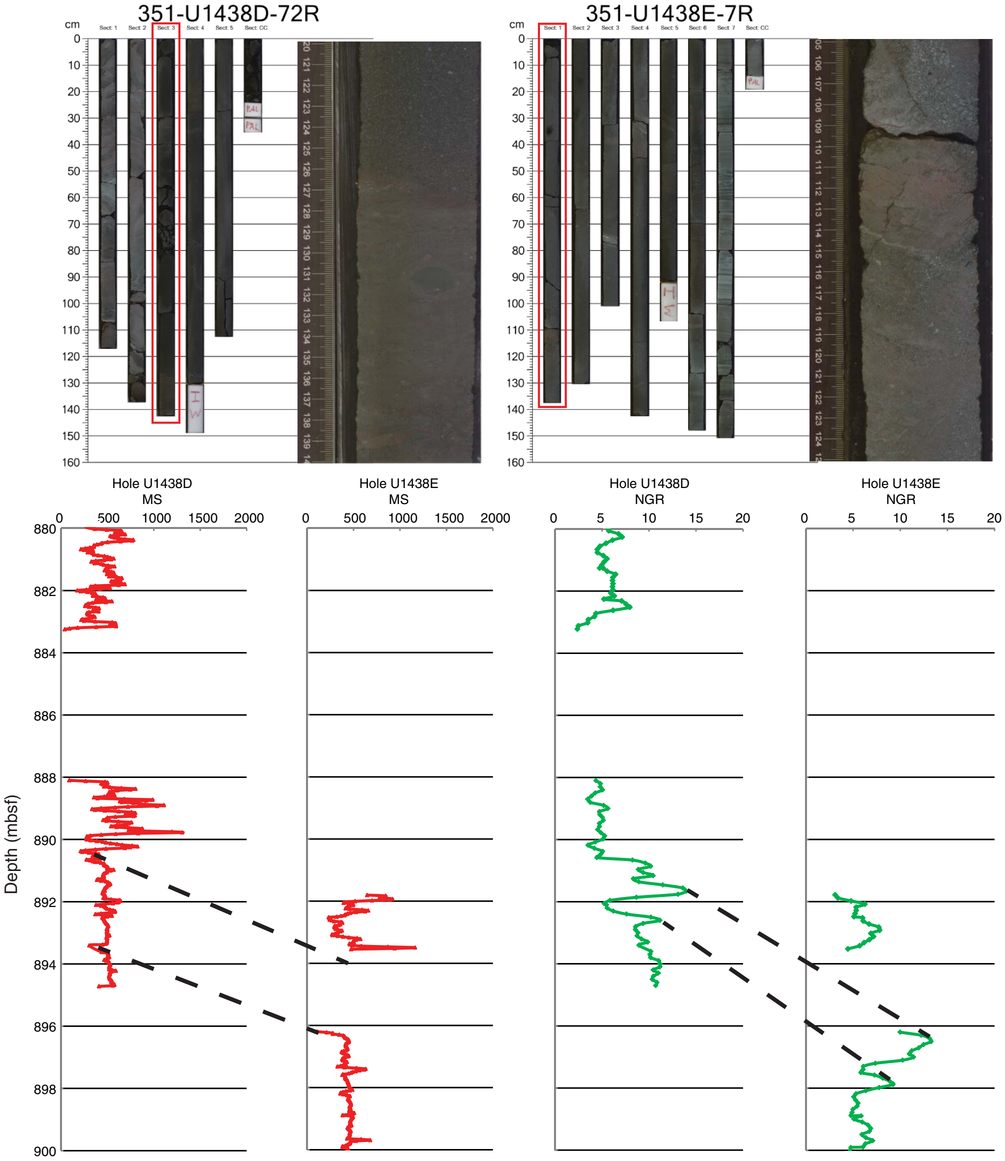

Tuffaceous breccia-conglomerate occurs at three stratigraphic levels in Unit IV, all beneath the igneous rocks (Sections 351-U1438E-62R-2 and 63R-2). These coarse-grained beds typically overlie mudstones along sharp bedding planes (Figure **F32C, F32E**). Unlike the sandstones, breccia-conglomerates are poorly sorted, and clasts include igneous and sedimentary rocks in subequal amounts, as well as abundant biogenic sediment. Clasts range up to 1 cm in reddish brown and pale green colors. Microscopically, igneous clasts include mafic lithic fragments with plagioclase microlites and pumice and are severely altered, with feldspar and groundmass replaced by zeolite, hematite, and clay minerals (Figure **F32D, F32F**). Plagioclase and clinopyroxene grains (up to 1 mm) also occur loose in the matrix; plagioclase is heavily replaced by zeolites and pyroxene appears unaltered. Sedimentary clasts are mostly mudstone, frequently with radiolarians. Thus, although radiolarian-rich mudstones were not sampled in situ in the lower part of Unit IV, they were available to form clasts in the breccia-conglomerates. The matrix for the breccia-conglomerates consists mainly of clay, hematite, and zeolites. Radiolarians are also abundant in the matrix (Figure **F32D, F32F**).

Igneous rocks in Hole U1438E Unit IV are present in three locations that lie 49–55 m above the top of the basement at 1461 mbsf. The first (youngest) occurrence is at 1406.33 mbsf, where igneous rock is present at the bottom of Section 351-U1438E-61R-1 and the top of Section 61R-2. The second occurrence is in the bottom of Section 61R-2 at 1407.24 mbsf. The third (oldest) occurrence is at 1411.64 mbsf, at the bottom of Section 62R-1 and the top of Section 62R-2 (Figure **F5**).

In all three locations, Unit IV igneous rock intervals are sparsely phyric, with 3%–5% phenocrysts and microphenocrysts of clinopyroxene (0.2–1.0 mm) set in a groundmass of devitrified glass with microlites of plagioclase and pyroxene (Figure **F33**). Alteration minerals including chlorite-clay, zeolite, hematite, and titanite are also present. The presence of solely clinopyroxene phenocrysts, the fine

Figure F32. Hole U1438E, Unit IV. A, B. Tuffaceous sandstone (64R-4; B: PPL) shows mafic and pumiceous lithic sand grains and volcanic mineral grains (arrow). C, D. Tuffaceous breccia-conglomerate (62R-2; D: XPL) shows abundant radiolarians in a mudstone clast. E, F. Tuffaceous breccia-conglomerate (351-U1438E-63R-2; F: PPL) shows a mudstone clast (left) in contact with sand-sized lithic fragments, mineral grains, and radiolarians (arrow). Scale bars = 1 mm.

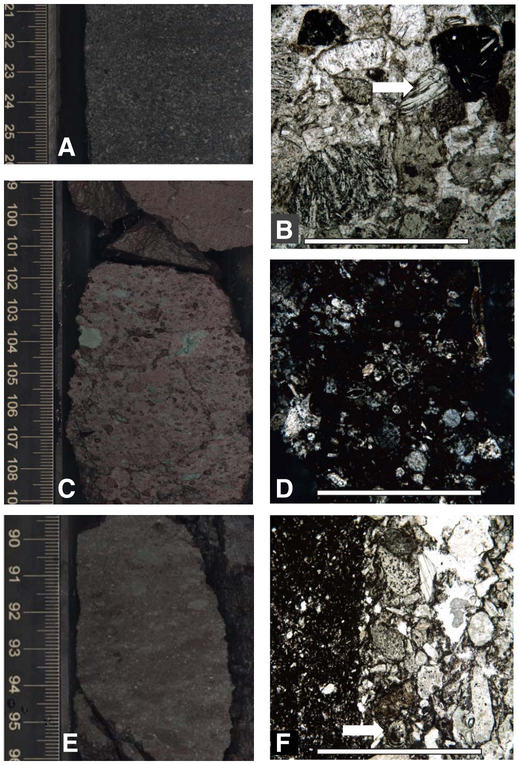

Figure F33. Hole U1438E, Unit IV, igneous rock (top; 61R-2, TS-93; XPL) compared to basement basalt (bottom; 75R-1, TS-111; XPL) at the same scale. Phenocrysts in the Unit IV igneous rocks are pyroxene only. Note also the fine groundmass and absence of plagioclase. All Unit IV igneous rocks share these petrographic characteristics.

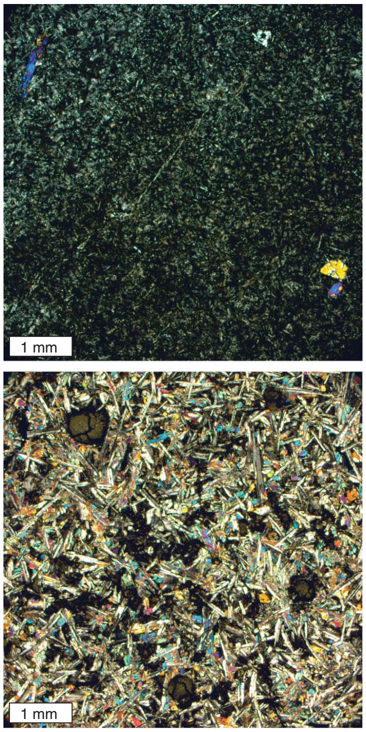

groundmass, and the absence of plagioclase readily distinguish the Unit IV igneous rocks from basalts of the underlying basement. Geochemical analysis (see **Geochemistry**) shows these igneous rocks are high-Na basaltic andesite.

All of the Unit IV basaltic andesites have quench features (e.g., Figure **F33**), and contacts with the overlying and underlying sedimentary rocks are horizontal to subhorizontal. These features suggest the basaltic andesites are shallow intrusive rocks, probably sills, and not volcanic blocks or sedimentary cobbles deposited on the sediment surface. This interpretation is underscored by the occurrence at the bottom of Section 351-U1438E-61R-1 of basaltic andesite entirely enclosed within a sandy interval that was likely deposited rapidly and in a single event. Under these circumstances, the co-occurrence of a >12 cm volcanic block or sedimentary cobble is unlikely. Petrographic observations also provide evidence for mingling of mud/mudstone and magma, as would be expected in an intrusive contact. These relationships may be seen in Sample 351-U1438E-62R-1, TS 95 (1411.61 mbsf), where coarsely zeolitized rock near the center of the section encloses both phenocrysts of clinopyroxene from the basaltic andesite and opaque clots of mudstone. These relationships would be expected if formation of zeolite minerals was concentrated in glassy and fragmented material formed by mingling of magma and mud/mudstone in the contact area between the two lithologies. Based on this reasoning, it appears likely the Unit IV basaltic andesites were emplaced from a local intrusion (dike/sill). The petrographic similarity of the basaltic andesites and their clustering within <6 m of core suggest that all three of the occurrences may have been emplaced in a single event. It is not clear whether the basaltic andesites were intruded into solidified sedimentary rock or unconsolidated sediment, but the location of the sills, 50 m above the basement surface and in mostly fine-grained sedimentary rock, suggests the Unit IV basaltic andesites are significantly younger than the basement basalts.

Unit 1 (Hole U1438E)

Interval: 351-U1438E-69R-1, 18 cm, to 88R-1, 150 cm
Thickness: 149.9 m
Depth: 1461.08–1611.0 mbsf
Age: Eocene(?)
Lithology: basalt

At 1461.08 mbsf, along a rubbly contact, brown laminated mudstone of Unit IV is underlain by oxidized basalt rocks of Unit 1 which extend to the bottom of the hole at 1611 mbsf. Note that unit numbers follow IODP convention where the sedimentary units are characterized by Roman numerals and igneous units with Arabic numbers. In the ~150 m cored interval of Unit 1, only 44 m (29%) of core was recovered. Although probable contacts were recognized between adjacent individual core pieces based on grain size variations and chilled margins, substantial drilling disturbance made consistent recognition of individual unit boundaries and estimation of thicknesses impractical, so all igneous basement rocks are grouped together in a single unit. Unit 1 is primarily composed of sparsely vesicular to nonvesicular, microcrystalline to fine-grained, aphyric to sparsely porphyritic basalts (Figure **F34**). Rare pheno-

Figure F34. Igneous textures in Unit 1 basaltic rocks (XPL, left). (PPL, right).

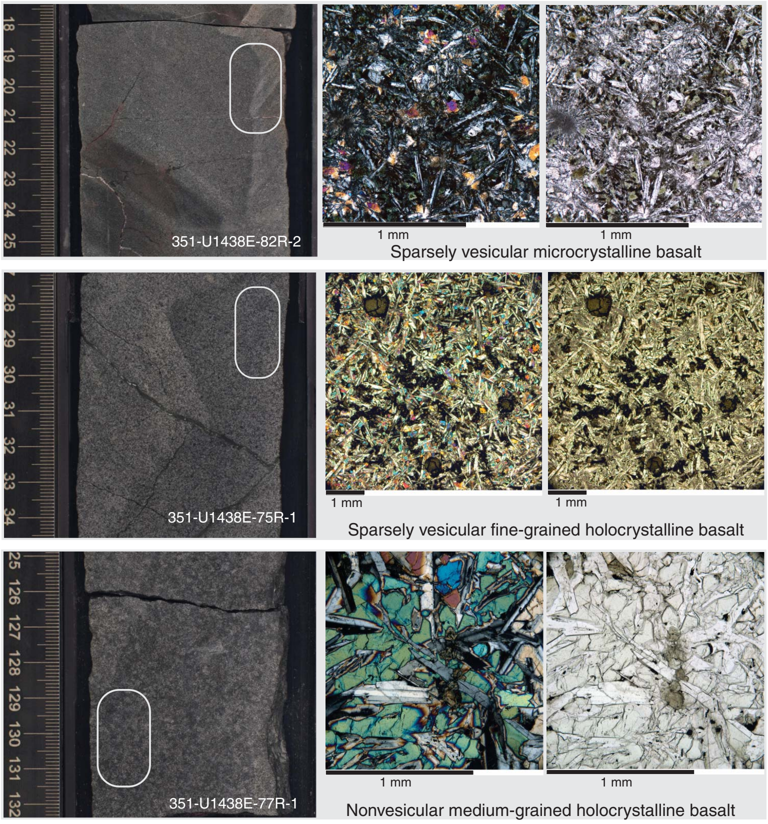

crysts of olivine, pyroxene, and/or plagioclase up to 3 mm in maximum dimension are set in holocrystalline groundmass characterized by abundant feathery plagioclase. Macroscopic alteration is predominantly patchy chlorite and oxides replacing phenocrysts and groundmass, chlorite and carbonate filling sparse vesicles, and veins filled with chlorite + carbonate ± sulfides and/or oxides. Alteration in the basalts is strong in Cores 351-U1438E-69R through 73R and decreases to moderate intensity from Core 74R to the bottom of the hole.

Description

In thin section, the microcrystalline to medium-grained basalts have diverse textures that include (sub)ophitic, spherulitic, intersertal, dendritic, variolitic, (glomero)porphyritic, vitrophyric, aphyric, amygdaloidal, and glassy varieties. Vesicles are present in approximately one-third of the rocks but are usually sparsely distributed within each rock. However, one sample is moderately vesiculated (30%) with irregular vesicle shapes (Sample 351-U1438E-81R-1, 98–102 cm; TS 127).

Phenocrysts are present in approximately half of the basalts and consist of plagioclase, clinopyroxene, titanomagnetite, and olivine in order of decreasing abundance. The majority of phenocrysts range in size from 0.2 to 4 mm. Plagioclase phenocryst abundances range from 0% to 30%, although observations made of thin sections show 0%–5% is most common. These plagioclase phenocrysts tend to be blocky and sometimes zoned. Clinopyroxene phenocrysts occur more rarely and tend to be smaller (0.2 mm) than plagioclase. The occurrence of olivine either as a phenocryst or in the groundmass is difficult to estimate due to the strong alteration. In four cores however, olivine that is pseudomorphed by chlorite is recognizable by shape and the presence of small, partially translucent reddish chrome spinel inclusions (Cores 351-U1438E-71R, 75R, 80R, and 84R) (Figure F35). It is possible that olivine occurs more widely but is now difficult to recognize due to the alteration.

Figure F35. Unit 1 basalts, Hole U1438E. Top left: chrome spinel (80R-1W; 1534.53 mbsf; PPL). Top right: olivine replaced by calcite (84R-1W; 1571.94 mbsf; PPL). Bottom left: quench textures in basalt (75R-1; 1504.33 mbsf; XPL). Bottom right: alteration of basalts (83R-2W; 1563.97 mbsf; XPL).

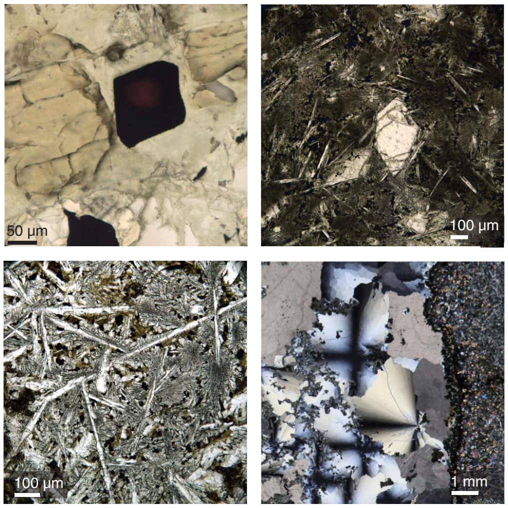

The groundmass of the basalts is mostly holocrystalline and is composed primarily of plagioclase, clinopyroxene, and titanomagnetite. Glass can be significant in the groundmass (up to 85%; average = 25%), but it is entirely altered mostly to chlorite. Plagioclase mostly occurs as narrow, elongated crystals in subophitic relationships with clinopyroxene. Plagioclase is the most common crystalline phase, comprising between 10% and 45% of the groundmass, whereas clinopyroxene comprises 11% and 40% of the groundmass (Figure **F35**).

Numerous flow contacts were identified in Unit 1, but their interpretation in terms of volcanic stratigraphy is hindered by the overall low recovery in basement rocks (29%). The majority of magmatic contacts are gradational in the core, showing a diffuse change in grain size to micro- or even cryptocrystalline (Figure **F36**). Moreover, several chilled margins could be identified, but only very few of those preserved a glassy margin (altered) (Figure **F37**). A full list of possible flow contacts can be found in Table **T5**. The average flow thickness calculated from the thickness of the intervals between each boundary (or their mean when only a long gradational interval could be identified) is about 3.1 m, but this value is highly biased by the low recovery. Paleomagnetic measurements provide constraints on the lava flow type, and consistent shallow plunges of maximum anisotropy axes indicate a dominant flow direction. Thus, lava emplacement by lava flows (e.g., sheet flows) are more likely than pillow lavas (see **Paleomagnetism**).

Veins and alteration

Veins are much more common in the basaltic lavas than in the overlying sedimentary rock sequence. Although these veins vary widely in orientation, slightly more horizontal or shallow-dipping veins were recorded than vertical or steep veins. Most of the veins are small (average = 3 mm wide) and filled with calcite, chlorite, and clay minerals, and they tend to form branched networks. There are small differences in the mineralogy of the veins downhole, particularly in the oxidation state of the iron minerals that accompany the ubiquitous carbonate and chlorite + clay. Logging shows broad 20–40 m zones dominated by veins containing hematite, calcite, and chlorite with red halos alternating with zones that contain veins containing pyrite, chlorite + clay, and calcite ± magnetite without halos.

Two zones contain veins or alteration patches with crystalline and microcrystalline silica:

1. Large (2–4 cm) alteration patches in Section 351-U1438E-83R-2 have spectacular large (4 mm diameter) radiating rosettes of quartz intergrown with large subhedral calcite, small zeolite minerals, and small anhedral clay and chlorite crystals (Figure **F35**).
2. Small veins (2 mm) in Section 351-U1438E-87R-3 contain hematite, calcite, microcrystalline silica, and chalcopyrite.

Downhole changes in mineralogy (diagenesis and alteration)

Downhole changes in mineralogy at Site U1438 are documented from smear slide, XRD, and thin section observations and show that dominantly fresh volcanogenic minerals and glass within Unit II (depths <300 mbsf) are transformed into mixtures of dominantly clay and zeolite minerals (Unit III at depths >500 mbsf). We refer to these mineralogical changes as diagenetic given the thermal gradient and bottom-hole temperature estimates for Site U1438 (see **Physical properties and downhole measurements**), but they could be equally well described as effects of alteration or secondary mineral formation.

Plagioclase, pyroxene, and calcite are the dominant minerals in Unit II cores deeper than the downhole transition from Unit I to Unit II. Plagioclase compositions appear to be calcic, and pyroxenes include both monoclinic (clinopyroxene) and orthorhombic (orthopyroxene) varieties. Peaks in many Unit II sample X-ray diffractograms at 10°–11°2θ indicate the presence of amphibole(s), and their presence is confirmed by smear slide observations. Database searches on XRD patterns most commonly identify these as calcic amphiboles (e.g., pargasite, magnesiohornblende, or edenite), but other more sodic or magnesian varieties (e.g., crossite, riebeckite, or

Figure F36. Sheet flow base contact in Unit 1 (351-U1438E-83R-1A, 14–40 cm). Grain size changes gradationally from flow interior (microcrystalline) to flow base (cryptocrystalline). Cooling joints also developed at flow base and show oxidized halos by secondary alteration.

Figure F37. Chilled margins in Unit 1 (oceanic igneous basement), Hole U1438E. Left: chilled margin with decrease in grain size toward the flow contact. Right: flow contact with altered glassy matrix and spherulitic microphenocrysts.

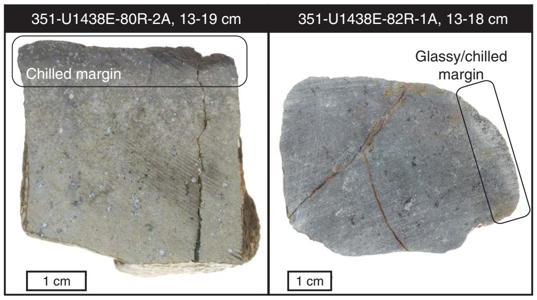

Table T5. Chilled margin summary. **Download table in .csv format.**

gedrite) might also be present. Identification of foraminifers and nannofossils in many smear slides from Unit II indicates that calcite occurs primarily as a sedimentary/biogenic component. Smear slide observations indicate the silicate minerals and associated volcanic glass in Unit II are largely free of hydrous alteration effects. Significant quantities of diagenetic minerals were observed only in XRD data for bioturbated mudstone Sample 351-U1438D-11R-2, 49–50 cm. Database searches for this XRD pattern return the zeolite mineral clinoptilolite.

In the upper part of Unit III, at about 300–500 mbsf, zeolite minerals observed in trace quantities in Unit II become common and their abundance relative to fresh, volcanogenic components increases. This downhole change, which increases progressively to the bottom of Hole U1438D, is illustrated in Figure **F38**, where summed peak counts for selected zeolite group and related minerals are plotted against depth for all XRD scans from Units II and III. At 300–500 mbsf, Unit III XRD data show that calcic plagioclase and pyroxene are still abundant minerals, as they were in Unit II. Calcite is also commonly present, as in Unit II, but in contrast, thin sections confirm its presence as minor authigenic cement. Most Unit III samples at 300–500 mbsf also contain one or more zeolite group minerals in combination with sheet silicate and other minerals that appear to be diagenetic. Database searches indicate that clinoptilolite is the most common zeolite present in these samples, but thompsonite, phillipsite, and mordenite were also identified. The XRD data confirm the presence of chlorite (clinochlore) in Unit III from 300 to 500 mbsf. Database searches also return celadonite, vermiculite, and smectite group clays, such as saponite and sauconite. The smectite minerals do not appear to be abundant in Unit II mudstones, so their presence in many Unit III samples (along with zeolites) indicates they are not detrital but instead have formed by diagenetic processes. Brown and yellowish brown material in the groundmass of tuffaceous sandstones (e.g., Figure **F27**) shows second-order birefringence, and in combination with XRD patterns, this material is interpreted to be mixtures of chlorite, smectite group clays, celadonite, and vermiculite. The texture of this mixture, where it commonly forms grain coatings and with radiating fibers (pore fills), also indicates a diagenetic origin. The XRD data indicate that zeolite minerals are present in most samples in the 300–500 mbsf interval, but these minerals are not easily identified in thin section. Where observed, they form irregular masses of weakly birefringent, low-relief minerals in the groundmass, sometimes in fibrous and radiating forms.

Deeper than 500 mbsf in Unit III and to the bottom of Hole U1438D, XRD data indicate that many samples are dominated by zeolite and related framework and sheet silicate minerals that are formed by diagenetic processes. In turn, the volcanogenic components that dominate Unit II diminish in importance in Unit III. The main diagenetic phases deeper than 500 mbsf are clinoptilolite, laumontite, and analcite. Mixtures of clay minerals produce broad peaks below 8°2θ in many samples, as in shallower parts of the core, but in several samples the appearance of sharp and intense peaks at 6.1°2θ indicate the presence of a new and well-crystallized mineral. Database searches indicate that this may be the zeolite mineral faujasite mixed with vermiculite and saponite or other smectite group minerals. Chabazite, wairakite, and stellerite (all zeolite minerals) are also identified in some samples. Thin section (Figure **F29**) and XRD data show that anhydrite is present locally, where it appears together with zeolite minerals in replacement of pumice lapilli and in millimeter-scale veins. The most thorough recrystallization and formation of diagenetic minerals has taken place in the finer grained mud- and clay-rich rocks. In some cases, these have been reduced to simple monomineralic and bimineralic zeolite (e.g., Figure **F24**). Based on evaluation of XRD scans, calcic plagioclase and pyroxene appear to be absent from many fine-grained samples, but thin sections show these minerals persist in diagenetically altered tuffaceous sandstones even at the bottom of Hole U1438D. Plagioclase crystals are often corroded and partially or wholly replaced by zeolites, but most pyroxene appears to have been little affected by diagenesis (e.g., Figure **F29**). Well-preserved volcanic glass is rare in Unit III but has been observed in thin section to the bottom of Hole U1438D. The general style of diagenetic alteration of volcaniclastic rocks at Site U1438 was also documented in nearly time-equivalent and lithologically similar IBM fore-arc cores recovered during Ocean Drilling Program (ODP) Leg 126 (Marsaglia and Tazaki, 1992).

Figure F38. Summed peak counts, Holes U1438B and U1438D. Maximum counts for peaks between 9° and 18°2θ identified by the Bruker Diffraction Evaluation software were summed for seven common zeolite groups and related minerals identified in X-ray diffractograms from Unit II and III samples. Five of the peaks fall between 9.3° and 9.9°2θ (laumontite, chabazite, stilbite, heulandite, and clinoptilolite), and there are additional peaks at 12.4° (phillipsite) and 15.8° (analcite).

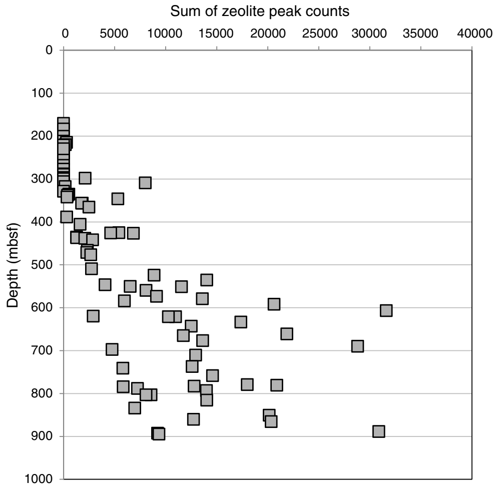

An additional style of diagenetic alteration is evident in Hole U1438D deeper than 600 mbsf, where a red and reddish brown stain has overprinted the dominantly grayish green, green, and black colors of the diagenetically altered rocks from overlying Units II and III. The reddish brown and red color is seen in four distinct intervals between 610 and 890 mbsf (Figure **F39**), where it affects almost exclusively the finer grained siltstone and mudstone (e.g., Figure **F24**). Deeper than 1200 mbsf, the red alteration becomes the dominant color in the fine-grained sedimentary rocks of Unit IV and at the bottom of Unit III (Figure **F39**). It is likely that the red coloration reflects a change in the oxidation state of iron, along with the formation of hematite at the expense of magnetite in the fine-grained sediments. This mineralogical change is not evident in the XRD data because the Fe oxide minerals are, in general, not well expressed. Targeted sampling and XRD analysis of closely spaced and varicolored horizons reveal no clear and systematic differences between the dominantly red layers compared to green, grayish green, and black layers of similar grain size in nearby parts of the core. All of the varicolored rocks are similarly dominated by the diagenetic minerals as described above.

Figure F39. Downhole changes in green-red reflectance (a*) measured by the SHMSL (0.6 m running average) and modal grain size from the core logs. Red alteration zones at base of hole affect only fine-grained rocks.

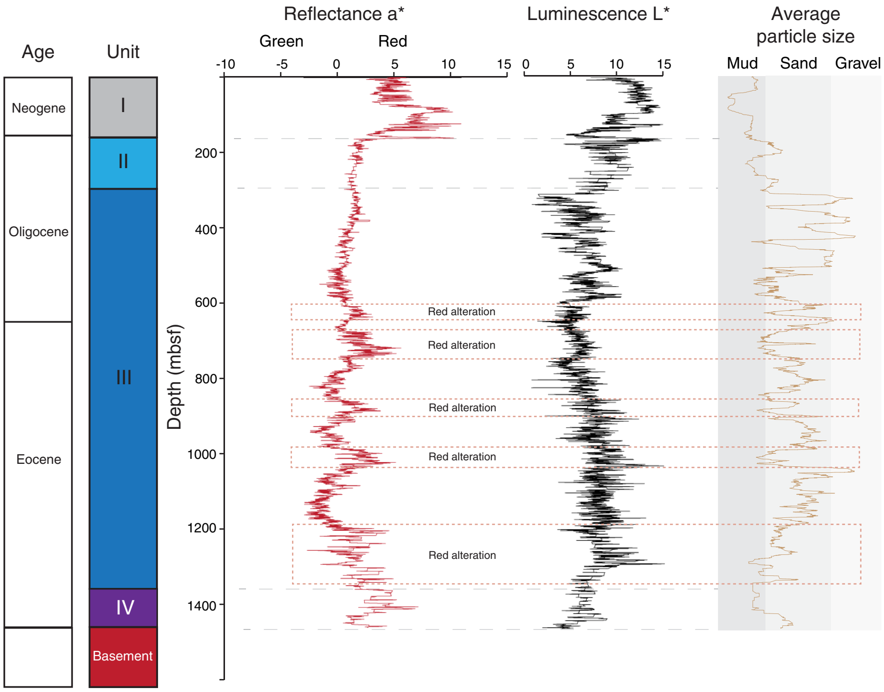

Additional downhole changes in mineralogy are evident in the bottom third of Unit III, in the transition to Unit IV. These changes are most clearly expressed in the appearance of quartz in the XRD data for most Unit III samples deeper than 1120 mbsf, compared to shallower parts of Unit III, where quartz is rarely or only occasionally present. Other minerals that appear sporadically in lower Unit III and in Unit IV, which were not present in the upper part of Unit III, include K-feldspar, prehnite, serpentine, and hematite.

The causes of the downhole changes in mineralogy in lower Unit III and Unit IV are uncertain. Some detrital quartz or microcrystalline silica grains have been observed in sandstones and mudstones in lower Unit III and in Unit IV, but their abundance appears to be no more than several percent, even in rocks where quartz dominates the XRD pattern. This suggests that abundant quartz deeper than 1120 mbsf may be cryptocrystalline silica. The source of the silica could have been biogenic or volcaniclastic or both. The emergence of quartz deeper than 1120 mbsf may also reflect changes in physical conditions to allow the formation of quartz from pore fluids in the rocks. Alternatively, the increase in quartz downhole near the bottom of Unit III could reflect changes in the dominant source of the sediment, to include a higher proportion of silt-and-finer detrital grains, perhaps of continental origin. In this case, the increase in quartz near the bottom of Unit III and in Unit IV would reflect a reversal of the trend that was observed from the unconsolidated muds of Unit I, where quartz was abundant, to the volcaniclastic sediments and sedimentary rocks of Units II and III, where quartz was mostly absent. This would imply a downhole trend to more quiet conditions of sediment deposition in Unit IV that prevailed in the time period after basement formation and prior to the flooding of the basin with the volcaniclastic sediment reflected in Unit III rocks. It is worth noting the similarity between the appearance of quartz in Unit IV immediately above the basement and late Eocene sedimentary cover of the basaltic basement recovered at ODP Leg 195 in the West Philippine Sea at Site 1201 (Salisbury et al., 2006).

Alteration minerals present in Unit 1 basalts are evident macroscopically in millimeter-scale veins and patches. The dominant alteration mineral identified by XRD is calcite. Macroscopic and petrographic observations show hematite is commonly associated with calcite. Veins and patches of soft, dark-colored minerals appear to be primarily saponite and/or vermiculite and less commonly chlorite or serpentine. The dark green and brown alteration mineral seen in thin section where it replaces olivine and groundmass glass (Figures **F33**, **F34**) is probably also a mixture of clay, chlorite, and serpentine. Pyrite is also present in the dark-colored, altered parts of the basalts. Alteration minerals occur in the basalts in the form of centimeter-scale veins or inclusions (Figure **F40**). These have textures that resemble plutonic igneous rocks or disaggregating cognate inclusions, but their mineralogy appears to be entirely hydrothermal. Thin section and XRD observations indicate that coarsely crystalline calcite, quartz, zeolite, and clay minerals are present (Figure **F35**).

Structural geology

Whereas inclined beds are present at various intervals cored at Site U1438 (Figure **F6**), faulted beds are restricted to the middle part of Unit II, around the overlap zone between the two holes (U1438B and U1438D) and are probably responsible for the 10 m difference between the depths of the marker horizon in the two cores. The deformed zone is characterized by strong drilling disturbance in both holes, but the original structures can be observed in a few of the cores. These consist of moderately dipping (40°–65°) planar structures that offset the inclined bedding (Figure **F21**). Most of the offsets show reverse (thrust) geometry with respect to the orientation of the bedding planes. The zone of deformation is 50–70 m wide and intersects Hole U1438B at a shallower level (20–40 m)

Figure F40. Coarse inclusions/veins of hydrothermal minerals in Unit 1 basalts.

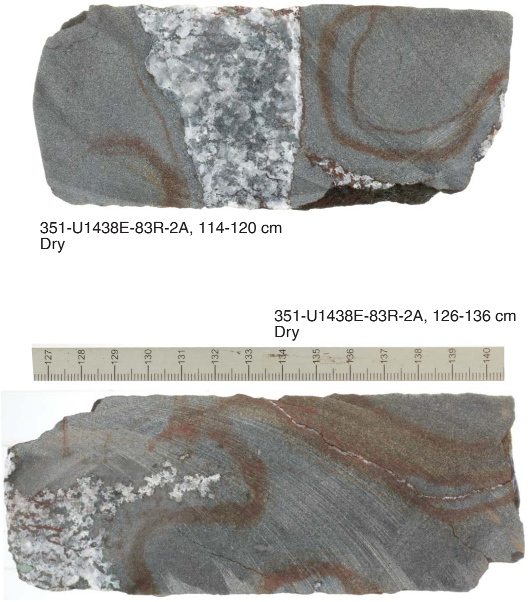

than in Hole U1438D, located northwest of Hole U1438B, suggesting a northwesterly dip to the structure at a moderate angle (40°–60°). The deformation and steep dips of the beds occur in the same area, suggesting either drag of bedding around a small reverse fault or slumping of partially lithified sediment to create small displacements and inclined beds.

Small 10 m reverse offsets of major reflectors are present in the southwest to northeast seismic sections near Site U1438 (Figure **F22**). These have approximately the same orientation and geometry (including dip direction) to account for the structures and offsets visible in Unit II.

The majority of Unit III to the bottom of Hole U1438D contains flat-lying beds and no faults. A few inclined beds were noted at widely spaced locations, but these tend to coincide with fine-grained rocks overlain by thick beds of sandstone and conglomerate (Figure **F6**), suggesting deformation occurred because of localized slumping and loading. Toward the bottom of Hole U1438D around 880 mbsf, bedding orientation changes rapidly, suggesting chaotic folding. Small reverse offsets on moderately dipping bedding planes become ubiquitous. However, veins are rare and fault gouge or cataclastic textures are absent, with most of the displacements occurring on very fine fractures that have now been filled by very fine secondary minerals.

Biostratigraphy

Preliminary biostratigraphic determination for Site U1438 is based on analysis of calcareous nannofossils, foraminifers, and radiolarians (Figures **F41**, **F42**; Table **T6**). All core catcher (CC) samples and some additional samples were examined (Tables **T7**, **T8**, **T9**, **T10**, **T11**, **T12**, **T13**).

Calcareous nannofossils

Hole U1438A

Three core catcher samples were recovered in Hole U1438A, all of which are barren of calcareous nannofossils. An additional two toothpick samples were analyzed from Samples 351-U1438A-1H-3W, 104–105 cm, and 2H-1W, 80–81 cm. Sample 1H-3, 104–105 cm, has low nannofossil recovery with rare occurrences of the genus *Ceratolithus*, mainly *Ceratolithus cristatus*. The range of these taxa is Pliocene to Pleistocene. Sample 2H-1, 80–81 cm, contains an abundant assemblage also composed mainly of Pliocene to Pleistocene species, including *Reticulofenestra minuta*, *Pseudoemiliania lacunosa*, and *Gephyrocapsa* spp. Significant reworking of Oligocene/Miocene species, such as *Sphenolithus ciperoensis* and *Cyclicargolithus abisectus*, was also found.

Hole U1438B

Of the 30 core catcher samples recovered from Hole U1438B, only 13 contain nannofossils with reliable ages. Calcareous nannofossils first appear in the lower section from Samples 351-U1438B-18H-CC to 30X-CC. Nannofossils are common to abundant and exhibit moderate to good preservation. Samples largely consist of Oligocene species such as *Reticulofenestra bisecta*, *C. abisectus*, *S. ciperoensis*, *Sphenolithus distentus*, and *Sphenolithus predistentus*. This interval therefore falls within nannofossil Zones NP25 and NP24.

Samples 18H-CC to 22F-CC (166.4–180.67 mbsf) were assigned to Zone NP25 based on the presence of both *S. ciperoensis* and *R. bisecta* (23.13 Ma) and the absence of *S. distentus* and *S. predistentus*. The last (youngest) occurrence (LO) of *R. bisecta* (23.13 Ma) defines the top of this zone, as does the LO of *S. ciperoensis* (Martini, 1971). The LO of *S. distentus* (26.84 Ma) defines the base. The assemblages include common to abundant *Triquetrorhabdulus carinatus*, *Discoaster deflandrei*, *C. abisectus*, *Cyclicargolithus floridanus*, and *Reticulofenestra stavensis*, with preservation ranging from moderate to good.

Samples 23F-CC to 30X-CC (189.44–257.08 mbsf) were assigned to Zone NP24 based on the presence of *S. distentus* and *S. ciperoensis*. The top of this zone is defined by the LO of *S. distentus* (26.84 Ma), and the base is defined by the first (earliest) occurrence (FO) of *S. ciperoensis* (29.62 Ma). The rare occurrence of *S. predistentus* is consistent with this zone (Gradstein et al., 2012). Nannofossils are generally rare to few and have poor to moderate preservation, possibly as a result of coarser grained sediment. In poorly preserved samples, it was occasionally not possible to distinguish between *S. distentus*, *S. ciperoensis*, and *S. predistentus* because most were observed without the base. However, in Sample 28X-CC, where preservation is better, *S. ciperoenesis* and *S. distentus* were recorded together.

Hole U1438D

Nannofossil marker species for Zones NP24 to NP19/NP20 were observed within the 72 core catcher samples of Hole U1438D, although the majority of samples are barren. Samples 351-U1438D-2R-CC (222.62 mbsf) to 8R-CC (269.84 mbsf) were assigned to Zone NP24 based on the presence of both *S. distentus* and *S. ciperoensis*. These samples yielded a typical Oligocene assemblage, such as *R. bisecta*, *C. abisectus*, *C. floridanus*, and *D. deflandrei*, with common abundance and moderate preservation. Other species that are present within this zone include *S. predistentus* in Samples 6R-CC to 8R-CC. *Discoaster tanii*, a typical Eocene marker species, was found in Sample 7R-CC and is considered to have been reworked.

Samples 9R-CC (280.66 mbsf) to 36R-CC (548.7 mbsf) were assigned to Zone NP23 based on the presence of *S. predistentus* and the absence of *S. ciperoensis*. The FO of *S. ciperoensis* (29.62 Ma) defines the top of this zone, whereas the base is defined by the LO of

Figure F41. Summary of microfossil information, Holes U1438B and U1438D. “Barren” refers to marker species.

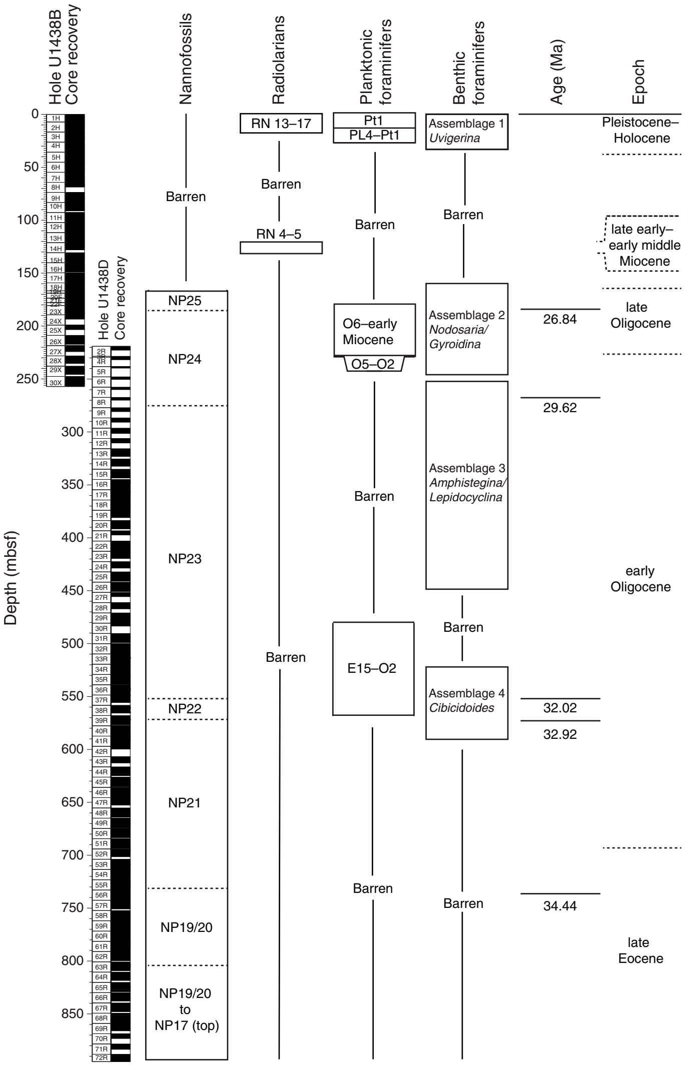

Reticulofenestra umbilica (32.02 Ma). Many core catcher samples in this zone are barren of nannofossils, including Samples 12R-CC to 14R-CC and 16R-CC to 24R-CC. All additional toothpick samples taken contained nannofossils assigned to Zone NP23.

Samples 37R-CC (555.71 mbsf) to 38R-CC (565.7 mbsf) were assigned to Zone NP22 based on the presence of *R. umbilica* and the absence of *Coccolithus formosus*. The base of this zone is defined by the LO of *C. formosus* (32.92 Ma), whereas the top is defined by the LO of *R. umbilica* (32.02 Ma). Abundance within this zone ranges between common and abundant, and specimens exhibit poor to good preservation.

Samples 39R-CC (576.79 mbsf) to 55R-5, 65–66 cm (729.58 mbsf), were assigned to Zone NP21 based on the presence of *R. umbilica* and *C. formosus* and the absence of *Discoaster saipanensis* and *Discoaster barbadiensis*. The top of this zone is defined by the LO of *C. formosus* (32.92 Ma), and the base is defined by the LO of *D. saipanensis* (34.44 Ma). Additional toothpick samples confirm the age. Nannofossil presence is rare to few, and preservation varies from poor to moderate. Nevertheless, *C. formosus* was found to be common and moderately preserved in each sample.

Samples 56R-1, 17–18 cm (733.07 mbsf), 57R-4, 103–104 cm (747.52 mbsf), and 62R-CC (799.63 mbsf) contained assemblages recognized as Zone NP19/NP20, based on the presence of Eocene marker species *D. saipanensis*, *D. barbadiensis*, and *Isthmolithus recurvus*. The base of this zone is defined by the FO of *I. recurvus* (36.97 Ma), and the top is defined by the LO of *D. saipanensis* (34.44 Ma). Samples 63R-CC to 72R-CC are barren. Only Sample 69R-4, 59–60 cm, from the lowermost part of Hole U1438D, yielded common to abundant nannofossils with poor to moderate preservation, including *D. saipanensis* and *D. barbadiensis*. With the absence of *I. recurvus*, these samples are constrained to the top of NP16 because of the presence of *Reticulofenestra reticulata*, which has its FO at 41.66 Ma (Gradstein et al., 2012).

Hole U1438E

Samples 351-U1438E-5R-4, 48–49 cm (881.24 mbsf), to 38R-2, 142–143 cm (1199.8 mbsf), contain generally few to barren occurrences of nannofossils with moderate to poor preservation. These samples were placed within Zones NP19/NP20 to NP17 (mid) because of the occurrence of *D. saipanensis*, *D. barbadiensis*, and *R. bisecta*. The upper boundary (Zone NP19/NP20) is defined by the LO of *D. saipanensis* and *D. barbadiensis*, and the lower boundary (NP17 [mid]) is defined by the FO of *R. bisecta* (38.25 Ma). All samples below this are barren of nannofossils.

Figure F42. Biostratigraphic and paleomagnetic age-depth plot against lithostratigraphic units, Site U1438. Ages based on the Gradstein et al. (2012) timescale.

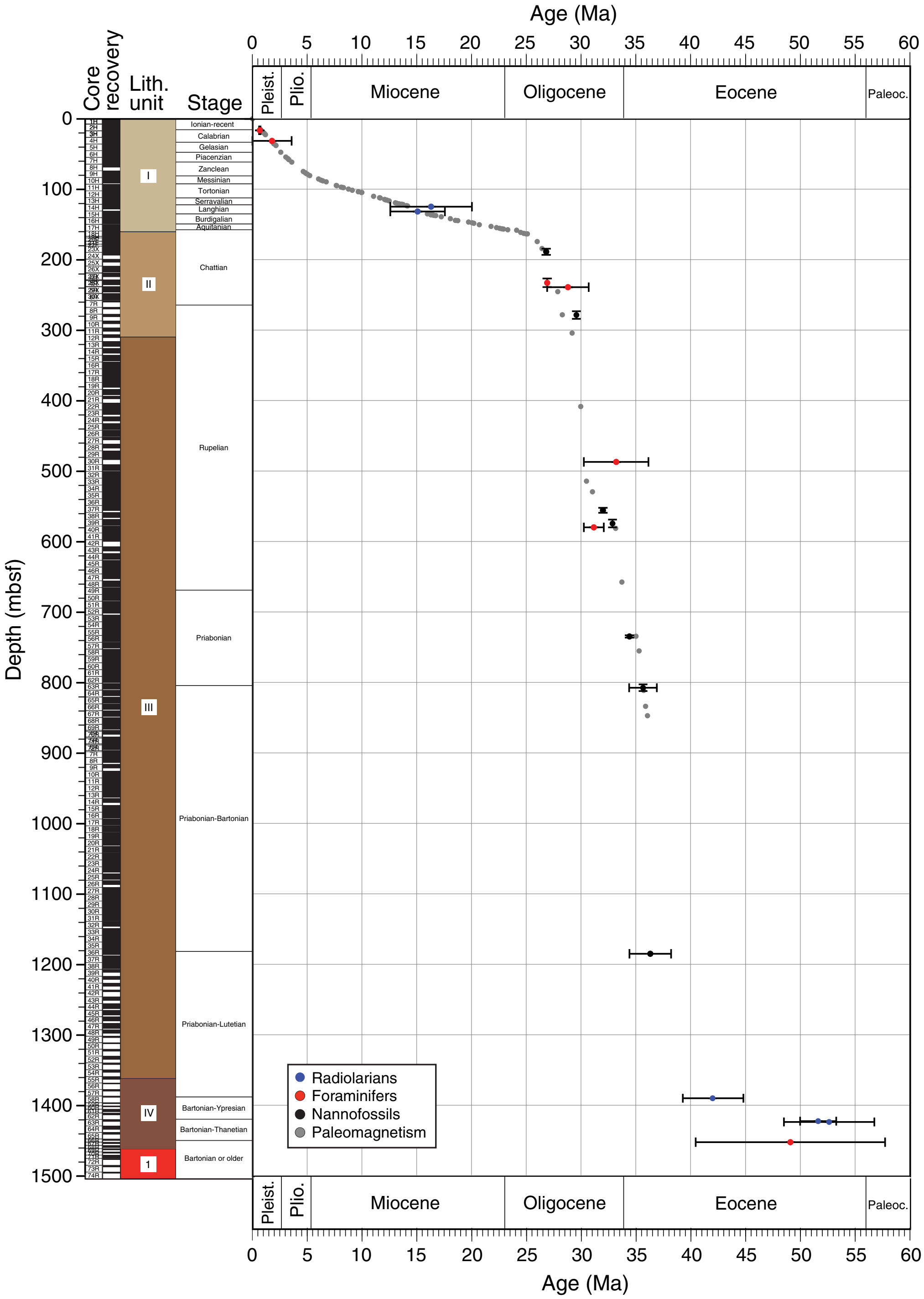

Planktonic foraminifers

Hole U1438A

No planktonic foraminifers occur in the top of Core 351-U1438A-1H (mudline sample), which is expected, as Site U1438 is below the current carbonate compensation depth (CCD). Sample 2H-5, 90–91 cm, was taken from a foraminifer-rich layer and comprises abundant planktonic foraminifers, including *Globorotalia tosaensis* and *Globorotalia hessi*. The ranges of these two species overlap in Zone Pt1a between 0.61 and 0.75 Ma (Gradstein et al., 2012). Other species present include *Globorotalia inflata*, *Globorotalia menardii*, *Globorotalia tumida*, and *Globorotalia truncatulinoides*. Sample 2H-CC contains a very sparse assemblage that includes *G. inflata*, a long-ranging extant taxon from Zone PL4 (3.59 Ma) to recent, and poorly preserved unidentifiable fragments. Preservation of planktonic foraminifers is generally good, with frosted shells common from secondary calcite overgrowth.

Table T6. Age-depth tie points of biostratigraphic marker events, Site U1438. Green = foraminifers, white = nannofossils, blue = radiolarians. **Download table in .csv format**.

Top depth (mbsf)	Bottom depth (mbsf)	Age top (Ma)	Age bottom (Ma)	Zone
Hole U1438B-				
12.51	12.52	0.61	0.75	Pt1a
27.56	27.57	0	3.59	PL4–recent
120.90	121.20	12.6	20.05	RN2–RN5
127.66	127.93	12.6	17.59	RN4–RN5
180.65	189.44	26.84	26.84	Base NP25
223.00	235.2	26.93	26.93	Base O6
235.20	235.36	26.93	30.72	Opima O2–O5
Hole U1438D-				
269.84	280.66	29.62	29.62	Base NP24
483.36	483.49	30.28	36.18	O2–E15
548.70	555.71	32.02	32.02	Base NP23
565.70	576.79	32.92	32.92	Base NP22
576.14	576.48	30.28	32.1	O2–E15
729.58	733.07	34.44	34.44	Base NP21
799.63	809.11	34.44	36.97	NP20/NP19
Hole U1438E-				
1181.73	1181.74	34.44	38.25	NP20–NP17 (top)
1387.51	1387.53	40.65	46.21	RP12–RP14
1419.73	1419.75	50.05	53.35	RP8
1420.84	1420.86	48.57	56.83	RP7 (top)–RP9
1449.35	1449.38	40.49	57.79	P4c–E11

Table T7. Nannofossil range chart, Holes U1438A and U1438B. **Download table in .csv format.**

Table T8. Nannofossil range chart, Holes U1438D and U1438E. **Download table in .csv format.**

Table T9. Foraminifer range chart, Holes U1438A and U1438B. **Download table in .csv format.**

Table T10. Foraminifer range chart, Holes U1438D and U1438E. **Download table in .csv format.**

Table T11. Radiolarian range chart, Hole U1438A. **Download table in .csv format.**

Table T12. Radiolarian range chart, Hole U1438B. **Download table in .csv format.**

Table T13. Radiolarian range chart, Hole U1438E. **Download table in .csv format.**

Hole U1438B

Sample 351-U1438B-2H-1W, 68–71 cm, is a toothpick sample taken from a foraminifer-rich horizon and consists of dominant planktonic foraminifers, including *G. inflata* (ranging from Zone PL4, 3.59 Ma, to recent) and the long-ranging species *Pulleniatina obliquiloculata*, *Globigerina bulloides*, *G. tumida*, *G. truncatulinoides*, and *Neogloboquadrina pachyderma*.

Sample 2H-CC contains a sparse assemblage consisting of indeterminate forms and *G. inflata*, *P. obliquiloculata*, and *G. tumida*. Sample 4H-1W, 136–137 cm, is a toothpick sample taken at the deepest (earliest) foraminifer-rich horizon and consisting of abundant planktonic foraminifers, including the stratigraphically important *G. inflata* (3.59 Ma to recent), and the long-ranging Neogene species *G. bulloides*, *G. tumida*, *G. crassaformis*, *G. menardii*, *Orbulina universa*, and *Sphaeroidinella dehiscens*.

Samples 4H-CC to 20F-CC are barren of foraminifers, except for one unidentifiable planktonic specimen in Sample 18H-CC. Samples 21F-CC and 22F-CC contain sparse planktonic foraminifers largely indeterminate but including *Paragloborotalia nana*, which is long-ranging from the Eocene to late Miocene (Pearson et al., 2006). Sample 22F-CC also contains a well-preserved specimen of *Paragloborotalia mayeri*, which ranges from within Oligocene Zone P22 (~27–23 Ma), according to Bolli and Saunders (1985), to Miocene Zone M11 (10.46 Ma), according to Gradstein et al. (2012). *Catapsydrax unicavus*, ranging from late Eocene Zone P14 to early Miocene Zone N6 (Pearson et al., 2006), is the only identifiable species to occur in Samples 24X-CC and 26X-CC.

Sample 27X-CC contains a slightly more diverse assemblage of planktonic foraminifers, including a very well-preserved specimen of *Globoquadrina praedehiscens*, which ranges from Oligocene Zone P22 (26.93 Ma) to Miocene Zone N6 (Kennett and Srinivasan, 1983), indicating this sample is no older than late Oligocene. This sample is likely within Zone O6 (base of Zone P22), as the sample below (28X-CC) is assigned to Zones O2–O5. The sample also includes the long-ranging *C. unicavus* and *Globoquadrina venezuelana*. The following Sample 28X-CC contains a sparse assemblage of largely unidentifiable etched and poorly preserved planktonics but also well-preserved *Paragloborotalia opima-nana* group specimens ranging up to ~300 µm in size. According to Bolli and Saunders (1985), specimens >320 µm are restricted to the Oligocene *P. opima* range, which is from Zone O2 (30.72 Ma) to Zone O5 (26.93 Ma) (Gradstein et al., 2012).

Hole U1438D

Samples 351-U1438D-2R-CC to 9R-CC are either barren or contain very few broken and unidentifiable planktonic foraminifers. Toothpick Sample 10R-2A, 44–45 cm, was taken from a fine-grained sand interval containing common poorly preserved to moderately well-preserved species. These include *Globigerina euapertura*, ranging from late Eocene Zone P16/P17 (<35.71 Ma) to early Miocene Zone N7 (>16.36 Ma) (Bolli and Saunders, 1985), and the long-ranging *C. unicavus*. Samples 10R-CC to 28R-CC are barren, except for a solitary broken specimen in Sample 28R-CC.

Sample 29R-CC contains only rare, poorly preserved, yellow planktonics that include solitary specimens of *Turborotalia ampliapertura*, which ranges from Eocene Zone E15 (36.18 Ma) (Pearson et al., 2006) to Oligocene Zone O2 (30.28 Ma) (Gradstein et al. 2012), and the long-ranging *Catapsydrax dissimilis* (Oligocene to early Miocene). The species *Globigerina praebulloides* (Eocene to Miocene) occurs in Sample 31R-CC, and *G. euapertura* (late Eocene Zone P16/P17 to early Miocene Zone N7) occurs again in Sample 33R-CC, and then the samples are barren until Sample 38R-CC, which contains common and well-preserved planktonic foraminifers. The specimens here are largely composed of *T. ampliapertura* (36.18–30.28 Ma), which could be indicative of the *T. ampliapertura* highest occurrence Zone O2 (Gradstein et al., 2012) between 30.28 and 32.10 Ma, although it could range into the earlier Oligocene. Other species in this sample include *C. dissimilis*, *G. euapertura*, *G. praebulloides*, and *Dentoglobigerina pseudovenezuelana*, which ranges from Eocene Zone E14 (38.25 Ma) to possibly Oligocene Zone O5 (26.93 Ma), according to Pearson et al. (2006).

Sample 39R-CC contains a very sparse and poorly preserved assemblage including the long-ranging *C. unicavus* and *G. euapertura*, and Sample 43R-CC contains the long-ranging *G.*

praebulloides, and therefore age diagnosis beyond Eocene–Oligocene is not possible from planktonic foraminifers alone. All other samples down to 72R-CC are barren of planktonic foraminifers.

Hole U1438E

Sample 351-U1438E-28R-CC contains five specimens of planktonic foraminifers, which are mostly broken and unidentifiable to species level. However, one specimen appears to belong to the long-ranging genus *Catapsydrax* (early Eocene to middle Miocene). The only other sample to contain foraminifers is Sample 66R-CC. This sandy sample contains two specimens of very poorly preserved, partially recrystallized planktonic foraminifers. One specimen appears to belong to the genus *Acarinina*, with its characteristic robust wall and coarse wall texture, although the lack of a visible aperture precludes definite identification (Figure **F43**). The overall quadrate test shape and subangular periphery indicates it probably belongs to the species *Acarinina bullbrooki* (Zones E7–E11; 50.2–40.49 Ma), or possibly *Acarinina soldadoensis* (Zones P4c–P9; 57.79–44.49 Ma) (Pearson et al., 2006), although the profile of the last chamber is somewhat angular, as in *A. bullbrooki.*

Figure F43. SEM (upper) and reflected light (lower) images of *Acarinina* sp. (Sample 351-U1438E-66R-CC).

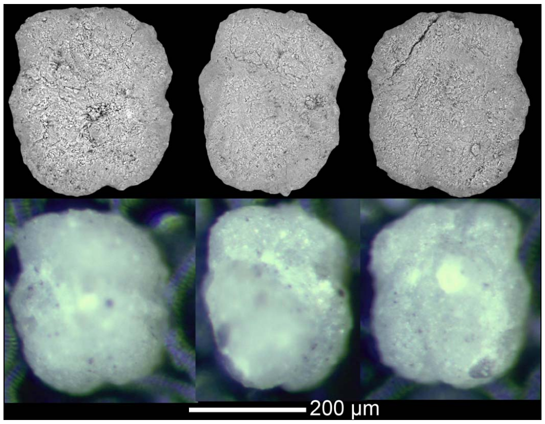

Benthic foraminifers

The occurrence of benthic foraminifers is generally low and sporadic, with many barren samples. However, some broad assemblage zones can be defined, and the paleoenvironmental implications presented below are based on the most common species and on preservation state. The assemblage zones are listed in order of total depth (mbsf), rather than by hole (Figure **F41**). Paleobathymetric and paleoenvironmental designations are based on published studies, such as van Morkhoven et al. (1986), Kaiho (1992), and Holbourn et al. (2013).

Assemblage 1: *Uvigerina*

Depth: 0–28 mbsf
Age: Quaternary (0–1.6 Ma)
Samples: 351-U1438A-1H to mudline; 351-U1438A-2H-5W, 90–91 cm; 351-U1438B-2H-1W, 68–71 cm; 351-U1438B-4H-1W, 136–137 cm

Characteristics

The relative proportion of benthic foraminifers is small compared to planktonic foraminifers. This assemblage is composed of relatively well preserved smaller benthic foraminifers, including the species *Rhizammina* sp., *Reophax* sp., *Nonionella* sp., and *Saccammina* sp. in the core-top mudline sample and *Uvigerina peregrina*, *Cibicidoides mundulus*, *Planulina wuellerstorfi*, *Uvigerina hispida*, *Nodosaria* spp., *Quinqueloculina* sp., *Cibicidoides* spp., *Fursenkoina complanata*, *Melonis barleeanum*, *Stilostomella* spp., *Fissurina* sp., *Eggerella bradyi*, *Gyroidina* sp., and *Globocassidulina subglobosa*. The lithology is predominantly clay, and several samples are barren of foraminifers.

Remarks

The surface mudline sample contains predominantly (although not exclusively) agglutinated species, as Site U1438 is currently below the CCD. The occurrence of agglutinated foraminifers is extremely low in the rest of the Site U1438 samples, which may be an indication that agglutinated foraminifers usually disaggregate after burial and are not preserved. The sporadically high abundances of calcareous species in some samples in this assemblage could either be related to CCD changes or possibly rapid burial due to gravity flows. There is, however, no evidence of transported shallow-water (shelf) benthics and no obvious sorting of foraminifers on test size and shape that may be indicative of gravity flows. The overlapping depth ranges of these species in the modern ocean is generally considered to be lower bathyal to upper abyssal (1000–3000 m water depth), although this is primarily controlled by the level of the CCD (currently about 4.5 km in the Pacific Ocean) and organic carbon flux, controlled partly by surface ocean productivity and intermediate water mass properties that are globally changeable. These parameters are considered to have been highly variable over the Quaternary (see Pälike et al., 2012, for Pacific CCD changes). Thus, using benthic foraminifers for detailed paleodepth reconstructions in deeper water (bathyal and deeper) is not generally regarded as accurate (e.g., Holbourn et al., 2013). Further work is needed to ascertain if this assemblage is primarily related to environmental changes (CCD and/or organic carbon flux) or lateral transport.

Barren interval

Depth: 35–159 mbsf
Age: Pleistocene–late Oligocene (2–24 Ma)
Interval: 351-U1438B-4H-CC to 17H-CC

This interval includes fine clays and silts with rare to common fish teeth, likely deposited below the CCD.

Assemblage 2: *Nodosaria/Gyroidina*

Depth: 166–245 mbsf
Age: mid-Oligocene (~25.5–28 Ma)
Intervals: 351-U1438B-18H-CC to 29X-CC; 351-U1438D-2R-CC and 3R-CC

Characteristics

This assemblage zone contains a number of samples, and although the overall diversity is quite high, species diversity in individual samples is generally less than 5. Planktonic foraminifers are usually rare. Preservation is good, although some specimens are broken. The lithology is predominantly clay. The most common species in the samples include *Cibicidoides* spp., *Nodosaria* spp., *Globocassidulina moluccensis*, and *Gyroidina* sp. Other species present are *Pullenia* sp., *Nodosaria longiscata*, *Uvigerina* sp., *Trifarina* sp., *Nuttalides* sp., *Stilostomella* spp., *Glandulina* spp., *Pleurostomella subcylindrica*, *Cibicidoides grimsdalei*, *Oridorsalis umbonatus*, *Cribrostomoides subglobosus*, *Pullenia simplex*, *Sphaeroidina bulloides*, *Stilostomella abyssorum*, *Karrerulina* sp., *Rhabdammina* sp., *Cibicidoides laurisae*, *C. mundulus*, *Cibicidoides havanensis,* and *Lagena sulcata*.

Remarks

The benthic foraminifers are typically found at lower bathyal to abyssal depths (1000 to >4000 m water depth), although as stated above, the primary control on depth preferences for deep-sea foraminifers is organic carbon flux and the level of the CCD. The low species abundances may be related to sediment dilution due to high sedimentation rates. However, the very low proportion of planktonic foraminifers may suggest that these samples have been affected by dissolution and therefore deposited below or very near to the CCD, which was at ~4.7 km during the mid-Oligocene in the east Pacific (Pälike et al., 2012).

Assemblage 3: *Amphistegina/Lepidocyclina*

Depth: 257–430 mbsf
Age: early Oligocene (~28–30.2 Ma)
Samples: 351-U1438B-30X-CC; 351-U1438D-12R-CC; 351-U1438D-13R-CC; 351-U1438D-14R-CC; 351-U1438D-16R-CC; 351-U1438D-17R-CC; 351-U1438D-22R-CC; 351-U1438D-23R-3A, 95–98 cm; 351-U1438D-23R-CC; 351-U1438D-24R-2A, 105–107 cm

Characteristics

Very sparse, poorly preserved, grayish/yellowish, commonly etched specimens of species belonging to the genera *Amphistegina* and *Lepidocyclina*. These specimens always occur within sandy intervals.

Remarks

Both genera are "larger" benthic foraminifers that produce a complex wall structure of numerous chambers used to house photosynthetic symbionts. These species therefore show strong evidence of being transported from a shallow (<200 m?) reef environment along with the sands. More detailed thin section analysis is required to speciate these specimens, although the genera are long-ranging from Eocene to Miocene.

Barren interval

Depth: 450–510 mbsf
Age: early Oligocene (~31 Ma)
Interval: 351-U1438D-24R-CC to 31R-CC

This interval contains predominantly fine sands.

Assemblage 4: *Cibicidoides*

Depth: 520–587 mbsf
Age: early Oligocene (~31–33.2 Ma)
Samples: 351-U1438D-32R-CC, 36R-CC, 38R-CC, 39R-CC

Characteristics

Only four samples in this interval contain foraminifers, and these are in low abundance. However, there are a number of species present, including *Cibicidoides pachyderma*, *C. havanensis*, *C. laurisae*, *Stilostomella* sp., *Nonionella* sp., *Rhabdammina* spp., *Bathysiphon* sp., *Sigmavirgulina tortuosa*, *C. subglobosus*, *P. simplex*, *Stilostomella* sp., and *Haplophragmoides* sp. Planktonic foraminifers occur in low abundance in some samples. The lithology is clay, apart from Sample 351-U1438D-38R-CC, which contains fine sand.

Remarks

C. pachyderma may be of some stratigraphic significance here, as it ranges from early Oligocene to recent (Holbourn et al., 2013). The majority of species are typical for bathyal to abyssal assemblages. However, Holbourn et al. (2013) list *S. tortuosa* and *C. pachyderma* as neritic to upper bathyal, so it is possible that some transportation of material from shallower water has occurred in this sandy sample. It is unlikely that the paleobathymetry of this site was bathyal at this time because of the presence of the abyssal *C. havanensis* in this assemblage zone (Holbourn et al., 2013). The occurrence of a number of well-preserved agglutinated *Rhabdammina* spp. in Sample 32R-CC is interesting because of the absence of abundant agglutinated forms in other samples. It is possible that a higher proportion of silica from ash has helped preserve the fauna by replacing the primary organic cement.

Barren interval

Depth: 597–1460.9 mbsf
Age: Eocene to possibly latest Paleocene (>33.5 Ma)
Intervals: 351-U1438D-40R-CC to 72R-CC; 351-U1438E-4R-CC to 68R-CC

Other than a few poorly preserved benthics and planktonics in Samples 351-U1438D-42R-CC, 43R-CC, and 45R-CC and 351-U1438E-4R-CC and 28R-CC, all samples in this interval are barren. The lithology largely ranges from coarse sands to pinkish and grayish clays, passing into darker red and finally brown clay. It is possible that the significantly shallower position of the CCD in the Pacific in the Eocene, compared to the Oligocene, impacted the preservation potential of foraminifers in these samples. The single identifiable benthic foraminifer to occur in this interval, in Sample 351-U1438E-4R-CC, is *C. subglobosus*, an agglutinated (noncalcareous) species that typically inhabits bathyal to abyssal depths in the modern ocean (Holbourn et al., 2013).

Radiolarians

Hole U1438A

All core catcher samples from Hole U1438A were examined. Only Quaternary radiolarians are present in the studied samples. Additionally, a relatively abundant and well-preserved radiolarian assemblage was recovered from the mudline sample, consistent with a water depth below the CCD. However, radiolarian abundance and preservation decrease drastically downhole. Samples 351-U1438A-1H-CC and 3H-CC are barren of radiolarians or contain only occasional radiolarian fragments. Sample 2H-CC is assigned to the Pleistocene–Holocene RN13–RN17 zones based on the presence of *Lamprocyrtis nigriniae*, which corresponds to the 1.26–0 Ma interval.

Hole U1438B

Rare, moderately preserved Quaternary radiolarians are present in Sample 351-U1438B-1H-CC. Samples 2H-CC to 11H-CC are generally barren of radiolarians, and only very rare and poorly preserved specimens were observed in that interval. Radiolarians become slightly more abundant and better preserved in Samples 12H-CC to 15H-CC. The only dated radiolarian record from this interval is 17.59–12.6 Ma based on the presence of *Calocycletta costata*, which suggests assignment to the late early Miocene to early middle Miocene RN5 or RN4 Zones. No identifiable faunas were found in, or deeper than, Sample 16H-CC. Radiolarians are present in some samples, but they are typically recrystallized and have suffered significant dissolution.

Hole U1438D

Samples 351-U1438D-2R-CC to 72R-CC are generally barren of radiolarians or only contain very rare and poorly preserved specimens, which have typically been recrystallized and suffered extreme dissolution.

Hole U1438E

Radiolarian occurrences are low in the majority of samples from Hole U1438E. The skeletons of most recovered radiolarians are recrystallized as quartz, clay minerals, or zeolites and filled by matrix or cement.

Samples from Cores 351-U1438E-4R through 53R are mostly barren of radiolarians, except for a few samples. These samples contain rare and poorly preserved indeterminate specimens, which have typically been recrystallized and suffered extreme dissolution.

Samples from Cores 54R through 68R yielded slightly more abundant but also indeterminable radiolarian assemblages, except for Samples 58R-2, 47–49 cm, 63R-1, 23–25 cm, and 63R-1, 78–81 cm, which contain moderately preserved Paleogene radiolarians.

Sample 58R-2, 47–49 cm, is characterized by the occurrence of *Eusyringium fistuligerum*, *Lithocyclia ocellus*, *Periphaena tripyramis*, *Phormocyrtis striata striata*, *Sethochyrtis* cf. *triconiscus*, *Thyrsocyrtis rhizodon*, and *Thyrsocyrtis triacantha*, which indicates a Lutetian–early Bartonian age (Zone RP12–RP14; 46.21–40.65 Ma).

Sample 63R-1, 23–25 cm, yielded an assemblage characterized by the presence of *Buryella tetradica*, *Calocycloma castum*, *Lamptonium fabaeforme*, *Phormocyrtis* cf. *striata exquisita*, *Theocotyle cryptocephala*, *Theocotylissa ficus*, and *Theocotyle nigrinae* (Figure **F44**), which indicates a Ypresian age (Zone RP8; 53.35–50.05 Ma).

The lowest sample yielding determinable radiolarians was Sample 63R-1, 78–81 cm (Figure **F44**). The assemblage contains radiolarian genera characteristic of the latest Paleocene–early Eocene. Based on the presence of *Buryella* spp., *Phormocyrtis* spp., *Podocyrtis* spp., and *Theocotylissa* spp., the age of the sample was tentatively interpreted as latest Thanetian–Ypresian (RP7 [top]–9; 56.83–48.57 Ma).

Cores 64R through 69R contain mostly indeterminable radiolarians.

Figure F44. Scanning Electron Microscope pictures of radiolarians from Hole U1438E (Sample 63R-1W, 23–25 cm; early Eocene): 1, 2. *Buryella tetradica*; 3, 4. *Calocycloma castum*; 5. *Lamptonium fabaeforme*; 6. *Phormocyrtis* cf. *striata exquisita*; 7. *Theocotylissa ficus*; 8. *Theocotyle nigrinae*. (Sample 63R-1W, 78–81 cm; latest Paleocene–early Eocene): 9. *Buryella* sp.; 10. *Phormocyrtis* sp.; 11. *Podocyrtis* sp.; 12. *Theocotylissa* sp.

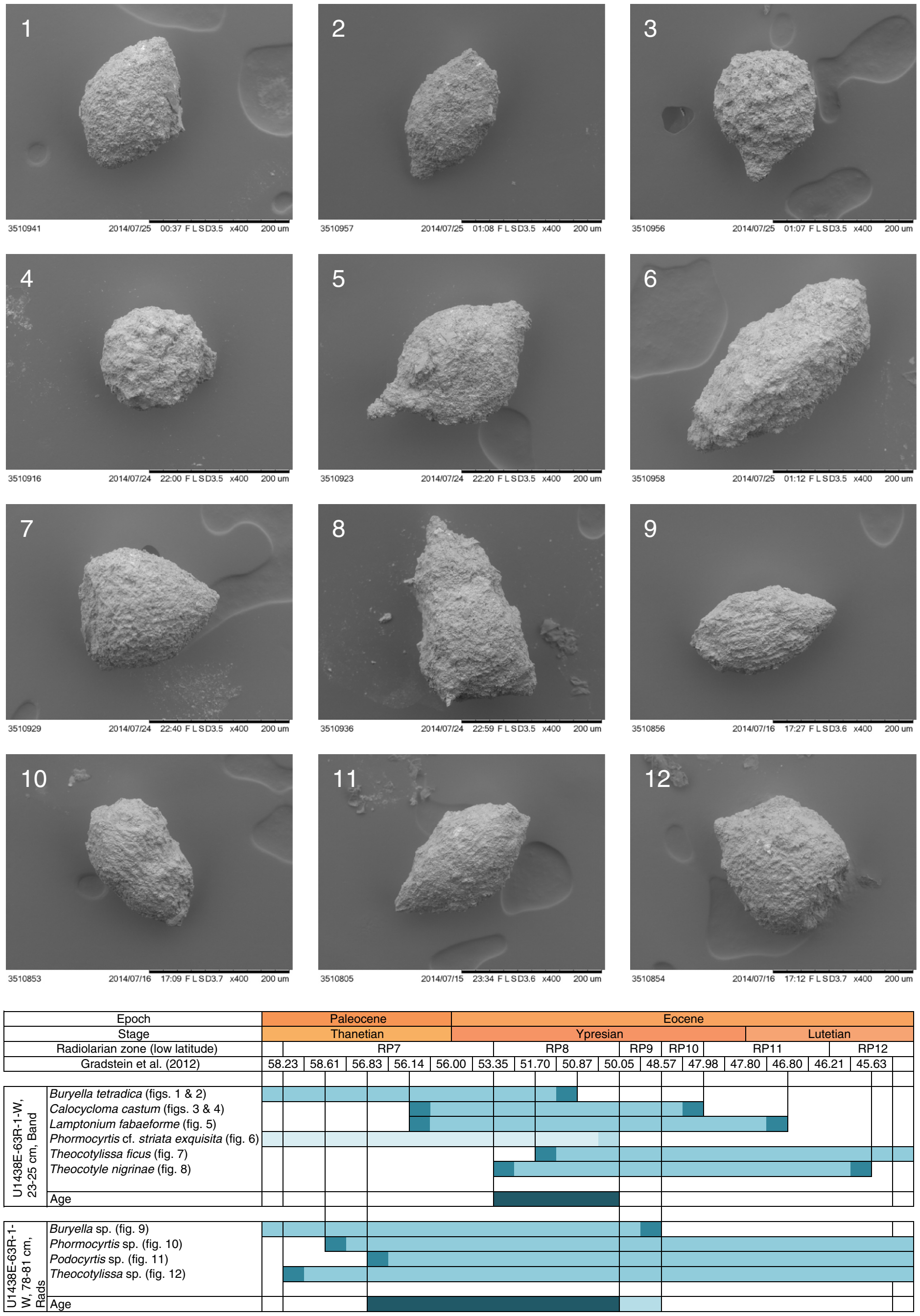

Geochemistry

Interstitial water

To determine the inorganic constituents of interstitial water (IW), 67 whole-round samples were collected at Site U1438 (see the **Expedition 351 methods** chapter for sampling procedures [Arculus et al., 2015a]). Aliquots of IW were used for shipboard analyses, and the remaining fluid was sampled for shore-based analyses, following protocols specified by individual scientists. From cores recovered in Hole U1438B, 17 samples were taken in lithostratigraphic Unit I and 9 samples were taken in Unit II (see **Core descriptions** and Figure **F45** for lithostratigraphic unit designations). In Hole U1438D, 6 samples were taken in Unit II and 35 were taken in Unit III. Only 4 samples were taken from Unit III in Hole U1438E. Where possible, IW samples were taken in the middle of the core; however, sample locations were adjusted to accommodate changes in lithology, drilling disturbance, and core recovery. In Hole U1438B, some lithologies were too indurated to yield pore water, namely the fine-grained sediments at the bottom of Unit I (Figure **F45**).

Figure F45. Alkalinity, pH, redox potential, sulfate, phosphate, and ammonium depth profiles, Site U1438. Arrowed values = seawater data at ~6 m below sea surface.

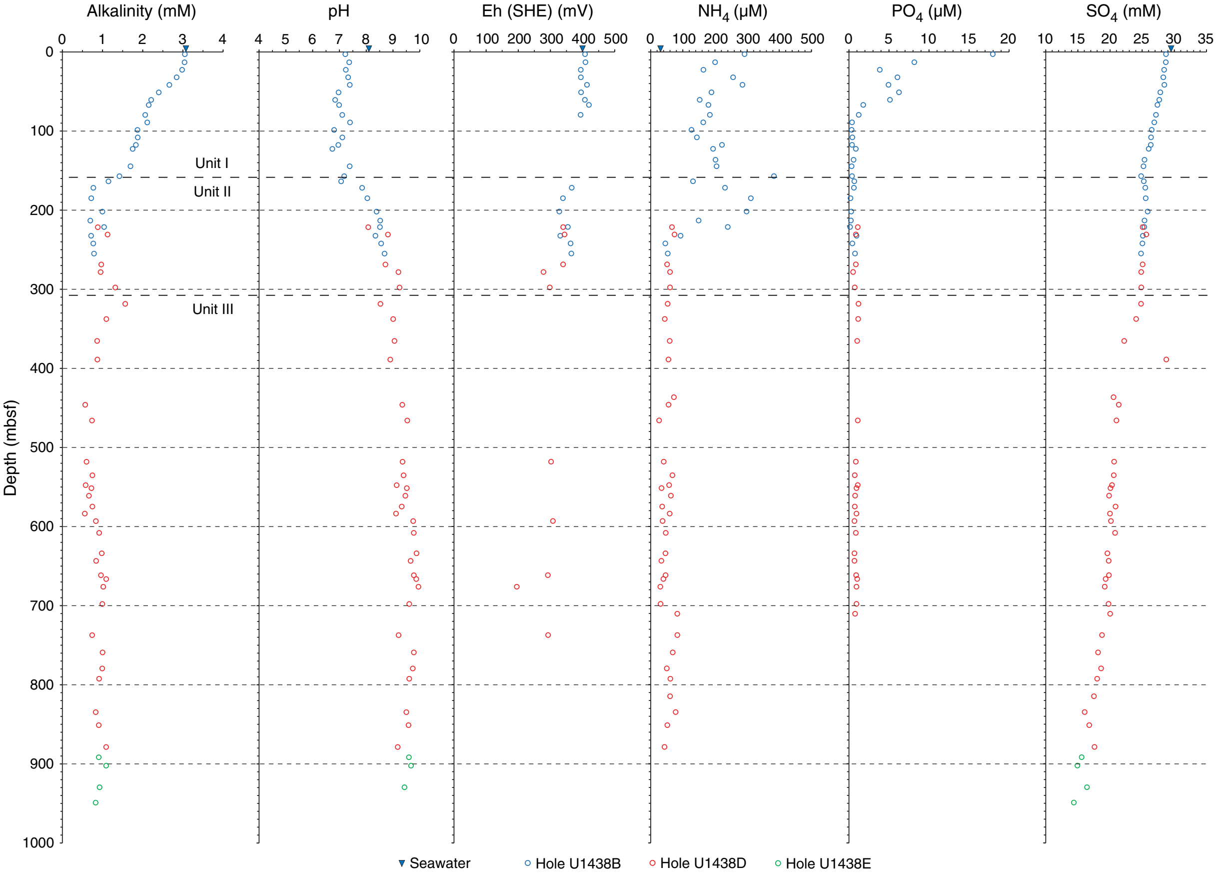

On 10 June 2014, a seawater sample was taken at ~6 m below the sea surface and analyzed for comparison with IW (Table **T14**). Seawater values are plotted as arrows at the top of the IW downhole profiles.

Alkalinity and pH

Depth profiles of alkalinity and pH are shown in Figure **F45**. In Unit I (0 to ~160 mbsf), alkalinity decreases downhole from 3.05 to 1.42 mM, whereas pH is nearly constant at ~7, suggesting predominantly carbonate alkalinity. In Unit II (~160 to ~310 mbsf), alkalinity remains nearly constant, averaging ~0.92 ± 0.19 mM, whereas pH increases to a maximum of 9.25 at the bottom of Unit II. This indicates that aqueous carbonate species (HCO_3^- and CO_3^{2-}) no longer constitute the major alkalinity component. Specifically, a downhole increase in aqueous silicates and borates results in a pH increase and consistently low alkalinity values. In Unit III (~310 to ~1360 mbsf), alkalinity remains relatively stable, varying from 0.56 mM at 583.65 mbsf (Section 351-U1438D-40R-5) to 1.09 mM at 878.68 mbsf (Section 71R-1). pH slightly increases to a maximum of 9.95 at 676.18 mbsf (Section 351-U1438D-50R-2) and then decreases to 9.43 at 929.65 mbsf (Section 351-U1438E-10R-3).

Redox potential, sulfate, phosphate, and ammonium

The redox potential (Eh) of IW was also measured (see the **Expedition 351 methods** chapter [Arculus et al., 2015a]) (Figure **F45**). The redox potential decreases from ~400 mV (Unit I) to ~300 mV (Unit II). Because of the limited IW volume, only five measurements were made in Unit III, yielding a consistent redox potential of ~300 mV with the exception of ~676 mbsf (195 mV). The redox potentials in Holes U1438B and U1438D are relatively oxidizing and in agreement with the relatively high sulfate concentrations, which range from 28.7 mM (~3 mbsf) to 14 mM (~949 mbsf).

Table T14. Chemical data of seawater collected 6 m below the sea surface, 10 June 2014. * = measured by ion chromatography; † = measured by spectophotometer; ‡ = measured by inductively coupled plasma–atomic emission spectroscopy. **Download table in .csv format.**

Analyte	Result	Unit
pH	8.11	
Alkalinity	3.085	mM
Salinity	36	
Eh (SHE)	400	mV
Cl (titration)	547.92	mM
Cl*	573.64	mM
Br*	0.89	mM
SO_4*	29.49	mM
Na*	484.84	mM
K*	8.17	mM
Ca*	12.61	mM
Mg*	54.05	mM
$NH_4^\dagger$	30.32	µM
$B^\ddagger$	516.65	µM
$Li^\ddagger$	25.27	µM
$Si^\ddagger$	57.77	µM
$Sr^\ddagger$	88.16	µM

Ammonium concentrations vary between 127.1 and 383.4 µM in the uppermost 220 mbsf and do not show a clear trend (Figure **F45**). Below this depth, ammonium concentrations are relatively stable and low (~26–78 µM). Phosphate concentrations decrease sharply from ~18.0 µM at the surface to 0.4 µM at 100 mbsf and remain around 0.4 µM deeper than 100 mbsf. The depletion of ammonium and phosphate deeper than 250 mbsf is best explained by a sharp downhole decline of microbial activity.

Salinity, chloride, bromide, sodium, potassium, calcium, and magnesium

Salinity varies from 36.5 to 37.5 throughout Unit I, slightly increases to 39 in Unit II, and then rapidly increases in Unit III to the maximum value of 47 at the bottom of Hole U1438D (Figure **F46**). The maximum in salinity is mainly due to a downhole increase in Ca concentration, reaching a maximum concentration ~27 times greater than seawater.

Chloride concentrations vary from ~560 to 548 mM in Unit I. It is possible that the clay content at the base of Unit I, in particular, acts as a semipermeable membrane impeding diffusion of the anions across the Unit I/II boundary, causing a lower concentration in Unit I (see discussion in Egeberg et al., 1990). Chloride concentrations increase through Unit II and III and reach a maximum concentration of 675.61 mM at the base of Hole U1438D. Bromide concentrations range from 0.85 to 1.08 mM, three orders of magnitude less than that of chloride, but exhibit a similar trend to the latter with depth (Figure **F46**). The downcore increase in chloride and bromide concentrations is most likely due to hydration reactions in the mineral lattice, which preferentially incorporates hydroxyl anions rather than chloride and bromide, resulting in chloride and bromide enrichment in IW (Egeberg et al., 1990; Wei et al., 2008). This enrichment is in agreement with the formation of secondary hydrated mineral phases such as zeolites identified by XRD (see **Core descriptions**).

Sodium concentrations decrease slightly from ~479.6 to 445.2 mM in Unit I (Figure **F46**), increase slightly at the Unit I/II boundary (~164 mbsf), and then progressively decrease to a minimum of 127.1 mM at ~902 mbsf (Core 351-U1438E-7R). Overall, Na concentrations decrease downcore by ~66%. Potassium behaves similarly to Na in that the concentrations decrease until the Unit I/II boundary, increase in the first three cores of Unit II, and then decrease to a minimum value of 1.59 mM at ~879 mbsf (Core 351-U1438D-71R) (Figure **F46**).

Calcium concentrations increase linearly from ~11.5 mM (3 mbsf) to ~271.5 mM (~298 mbsf; Core 351-U1438D-49R), and continue to increase linearly, at a higher rate, reaching a maximum of ~272 mM (~666 mbsf), below which concentrations vary within a narrow range of 246–272 mM to ~949 mbsf (Figure **F46**). Magnesium concentrations decrease linearly downhole from 53 mM (~3 mbsf) to depletion in the aqueous phase at ~437 mbsf (Figure **F46**). To 389 mbsf, Ca and Mg concentration profiles show opposite trends and no clear differences across the interface of Units I and II, indicating that diffusion and ion exchange influence their mobility in the IW. The synchronous increase in Ca and decrease in Mg concentrations was observed in western Pacific marginal basins and attributed to the diagenesis of volcaniclastic sediments (e.g., Gieskes and Lawrence, 1981; Egeberg et al., 1990; Torres et al., 1995; Salisbury, Shinohara, Richter, et al., 2002). Leaching of Ca from the volcanic glass in the sediment is a potential source for Ca in IW, and Mg and K presumably replace Ca through ion exchange and diffusion into the sediments.

Figure F46. Salinity, chloride, bromide, sodium, potassium, calcium, and magnesium depth profiles, Site U1438. Arrowed values = seawater data at ~6 m below sea surface.

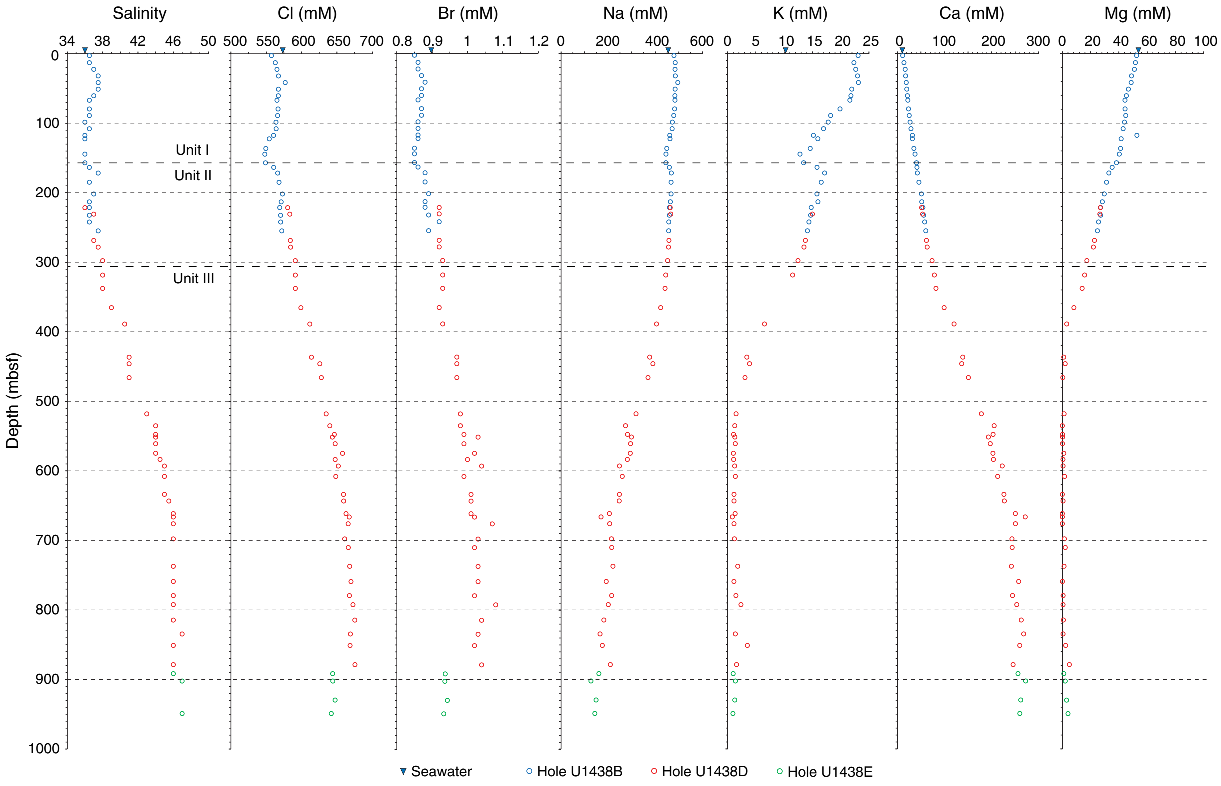

Boron, lithium, silica, manganese, barium, and strontium

Boron concentrations increase from 568.67 µM at ~3 mbsf (Core 351-U1438B-1H) to 635.47 µM at ~108 mbsf (Core 12H) and then decreased to 316.05 µM at the base of Hole U1438D (~879 mbsf) (Figure **F47**). Lithium concentrations increase from 21.54 µM at 3 mbsf (Core 351-U1438B-1H) to 32.29 µM at ~136 mbsf (Core 351-U1438B-15H), then decrease to 5.95 µM at ~792 mbsf (Core U1438D-62R) (Figure **F47**). Both Li and B concentrations increased at ~518 and ~737 mbsf (Cores 351-U1438D-33R and 56R), possibly as a result of remobilization and ion exchange in secondary minerals. Li concentrations increase significantly from Core 351-U1438D-66R to the bottom of Hole U1438D, occurring coincident with faulted beds (see **Core descriptions**). The major changes in Li and B concentrations occur independently of lithostratigraphic unit boundaries; however, both elements covary with pH (Figures **F45**, **F47**), suggesting that B and Li may be released in the upper sediment where pH is lower as a result of silicate dissolution and desorption of clay minerals, but retained in secondary minerals down hole where pH increased.

Silica concentrations vary significantly through Unit I (Figure **F47**) and can be generally correlated with the presence of volcanic ash layers (see **Core descriptions**), probably as a result of the dissolution of volcanic glass and silica phases concentrated in the ash layers. Si concentrations increase gradually to 255 mbsf (Core 351-U1438B-30X), possibly a zone of maximum silicate mineral dissolution, and then decrease through the remainder of Unit II and into Unit III to 851 mbsf (Core 351-U1438D-68R). Deeper than Core 68R, Si concentrations increase slightly and occur coincident with faulted beds (see **Core descriptions**). The downhole profile of manganese concentrations is similar to Si (Figure **F47**). Enhanced reduction of Mn oxides is indicated by the Mn concentration maximum near the base of Unit I.

The profile of barium resembles that of Ca, showing a downhole increase of ~900% (Figure **F47**), probably indicating that the alteration of volcaniclastic sediments and the basement released these cations into the IW. In addition, both Ba and Ca are present in sulfate minerals, the former in barite and the latter in gypsum and anhydrite. The presence of these minerals was confirmed by shipboard petrographic microscopy and XRD analysis (see **Core descriptions**). Preliminary pore water geochemical calculations indicate that barite was likely oversaturated throughout the sampled depths, whereas gypsum was oversaturated deeper than ~390 mbsf, corroborating the influence of these sulfate minerals on the patterns of Ca and Ba in the pore water.

Strontium concentrations increase from 90.63 µM at the surface (Core 351-U1438B-1H) to 138.50 µM at 269 mbsf (Core 351-U1438D-8R) (Figure **F47**). The steady increase of Sr with depth through Units I and II is most likely the result of low-temperature alteration of volcaniclastic sediment releasing Sr (Hawkesworth and Elderfield, 1978) and the recrystallization of calcium carbonate, as seen at ODP Site 1201 (Salisbury, Shinohara, Richter, et al., 2002). The highest Sr concentration occurs near the base of Unit II, consistent with an upper reaction zone of fresh volcaniclastic material (see **Core descriptions**). In Unit III, Sr concentrations decrease rapidly and reach a minimum of 18.94 µM at 698 mbsf.

Figure F47. Boron, lithium, silica, manganese, barium, and strontium depth profiles, Site U1438. Arrowed values = seawater data at ~6 m below sea surface.

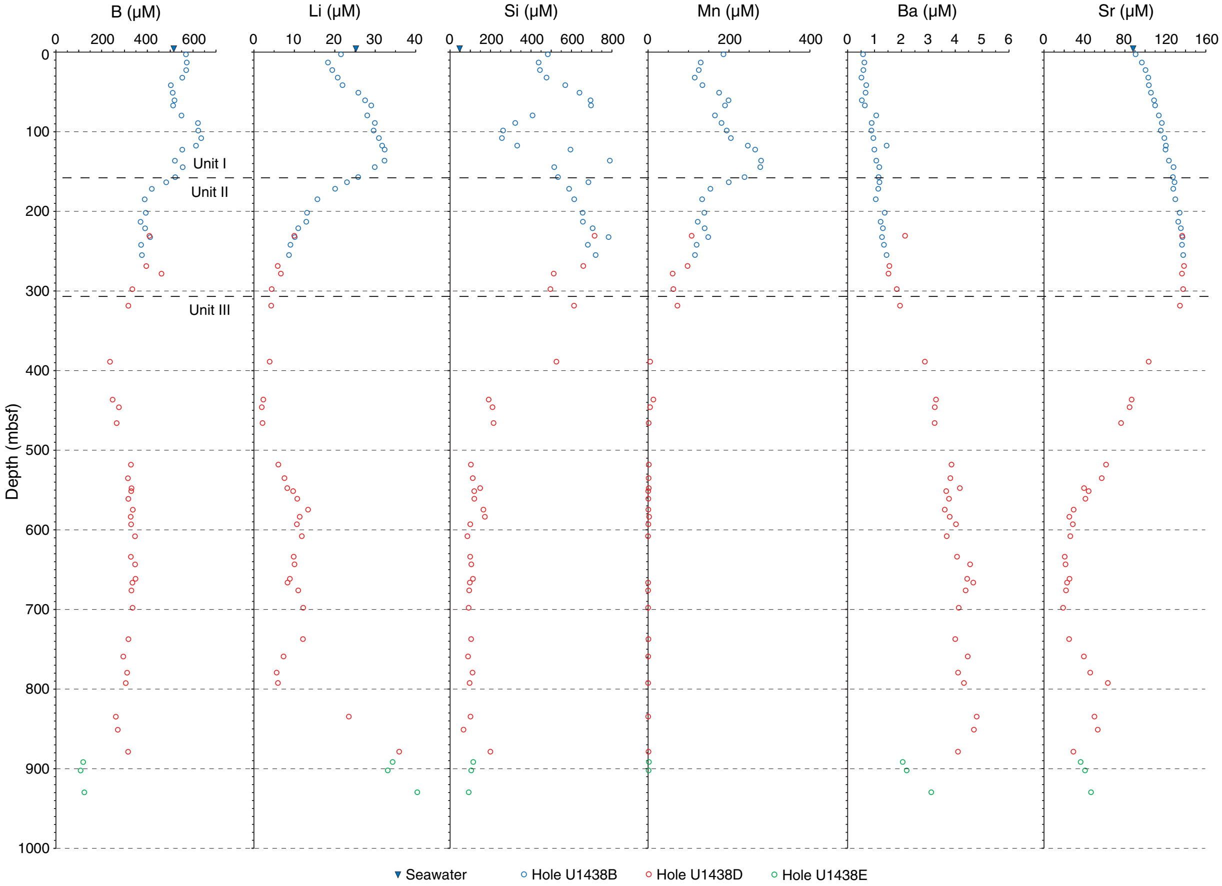

Crystalline precipitates in acidified IW samples

White and translucent crystalline needles were observed inside 15 vials of IW samples after acidification (see the **Expedition 351 methods** chapter [Arculus et al., 2015a]). The precipitates were photographed (Figure **F48**) and subsequently investigated under the petrographic microscope and by XRD. In addition, precipitates in three of the IW samples were filtered with a 0.45 µm (pore size) filter, and the remaining solution was analyzed by inductively coupled plasma–atomic emission spectroscopy (ICP-AES) and ion chromatography. The results show that the precipitates account for a loss of 18–21 mM of Ca (7.7%–8.9%), 6–8 mM of Na (2.6%–4.2%), 25–30 mM of Cl (3.8%–4.5%), and 3–6 mM of SO_4^{2-} (16.7%–28.7%). Petrographic microscopy of these crystals reveals relatively low birefringence, twinning, and extinction at 45°. The XRD pattern confirms the presence of gypsum. Although the ICP-AES data point to the formation of chloride minerals like $CaCl_2$ or NaCl, these were not observed in the XRD, probably because these precipitates were subject to possible dissolution in deionized water, which was used to spread the sample across the holder for the XRD analysis.

Solid phase analyses

Headspace gas

Samples were taken from 160 sediment cores from Units I–IV at Site U1438 for headspace gas analyses. No samples were taken from Unit 1 (basement). Methane concentrations range from 1.12 to 9.1 ppmv with an average of 2.35 ppmv (Figure **F49**), indicating a background level. Ethane was detected in four cores, with a maximum concentration of 2.03 ppmv. No propane or longer chain hydrocarbons were detected in any Site U1438 cores.

Carbonate, total organic carbon, and total nitrogen

Carbonate content in the solid phase is generally low in Unit I, typically <0.5 wt% (Figure **F49**). Two foraminiferal oozes from 7.8–8.3 mbsf (Sections 351-U1438B-2H-1 and 2H-2) and ~12.5 mbsf (Section 2H-5) are characterized by very high $CaCO_3$ contents, 28.7 wt% (n = 3) and 59.7 wt% (n = 1), respectively. Unit II is distinct from Unit I with a higher average (12.2 wt%) and variation between 0.1 and 37.6 wt% $CaCO_3$. For the upper part of Unit III (309.6–666.5 mbsf), the carbonate content varies between 0.2 and 14.3 wt% (average = 4.2 wt%), whereas from 666.5 mbsf (Section 351-U1438D-49R-1) to 949 mbsf (Section 351-U1438E-12R-3), it is less than 1 wt%. One exception is a sample at the base of Unit III (Section 351-U1438E-52R-3) that contains 10.5 wt% $CaCO_3$. No samples were analyzed for carbonate content between 950 and 1332 mbsf. The average carbonate content of Unit IV was ~1 wt%, with a maximum of 3.4 wt% in Section 351-U1438E-66R-CC.

Total organic carbon (TOC) decreases rapidly from 0.22 wt% at the top of Unit I (Section 351-U1438B-1H-1; 2.9 mbsf) to 0.04 wt% at the bottom (Section 17H-1; 157.05 mbsf) but abruptly rises to 0.51 wt% at the top of Unit II (Section 20F-2; 171.75 mbsf) and remains relatively high in the rest of Unit II (0–0.25 wt%) (Figure **F49**). The TOC of Unit III exceeds 0.1 wt% on only four occasions. From 535.4 mbsf to Unit IV, TOC values were all <0.1 wt%.

Total nitrogen content decreases from 0.05 wt% at the top of Unit I (Section 351-U1438B-1H-1; 2.9 mbsf) to 0.01 wt% at the bottom (Section 17H-1; 157.05 mbsf) and is 0 wt% in Units II–IV (Figure **F49**).

Sediment geochemistry

A total of 27 sedimentary samples were chosen for ICP-AES analysis. Ten were selected from the squeeze cake sections to compare solid-phase chemical compositions with IW compositions, and the remaining 17 samples were selected at ~50 m intervals downhole. Downhole profiles for major elements are shown in Figure **F50**, and bulk chemical compositions are reported in Table **T15**. Loss on ignition (LOI) for sediment samples ranges from 3.91 to 14.47 wt%. The highest LOI values are from unconsolidated sediments in Unit II. During sample preparation (see the **Expedition 351 methods** chapter [Arculus et al., 2015a]), no undissolved macroscopic residue was observed after nitric acid digestion. In order to avoid microscopic undigested residue from the rock samples entering the ICP-AES, samples were filtered with a 0.45 µm filter.

Figure F48. A. Crystalline precipitates in IW samples acidified for ICP-AES analysis. B. Photomicrograph (XPL). C. XRD pattern in red with predicted peak locations for gypsum in blue. WL = wavelength.

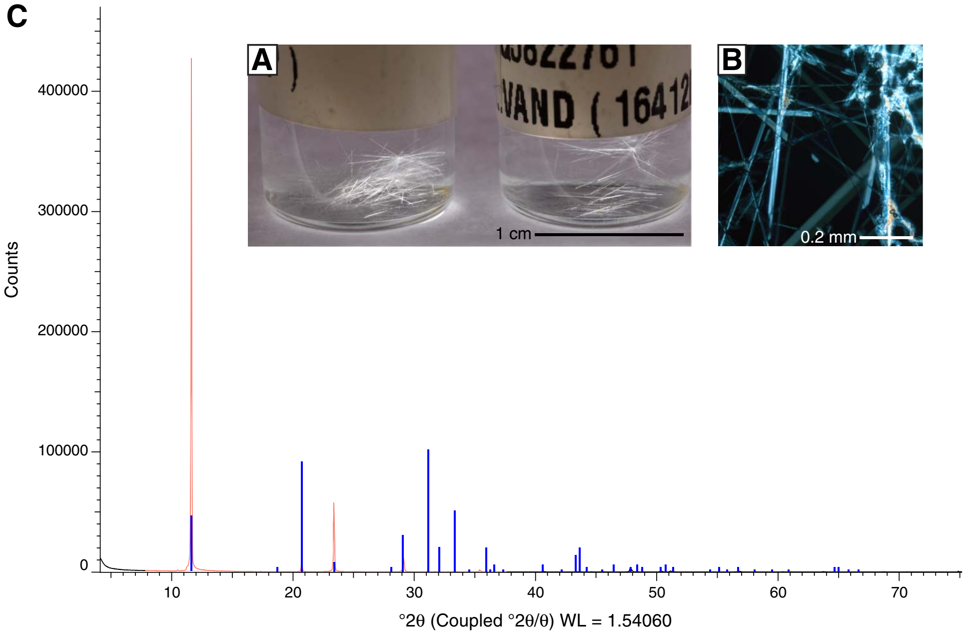

Figure F49. Methane, calcium carbonate, TOC, and TN depth profiles, Site U1438.

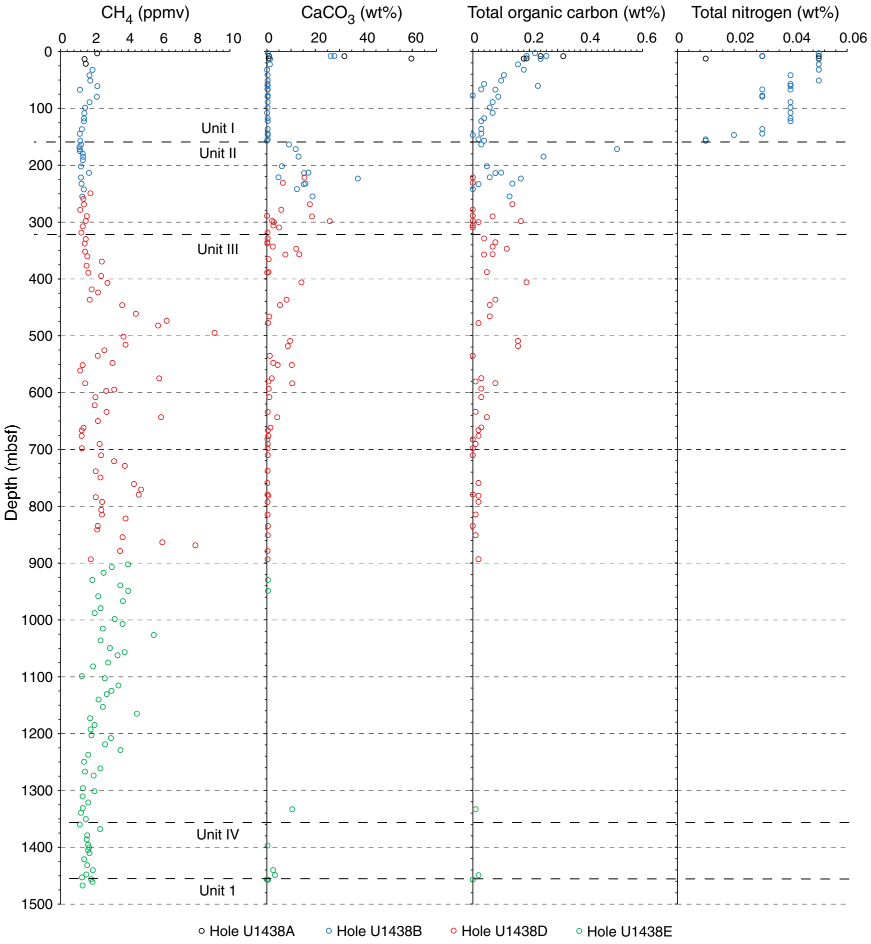

Figure F50. Sediment major element depth profiles, Site U1438.

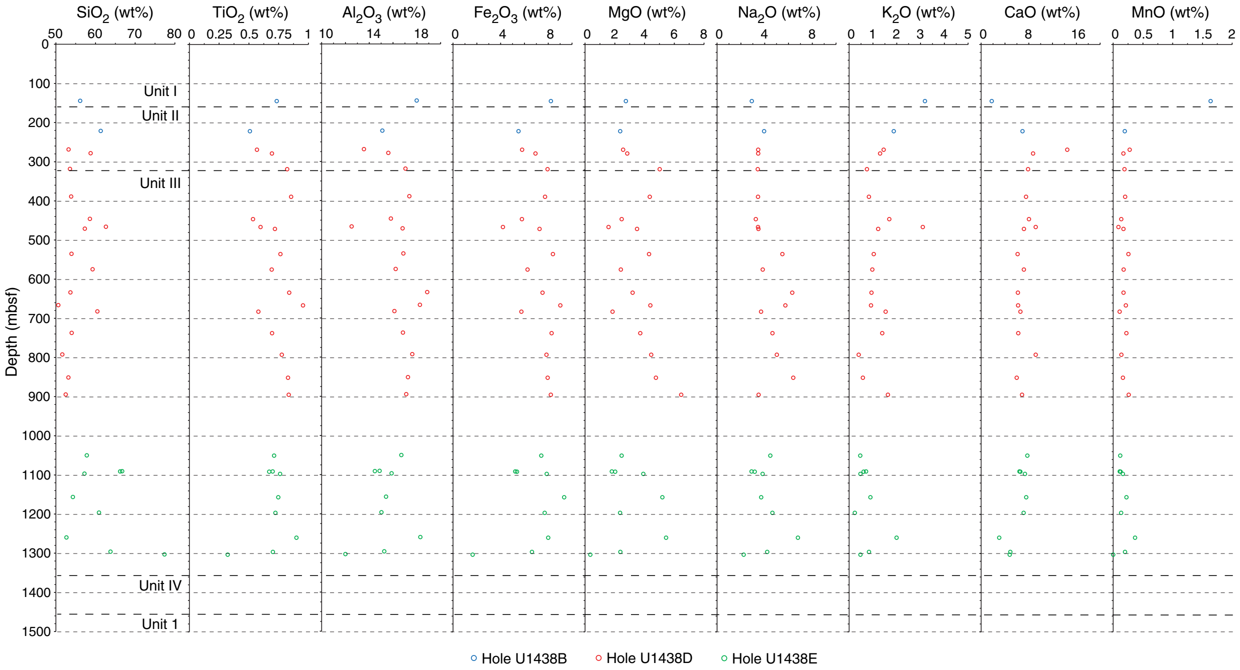

Table T15. Sediment and hard rock bulk chemistry: SiO_2, Al_2O_3, TiO_2, $Fe_2O_3{}^t$, MgO, K_2O, CaO, MnO, Na_2O, LOI, Ba, Cr, Sc, Sr, V, Y, and Zr. **Download table in .csv format.**

Figure F51. Si/Mg and Al_2O_3 depth profiles for sediments and sills, Site U1438. Solid line represents relative grain size distribution (see **Core descriptions**).

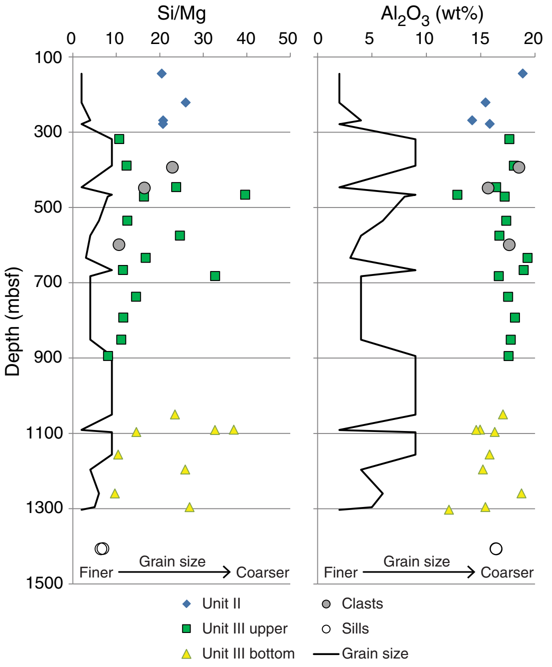

In Unit III, CaO decreases in the sediments from 9.17 wt% at ~466 mbsf (Core 351-U1438D-28R) to 3.04 wt% at ~1260 mbsf (Core 351-U1438E-44R), varying inversely with the increase of Ca in the IW (Figure **F50**). Concentrations of SiO_2 range from ~53 to ~78 wt%. Downhole variations in Si/Mg ratios are roughly correlated with changes in grain size (Figure **F51**). Maxima in Si/Mg ratios occur near conglomerate intervals, presumably from increased abundances of volcanic-derived detritus (see **Core descriptions**). The observed Si/Mg maxima near these zones suggest that the source of volcaniclastic sediment during these intervals was probably andesitic to rhyolitic/dacitic in composition. Al_2O_3 also correlates with grain size distribution downhole. In the conglomerate intervals, decreases in Al_2O_3 content are observed (Figure **F51**).

Igneous geochemistry

Thirty-seven samples from the lava flows of Unit 1 were collected in Cores 351-U1438E-70R through 88R and analyzed for major and trace elements by ICP-AES (Table **T15**). LOI for the basement samples ranges between 0.80 and 5.80 wt%. One outlier, altered Sample 351-U1438E-83R-2, has an LOI of 11.23 wt% and contains 77.84 wt% SiO_2 and only 3.75 wt% Fe_2O_3. The majority of the lava flow samples are high-MgO (mostly >8 wt%), low-TiO_2 (0.6–1.1 wt%), low-Zr (mostly <50 ppm), high-Sc (mostly >40 ppm), and high-Cr (up to ~400 ppm) tholeiitic basalts. They are compositionally very similar to the ~49 Ma basalts recovered from ODP Leg 195 Hole 1201D in the West Philippine Basin (Savov et al., 2005) and the ~52 Ma fore-arc basalts recovered from the present-day Izu-Bonin Trench wall (Reagan et al., 2010; Ishizuka et al., 2011) (Figure **F52**). Compared with global mid-ocean-ridge basalt compositions (Jenner and O'Neill, 2012), Hole U1438E basalts have high MgO/FeO with markedly low TiO_2, low Zr, and high Sc abundances; they are relatively primitive melts and likely derived from strongly depleted upper mantle sources, as indicated by very low Zr/Y ratios. Igneous rocks sampled in Unit IV above the basement in Cores 351-U1438-61R and 62R are Na-rich basaltic andesite.

Figure F52. Y vs. Zr for samples from a compilation of global mid-ocean-ridge basalts (Jenner and O'Neill, 2012), Site 1201 (Savov et al., 2005), fore-arc basalts (FAB) from the Mariana fore arc (Reagan et al., 2010), and Unit 1, Site U1438.

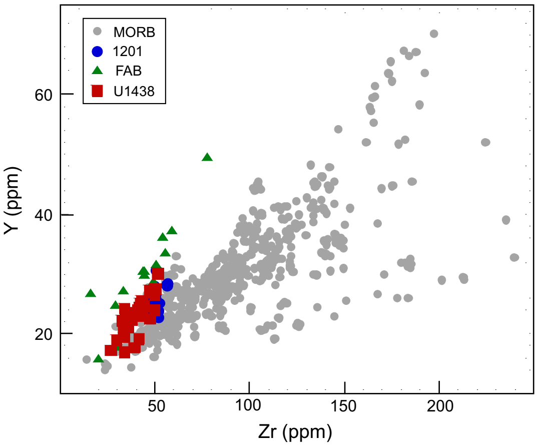

Paleomagnetism

Archive-half core remanence data

Remanence measurements were made at 2 cm intervals on all archive-half APC cores in Holes U1438A and U1438B, on archive-half XCB core pieces in Hole U1438B, and on archive-half RCB core pieces longer than approximately 10 cm in Holes U1438D and U1438E. All archive-half samples were subjected to stepwise alternating field (AF) demagnetization at 25, 35, and 40 mT, following experiments on pilot sections that were demagnetized in 5 mT steps up to 40 mT. These experiments showed that the ubiquitous drilling-induced magnetic overprint could be largely removed by treatment at 25 mT, allowing the paleomagnetic polarity of most core sections to be determined. Additional measurements after treatment at 35 and 40 mT were conducted, however, to allow the reliability of data to be checked. Demagnetization in AFs > 40 mT was not attempted because of a well-documented problem with the superconducting rock magnetometer (SRM) demagnetization coils that has been a characteristic problem of the SRM system observed during several IODP expeditions (e.g., see Teagle, Ildefonse, Blum, and the Expedition 335 Scientists, 2012), which results in acquisition of spurious, laboratory-imparted anhysteretic remanent magnetizations (ARMs) along the *z*-axis of the SRM system at higher applied fields.

Remanence data were filtered to discard data obtained within 4.5 cm of section or piece ends, and archive-half core point magnetic susceptibility (Section Half Multisensor Logger [SHMSL]) data were filtered to preserve only data corresponding to the intervals where remanence measurements were made. In general, the quality of magnetic data from APC-recovered intervals is much higher than for data from half-APC and XCB cores. The latter are frequently disturbed by "biscuiting," characterized by intervals of coherent or relatively undisturbed rotated core segments a few to tens of centimeters long separated by highly disturbed intervals as thick as several centimeters. Hence, magnetization directions and intensity are substantially less noisy and more coherent in APC-recovered intervals. Some interpretable demagnetization data were obtained from XCB Core 351-U1438B-23X, but remaining XCB cores in this hole were too disturbed by biscuiting to yield usable remanence data. RCB cores in Holes U1438D and U1438E consist of unoriented pieces of variable length, and the majority of core sections contained pieces of sufficient length to allow remanence measurements. However, data from RCB cores have a more pervasive drilling-induced magnetic overprint, which was difficult to remove adequately by demagnetization to 40 mT, especially in samples from Hole U1438E.

For the purpose of characterization based on bulk magnetic parameters, the lithologies recovered from Site U1438 are grouped into lithostratigraphic units defined by the core description team. Unit I, which includes all of Hole U1438A and the top of Hole U1438B to 160.3 mbsf (Section 351-U1438B-18H-1, 110 cm), dominantly consists of tuffaceous mud, mud with ash, mud, clay, and ash. Unit II, which includes Hole U1438B deeper than 160.3 mbsf and Hole U1438D to 309.6 mbsf, dominantly consists of tuffaceous siltstones, mudstones, and sandstones. Unit III, which includes Hole U1438D deeper than 309.6 mbsf and Hole U1438E to 1361.4 mbsf, dominantly consists of tuffaceous mudstones, siltstones, sandstones, and breccia-conglomerates. Unit IV, which includes Hole U1438E between 1361.4 and 1461.1 mbsf, dominantly consists of mudstones, sandstones, tuffaceous mudstones, tuffaceous siltstones, and tuffaceous sandstones. Unit 1, at the base of Hole U1438E from 1461.1 to 1611.1 mbsf, consists of basaltic rocks representing the basement to the overlying sedimentary succession. The variations in low-field magnetic susceptibility and the intensity of natural remanent magnetization (NRM) through these units are illustrated in Figures **F53** and **F54**, respectively. The frequency distributions of these parameters in each unit are illustrated in the histograms of Figure **F55**. Susceptibility increases in maximum values in successive units downhole, with the finer grained lithologies of Unit I having susceptibilities two orders of magnitude lower than the basement rocks of Unit 1. NRM intensities are variable in the sedimentary rocks, reaching maximum values of approximately 1 A/m but with peak values of 7 A/m in Unit II (potentially representing ash layers in the succession). These variations probably reflect higher concentrations of multidomain magnetite grains in the coarser clastic sediments. Basaltic basement rocks of Unit 1 have maximum NRM intensities in excess of 10 A/m, suggesting these rocks may represent a source for marine magnetic anomalies (see below). Figure **F56** shows biplots of NRM intensity against susceptibility for all units. Both parameters are dependent on the concentration of magnetic minerals (dominantly magnetite) in samples, and linear trends in such plots indicate a constancy of magnetic mineralogy and ferromagnetic grain size. Such trends are evident in Units I, III, and IV. However, differences in the fields occupied by each unit suggest that there may be contributions to the sedimentary units from sources with different rock magnetic properties. These differences may be resolved using a wider range of magnetic param-

Figure F53. Downhole variations in low-field MS in archive-half cores measured with the SHMSL, Site U1438.

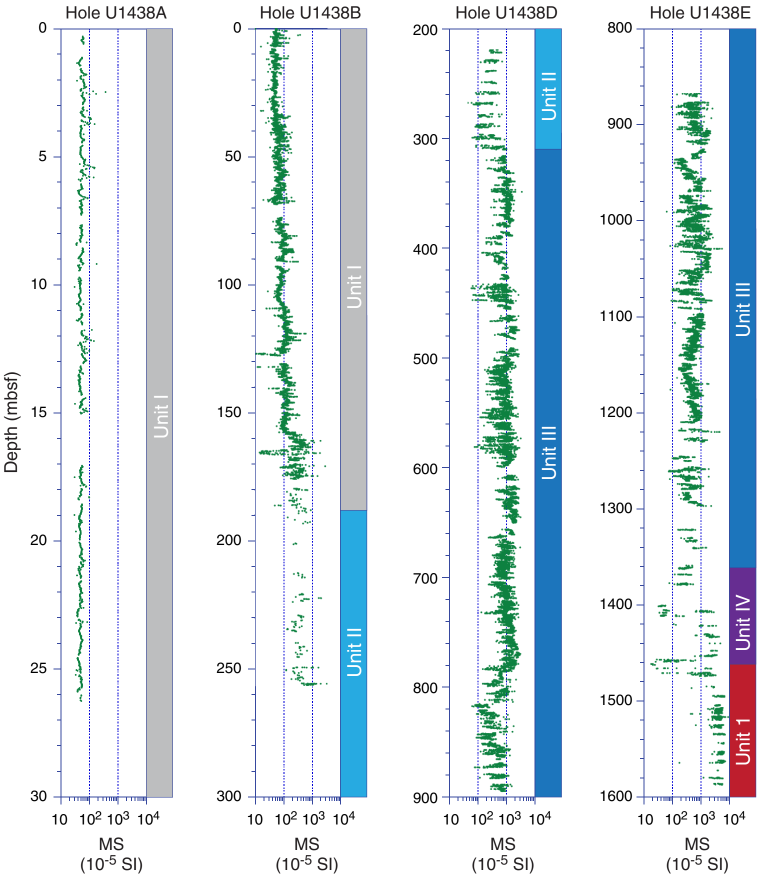

Figure F54. Downhole variations in NRM intensity in archive-half cores measured with the SRM, Site U1438.

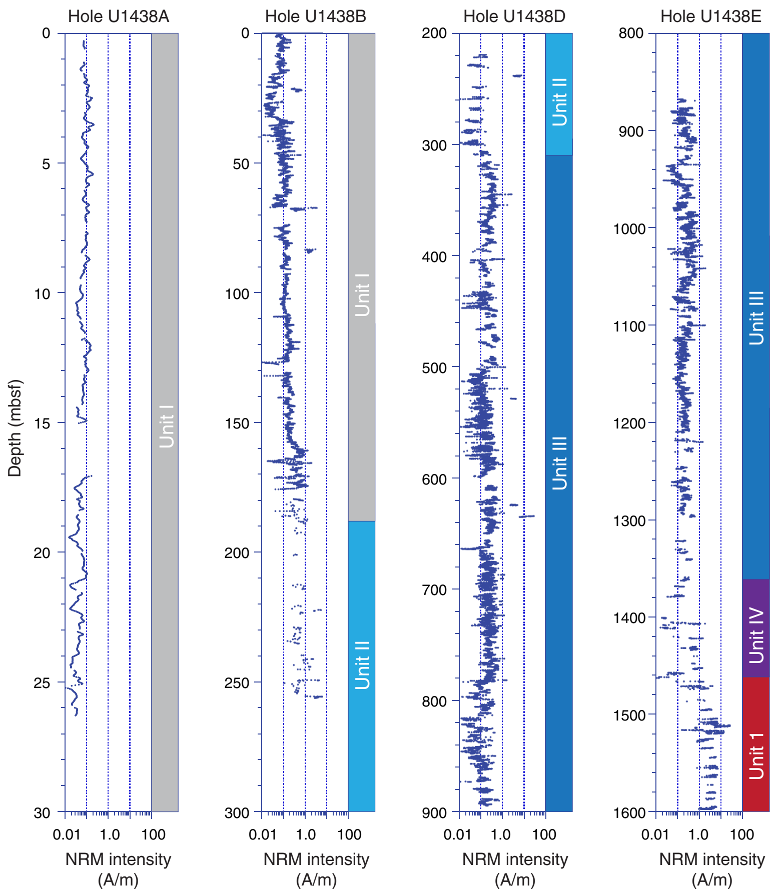

Figure F55. Low-field magnetic susceptibility and NRM intensity by lithostratigraphic unit based on archive-half core SHMSL and SRM measurements, Site U1438.

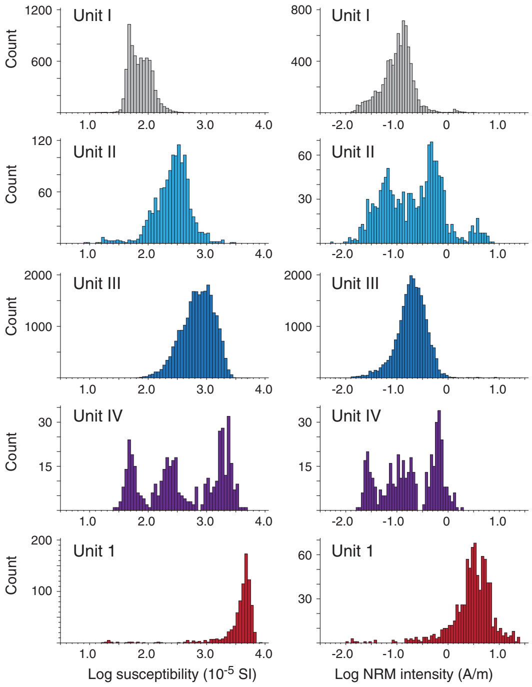

Figure F56. NRM Intensity vs. low-field magnetic susceptibility, Site U1438. Variations parallel to the dashed lines reflect variations in the concentration of magnetic phases.

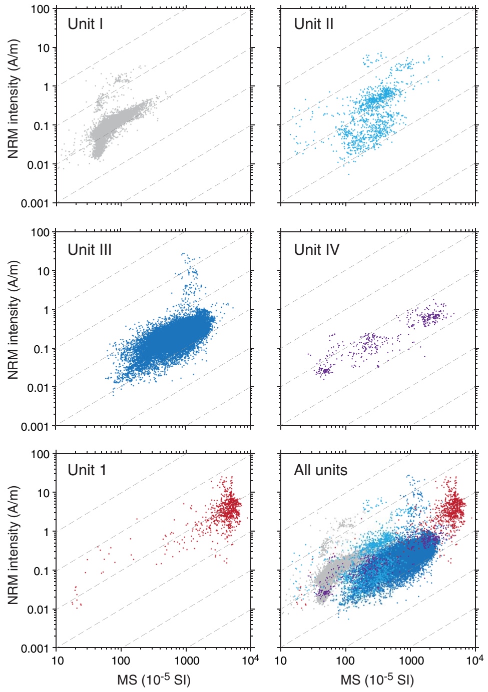

eters and by employing environmental magnetic principles (Thompson and Oldfield, 1986) to perform unmixing of different magnetic fractions in these sediments.

Despite using nonmagnetic core barrels and cutting shoes during collection of cores, NRM directions in both holes are dominated by a pervasive, steeply inclined, drilling-induced magnetic overprint (Figure **F57**), as documented during numerous ODP and IODP legs/expeditions (Acton et al., 2002). Samples with the highest magnetic susceptibilities ubiquitously have NRM inclinations that are steep and positive as a result of this drilling-induced component, and only samples with susceptibilities less than 1500 × 10^{-5} SI record NRMs with negative inclinations (Figure **F58**), suggesting that the overprint resides predominantly in coarse, multidomain magnetite. This spurious magnetization is largely removed by low AF treatments in archive-half section samples. For example, treatment at 25 mT results in a more bimodal distribution of remanence inclinations (reflecting the presence of normal and reversed polarity natural magnetizations). However, the drilling-induced overprint can persist to higher demagnetization levels, potentially biasing normal and reversed polarity magnetizations to steeper and shallower inclinations, respectively, and in some cases making determination of polarity difficult.

Figures **F59**, **F60**, and **F61** show representative examples of AF demagnetization behavior in archive-half core samples where components that are not related to drilling have been successfully isolated. The majority of samples have an initially downward-directed remanence due to the drilling-induced component, most of which is removed by AF treatment at 20–25 mT. This is followed by removal of a moderately inclined, either downward- or upward-directed component that decays toward the origin (up to the maximum applied field of 40 mT) on orthogonal vector plots that represent the characteristic remanent magnetization (ChRM). However, demagnetization paths are also frequently observed that do not trend toward the origin by AF treatment up to 40 mT, following removal of the steep drilling-induced component (Figures **F62**, **F63**, **F64**). In some of these examples, the polarity of the ChRM component is readily determined, allowing the SRM data to be used with confidence for magnetostratigraphic purposes. In other cases, successive

Figure F57. NRM directions in Units I, II, and 1, Site U1438. Top: individual determinations. Bottom: same data represented by Kamb contours. All units show dominance of steep downward directions resulting from a pervasive drilling-induced magnetic overprint. Unit II sediments and Unit 1 basalts also show a preferred clustering of NRM directions biased toward the core *x*-axis, resulting from the radial component of the drilling-induced magnetization (Acton et al., 2002). Produced using Rick Allendinger's Stereonet program v. 8.9.6 (Cardozo and Allmendinger, 2013).

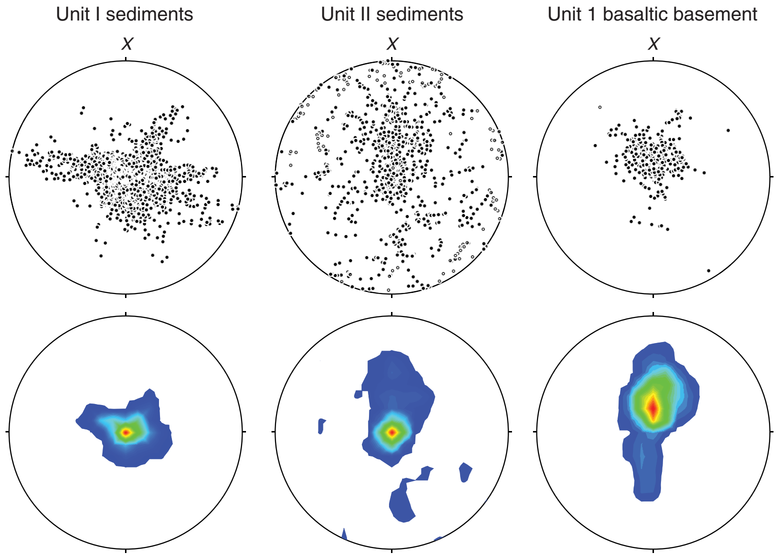

Figure F58. Variation in (left) NRM inclination and (right) inclination after AF demagnetization to 25 mT with low-field magnetic susceptibility for Units I–III, Site U1438.

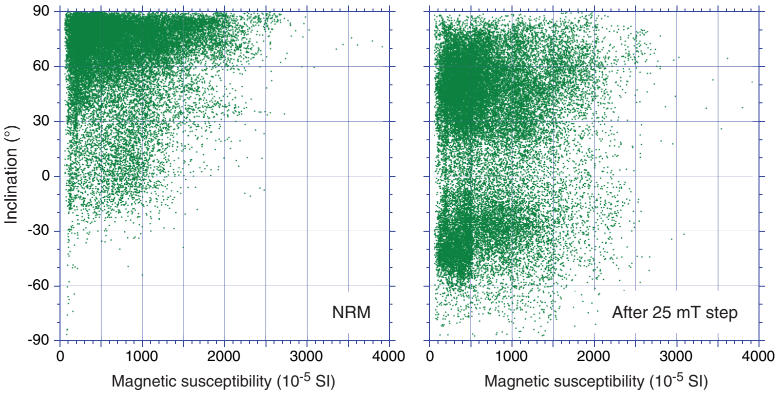

Figure F59. Examples of AF demagnetization of Unit I archive-half core sections, Hole U1438A. For Figures F59 through F64: solid circles = projection onto the horizontal plane, open circles = projection onto either the vertical X–Z or Y–Z planes.

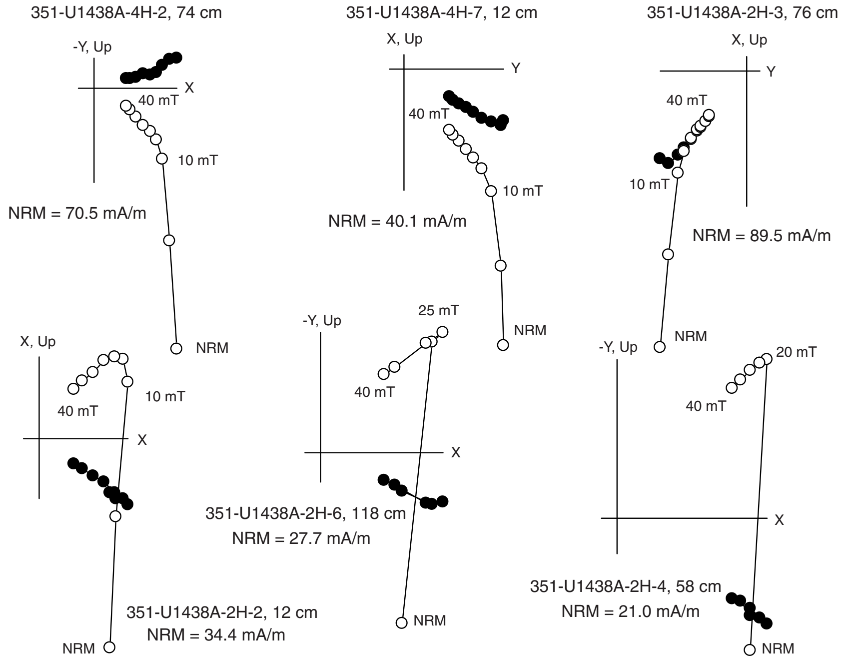

Figure F60. Examples of AF demagnetization of archive-half core sections showing clear ChRM components following removal of the steeply inclined drilling-induced overprint, Hole U1438B.

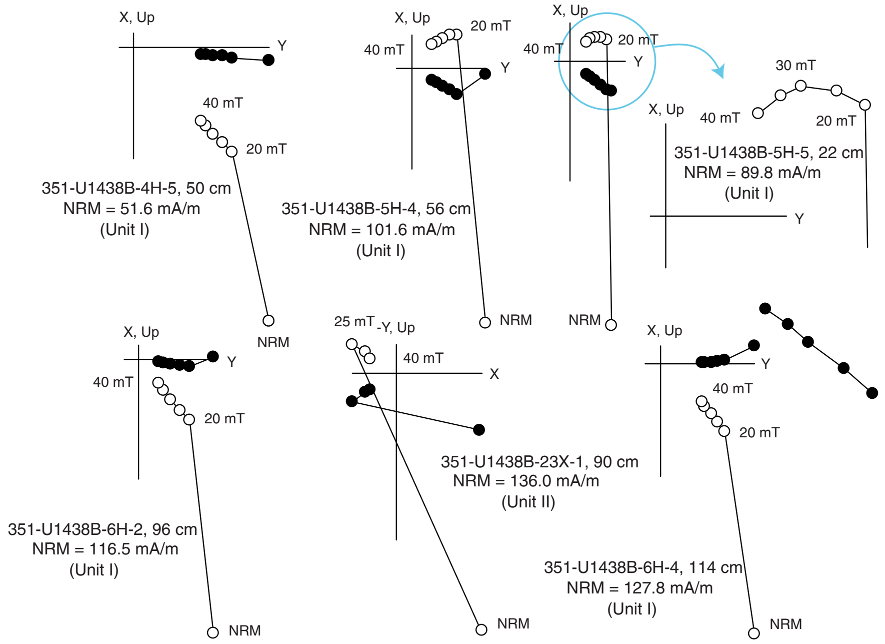

AF treatment steps define linear components that have positive inclinations but that pass onto the upper hemisphere, requiring a more subjective decision regarding polarity. In some rarer instances, demagnetization paths still trend away from the origin at the highest applied field, making determination of ChRM inclination impossible. Finally, in Unit IV (Hole U1438E), AF demagnetization was effective at removing the drilling-induced overprint but in some cases failed to demagnetize the natural remanence as a result of the presence of hematite-hosted remanences with high coercivities, requiring thermal demagnetization to isolate ChRMs. Shore-based rock magnetic experiments on discrete samples are required in order to fully understand this variability, but we note that polarity was determined unambiguously for the majority of SRM determinations conducted on samples from Holes U1438A, U1438B, and U1438D. Samples from Hole U1438E, however, have ubiquitously steep magnetizations after treatment at the maximum applied field

Figure F61. Examples of AF demagnetization of archive-half core sections showing clear ChRM components following removal of the steeply inclined drilling-induced overprint, Hole U1438D.

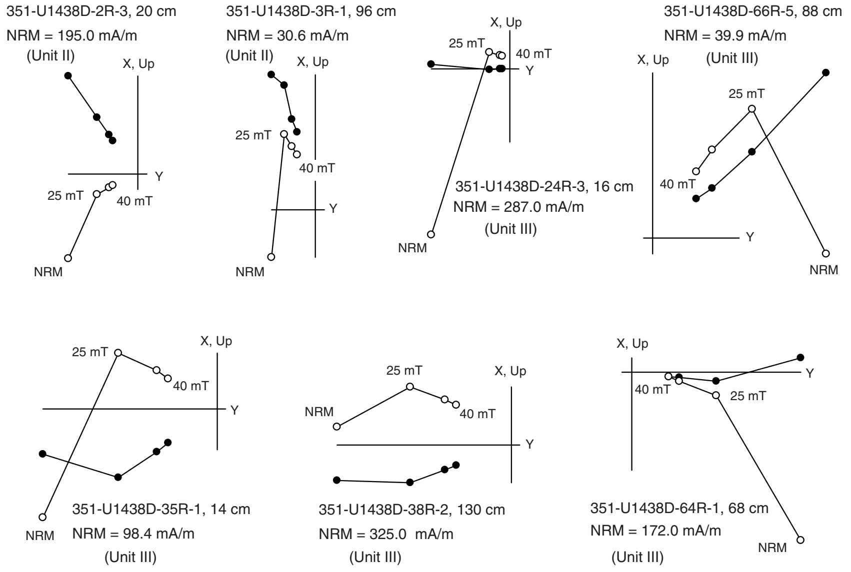

Figure F62. Examples of AF demagnetization of archive-half core sections showing clear reversed polarity magnetizations (following removal of the steeply inclined drilling-induced overprint) that do not reach stable endpoint directions, Hole U1438B.

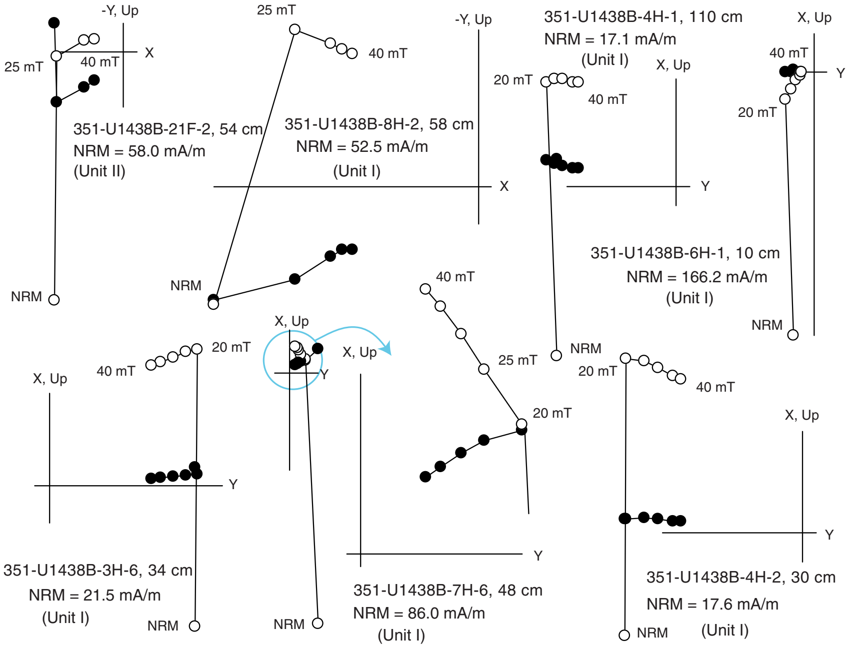

of 40 mT. It is likely that this hole is dominated by normal polarity magnetizations, but shore-based analysis of discrete samples (using higher AFs or thermal demagnetization) is required to identify any magnetozones present deeper than 850 mbsf.

The FlexIT core orientation tool was used with all full-stroke APC deployments in Hole U1438B (0–168.88 mbsf). The orientation tool uses three orthogonally mounted fluxgate magnetometers to record the orientation of the double lines scribed on the core liner with respect to magnetic north, providing an angular correction from core to geographic reference frameworks for each deployment that allows recovery of magnetic declination data. Figure **F65** shows the result of applying these corrections to the 25 mT treatment level data. Compared to the uncorrected data, magnetization directions clearly separate into two broadly north–south oriented polarity groups upon FlexIT correction. These groups are more clearly discernable in Kamb-contoured equal area stereographic projections (Figure **F66**). Considerable scatter in the distribution of individual remanence determinations exists in this data set, but this is comparable to that expected from paleosecular variation (PSV) of the geomagnetic field. Statistical field models allow prediction of the variability of field directions due to PSV. Figure **F66** shows a modeled distribution at the latitude of Site U1438, calculated using

Figure F63. Examples of AF demagnetization of archive-half core sections showing clear reversed polarity magnetizations (following removal of the steeply inclined drilling-induced overprint) that do not reach stable endpoint directions, Hole U1438D.

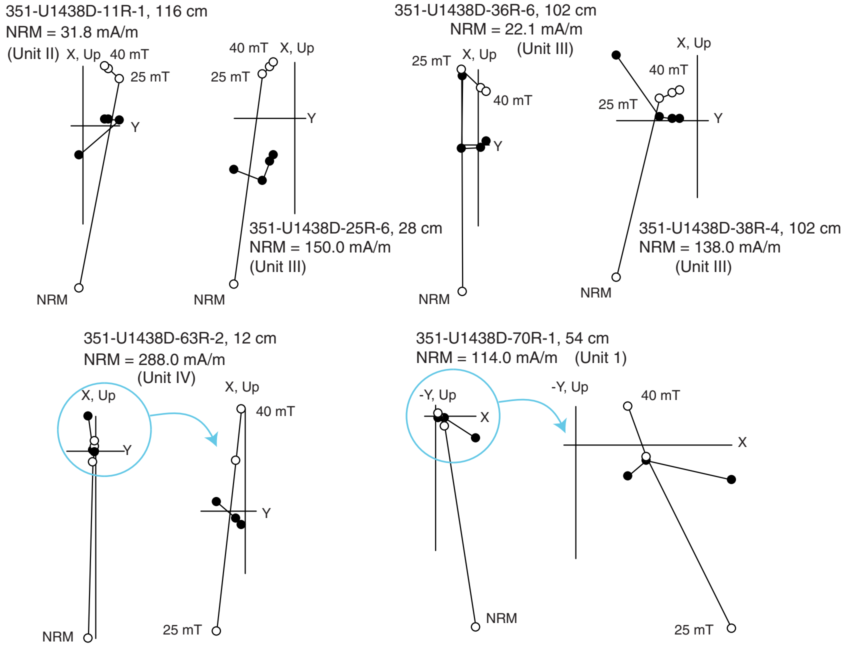

Figure F64. Examples of AF demagnetization of archive-half core sections showing dominance of steeply inclined drilling-induced overprints and evidence for hematite-hosted remanences in some samples, Hole U1438E.

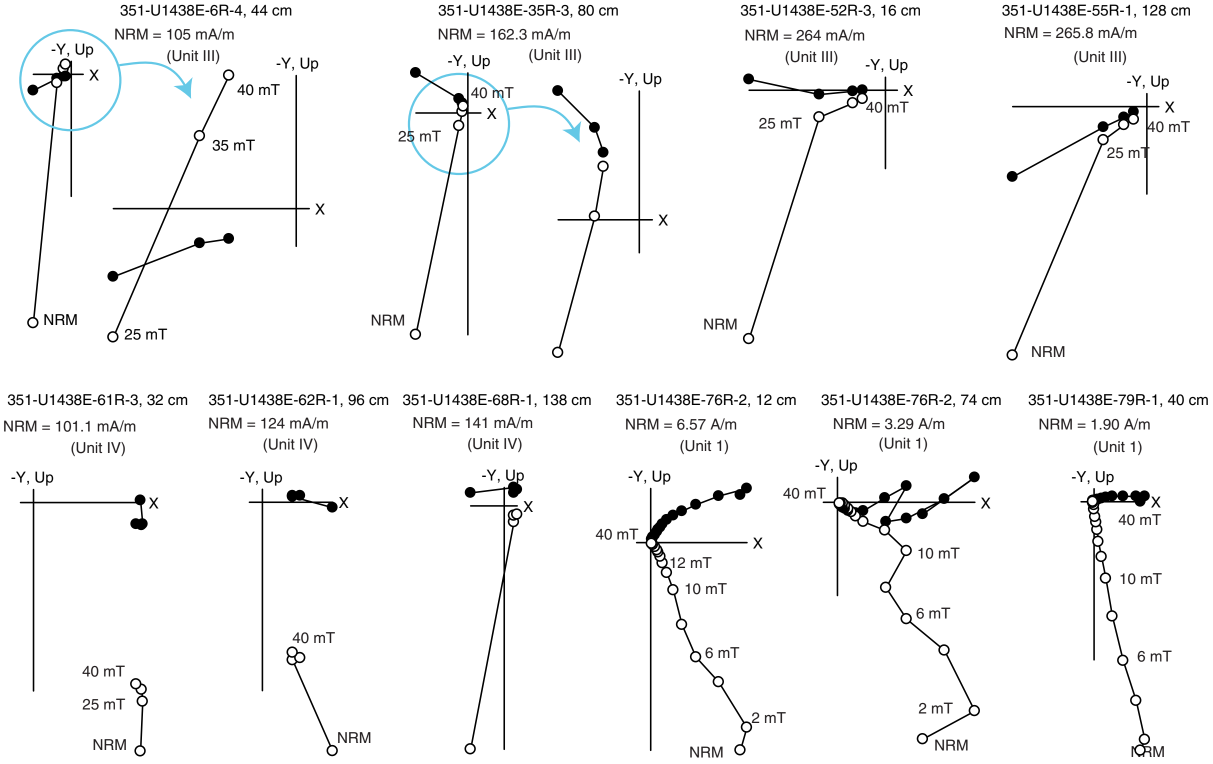

the statistical field model TK03.GAD of Tauxe and Kent (2004) from 6853 realizations (equivalent to the number of FlexIT reoriented remanence determinations in Hole U1438B). Comparison with the distribution of observed remanence directions indicates that PSV is adequately sampled in the reoriented data set from Hole U1438B. Moreover, the downhole distribution of FlexIT-corrected remanences (Figure **F67**) shows ~180° alternations of declination, and these values cluster at ~0° and ~180°, providing important additional constraints that inform the identification of geomagnetic reversal boundaries and magnetozones to ~170 mbsf.

Figure F65. Archive-half core section magnetizations after AF demagnetization in a 25 mT applied field, Hole U1438B. Top: data in core reference frame. Bottom: data in geographic reference frame, following application of azimuthal corrections provided by the FlexIT tool. Produced using Rick Allendinger's Stereonet program v. 8.9.6 (Cardozo and Allmendinger, 2013).

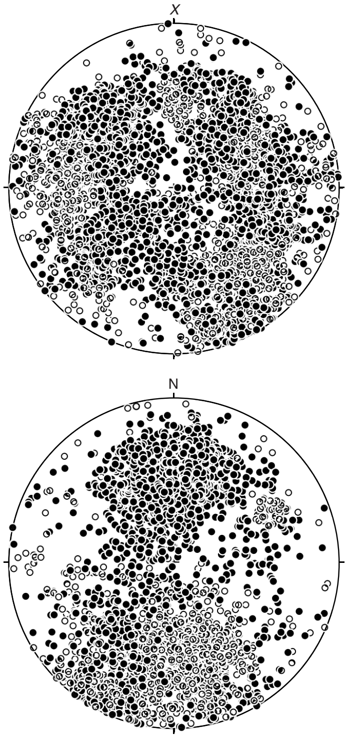

Figure F66. Top: Kamb-contoured archive-half core section magnetizations after AF demagnetization at 25 mT (6853 measurement points), showing recovery of antipodal polarity groups after application of FlexIT corrections, Hole U1438B. Bottom: instantaneous geomagnetic field directions calculated from 6853 realizations of the statistical field model TK03.GAD of Tauxe and Kent (2004) for the location of Site U1438. The distribution of these vectors predicts the variability of geomagnetic field directions at the site due to paleosecular variation (PSV). Produced using Rick Allendinger's Stereonet program v. 8.9.6 (Cardozo and Allmendinger, 2013).

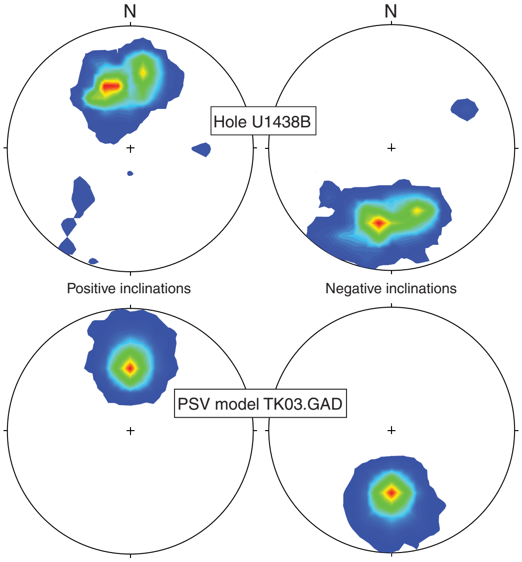

Figure F67. Remanence inclinations and declinations, Hole U1438B. Red dashed lines = axial geocentric dipole inclination expected at this site. Declinations have been recovered using azimuthal corrections supplied by the FlexIT tool. Note the clear pattern of geomagnetic field reversals marked by switches in both inclination and declination across reversal boundaries.

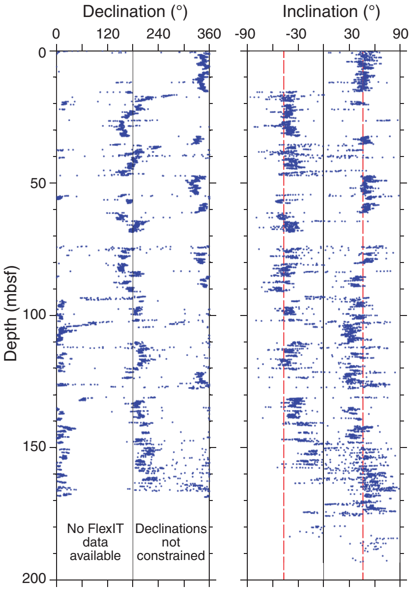

Discrete sample remanence data

A total of 190 discrete samples were demagnetized during Expedition 351 (47 by AF treatment and 143 using thermal demagnetization), mainly to check the reliability of archive-half core data from the SRM system. Representative examples are shown in Figures **F68** and **F69**. In most cases, these examples demonstrate removal of the drilling-induced overprint by applied fields of 10–20 mT or temperatures of ~200°C, leaving a linear ChRM that decays toward the origin by peak applied fields of 80 mT or temperatures of 580°C. These data are consistent with remanence being carried by magnetite. Samples from red mudstones and siltstones from Unit IV in Hole U1438E required thermal treatment to 630°–660°C to fully demagnetize the natural remanence (after removal of the drilling-induced overprint by temperatures of ~200°C), consistent with remanence carried by hematite. The high-quality data obtained from the shipboard discrete samples are insufficient in quantity to define magnetostratigraphic intervals but indicate that shore-based demagnetization of a larger suite of discrete samples will yield reliable remanence directions that may be used for both magnetostratigraphic and tectonic purposes.

Anisotropy of low-field magnetic susceptibility (AMS) was determined from a subset of discrete samples with AMS signals sufficiently high to allow measurement on ship using the AGICO Kappabridge KLY4 system. Results for fine-grained sedimentary rocks of Units III and IV and basaltic basement rocks of Unit 1 (Hole U1438E) are shown in Figure **F70**. Sedimentary samples have oblate fabrics that define a typical depositional fabric, with k_3 (minimum) principal axes oriented normal to bedding. k_1 (maximum) principal axes are distributed in the horizontal plane, but without reorientation parameters for these samples, it is impossible to determine whether there is a preferred magnetic lineation in these rocks. Basaltic rocks display k_1 principal axes that are generally shallowly plunging with steeply plunging k_3 principal axes, suggesting that a planar magnetic fabric is also present in these rocks. This

Figure F68. Examples of AF and thermal demagnetization of discrete samples, Holes U1438B and U1438D. For Figures F68 and F69: Solid circles = projection onto the horizontal plane, open circles = projection onto the vertical X–Z plane.

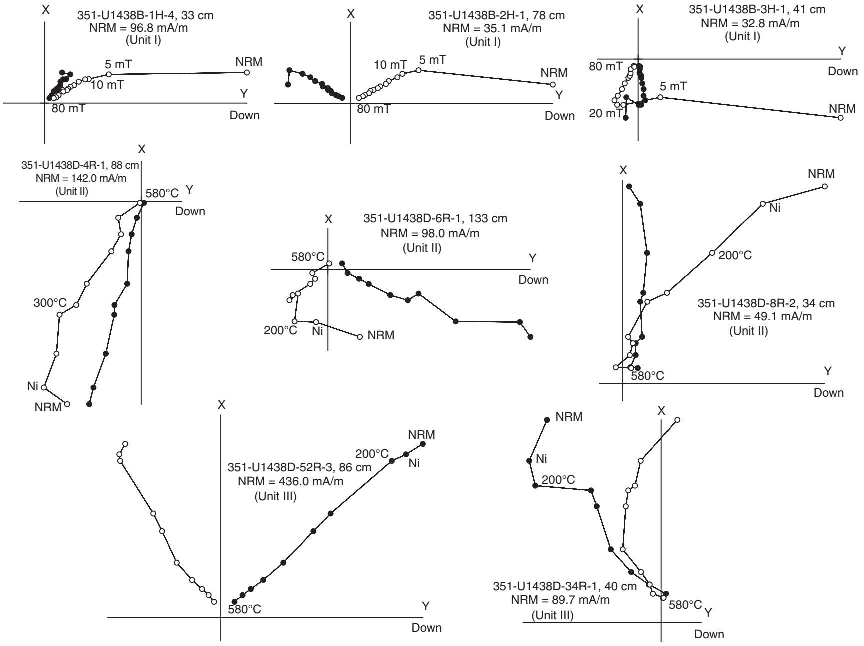

Figure F69. Examples of thermal demagnetization of discrete samples, Holes U1438D and U1438E.

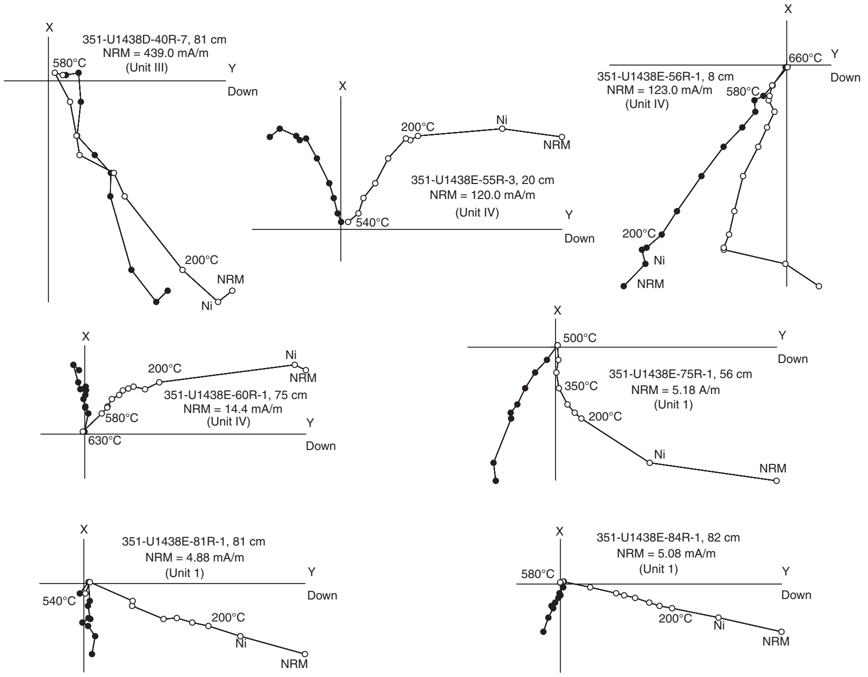

supports the interpretation that these rocks represent extrusive flows.

Magnetostratigraphy

After examining downhole plots of single demagnetization step inclination data from Holes U1438A and U1438B, data from the 25 mT treatment were used as the primary observations in determining magnetostratigraphy. However, inspection of orthogonal vector plots of the full demagnetization data at each measurement point confirmed polarity in intervals where the 25 mT step data were not clear cut. For Holes U1438D and U1438E, data from individual demagnetization steps did not allow unambiguous identification of patterns of magnetozones. A robust interpretation for Hole U1438D was made possible by using a combination of: (1) principal component analysis (PCA) of data from individual measurement points (filtered to exclude PCA picks with maximum angular deviations >10°), (2) averaging of PCA directions within individual RCB core pieces, and (3) filtering of anomalous PCA directions by com-

Figure F70. AMS data from selected discrete samples, Hole U1438D. Red = maximum principal axes of AMS ellipsoids, blue = minimum principal axes of AMS ellipsoids. Produced using Rick Allendinger's Stereonet program v. 8.9.6 (Cardozo and Allmendinger, 2013).

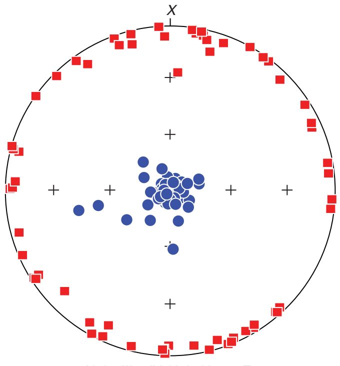

Units III + IV, Hole U1438E
Eocene sediments

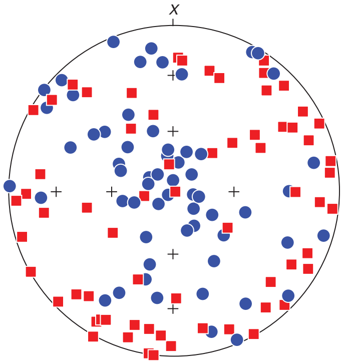

Unit 1, Hole U1438E
Basaltic basement

paring them with data from the 25 and 40 mT steps to identify samples with demagnetization paths trending broadly to the origin (see the **Expedition 351 methods** chapter [Arculus et al., 2015a]).

Shipboard paleomagnetic results identify a series of normal and reversed magnetozones to 846.8 mbsf (throughout Holes U1438A [Figure **F71**], U1438B [Figures **F72**, **F73**, **F74**, **F75**], and U1438D [Figure **F76**]). These examples show an excellent correlation to the geomagnetic polarity timescale (GPTS; Gradstein et al., 2012; Cande and Kent, 1995), providing a high-resolution magnetostratigraphy that extends to the base of GPTS Chron C16n.1r (36.051 Ma; Priabonian stage of the Eocene). Deeper in Hole U1438E, no clear reversals were identified, although positive inclinations throughout the sedimentary succession in this hole are consistent with paleontological constraints that place much of this succession in the latest middle to upper Eocene (when the geomagnetic field had a dominantly normal polarity) (Figure **F77**).

Overall, a total of 87 geomagnetic reversals may be correlated to the GPTS with confidence, providing a high-quality age-depth model for Site U1438. These correlations provide a shipboard chronostratigraphic framework for interpreting the Pleistocene to late Eocene sediment record at Site U1438 (Table **T16**). The most salient features of this age model (Figure **F78**) include the following:

- Average linear sedimentation rates during the Pliocene–Pleistocene were 1.4–2.2 cm/ky.
- Lower sedimentation rates of 0.25–0.5 cm/ky prevailed throughout the Miocene.
- Sedimentation rates were significantly higher during the Oligocene to late Eocene with a maximum of ~20 cm/ky.

Figure F71. Archive-half core remanent inclination data and magnetostratigraphy, Hole U1438A. For Figures F71 through F75: inclination measured after 25 mT AF demagnetization. Data from within 4.5 cm of section ends have been excluded. Magnetozones are based on inclination data and examination of orthogonal vector plots of demagnetization data and are correlated to the geomagnetic polarity and geological timescales of Gradstein et al. (2012).

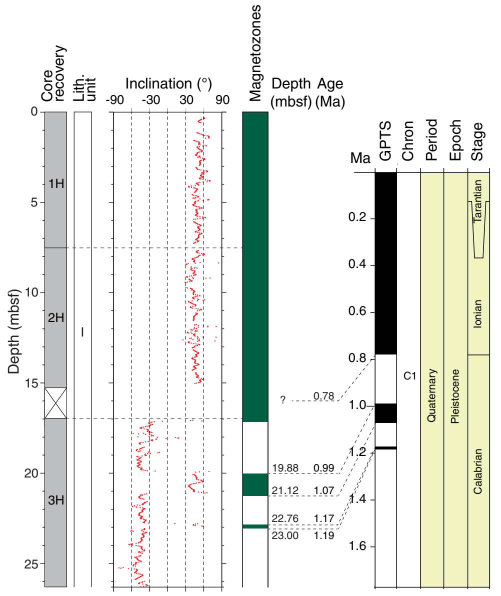

Figure F72. Archive-half core remanent inclination data and magnetostratigraphy, Hole U1438B, 0–50 mbsf.

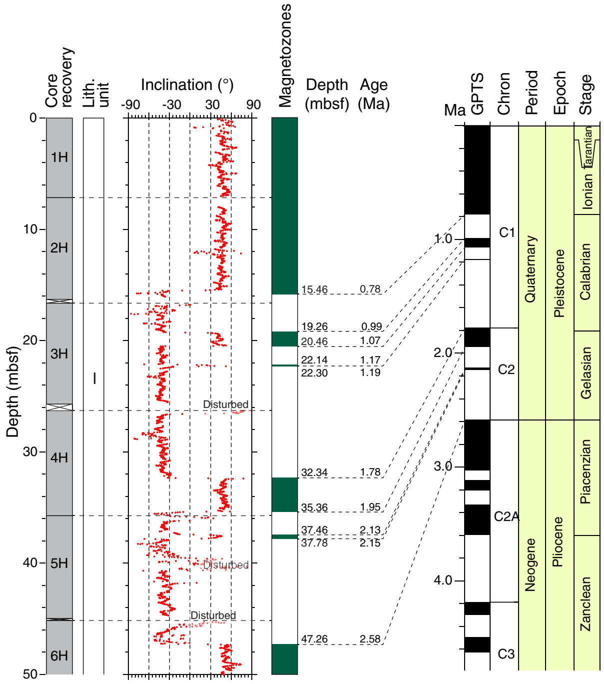

Basaltic basement rocks as a potential source of marine magnetic anomalies

In mafic igneous rocks, low-field magnetic susceptibility (k) is principally controlled by the volume concentration of magnetite. NRM variability is also controlled by variations in magnetite con-

Figure F73. Archive-half core remanent inclination data and magnetostratigraphy, Hole U1438B, 50–100 mbsf.

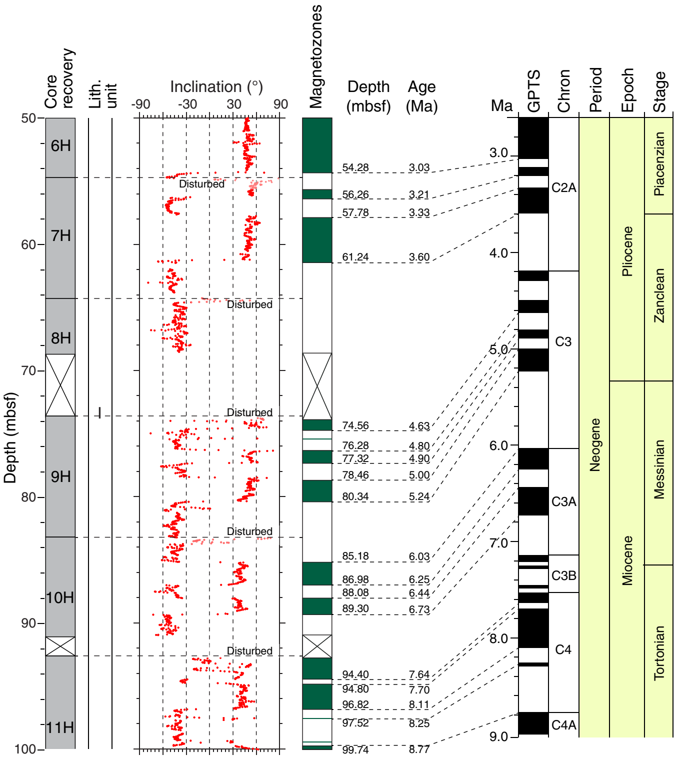

Figure F74. Archive-half core remanent inclination data and magnetostratigraphy, Hole U1438B, 100–150 mbsf.

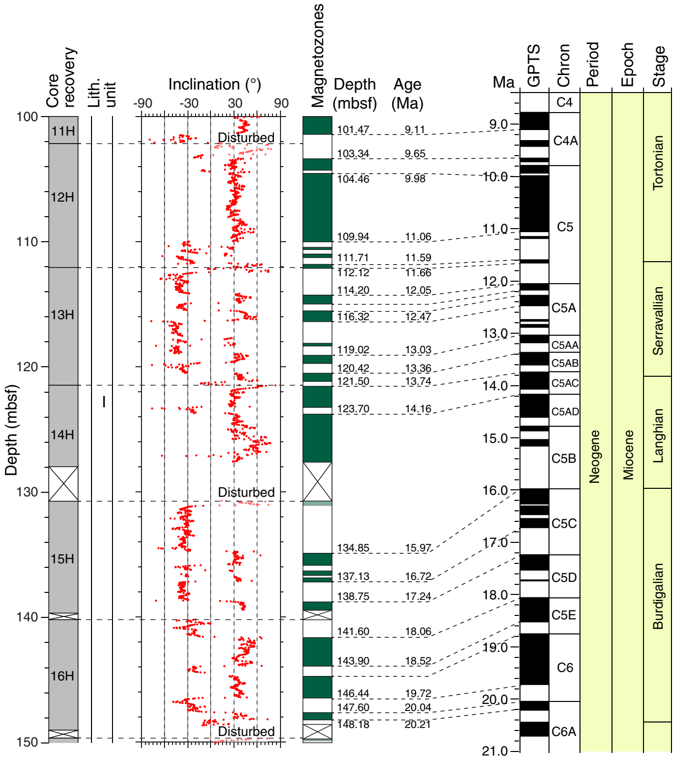

Figure F75. Archive-half core remanent inclination data and magnetostratigraphy, Hole U1438B, 150–200 mbsf. No usable data were acquired from Core 351-U1438B-25X.

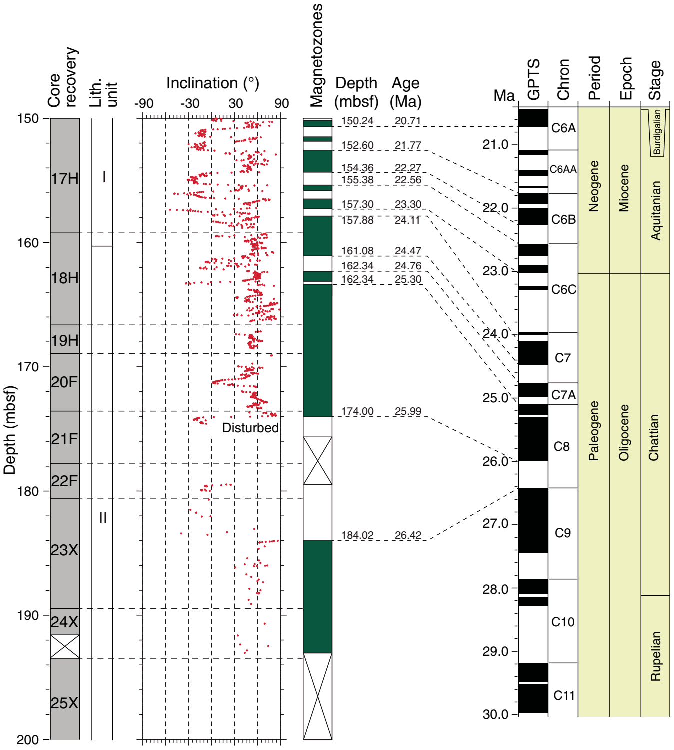

tent but may additionally be influenced by variability in the magnitude of drilling-induced remanent magnetizations. The relationship between NRM intensity and susceptibility is expressed by the Königsberger ratio, *Q*, which is defined as the ratio of remanent to induced magnetization in a rock (where induced magnetization equals the product of *k* [SI] and the geomagnetic field strength in A/m). Values of $Q > 1$ indicate that remanence dominates the magnetization of a rock unit.

Figure **F79** shows a log-log plot of NRM intensity against *k* for archive-half core samples from basaltic rocks of Hole U1438E, together with lines of equal *Q* calculated for a field of 32.2 A/m. The majority of samples plot above $Q = 1$. This suggests that these rocks have the potential to contribute a significant fraction to marine magnetic anomalies. However, caution is required in the interpretation of Q ratios calculated for these samples, as NRM intensities may be artificially increased by drilling-induced magnetization.

Figure F76. Archive-half core remanent inclination data and magnetostratigraphy, Hole U1438D, 200–900 mbsf. PCA piece averages = inclinations of piece-averaged principal components (after filtering out PCA picks with maximum angular deviations > 10°). Magnetozones are based on the inclination data and examination of orthogonal vector plots of demagnetization data, and are correlated to the geomagnetic polarity and geological timescales of Gradstein et al. (2012). For Figures F76 and F77: PCA 40 mT = piece-averaged PCA directions that have the same sign as the piece-averaged 40 mT demagnetization data. PCA 15° = piece-averaged PCA directions that have <15° angular difference with the piece-averaged 25 mT demagnetization data. Green = piece averages with $\alpha_{95} \leq 15°$, red = piece averages with $\alpha_{95} > 15°$, black = pieces with single measurement points, where α_{95} = Fisher (1953) 95% cone of confidence around the mean direction. Remanence data from within 4.5 cm of a piece end have been excluded.

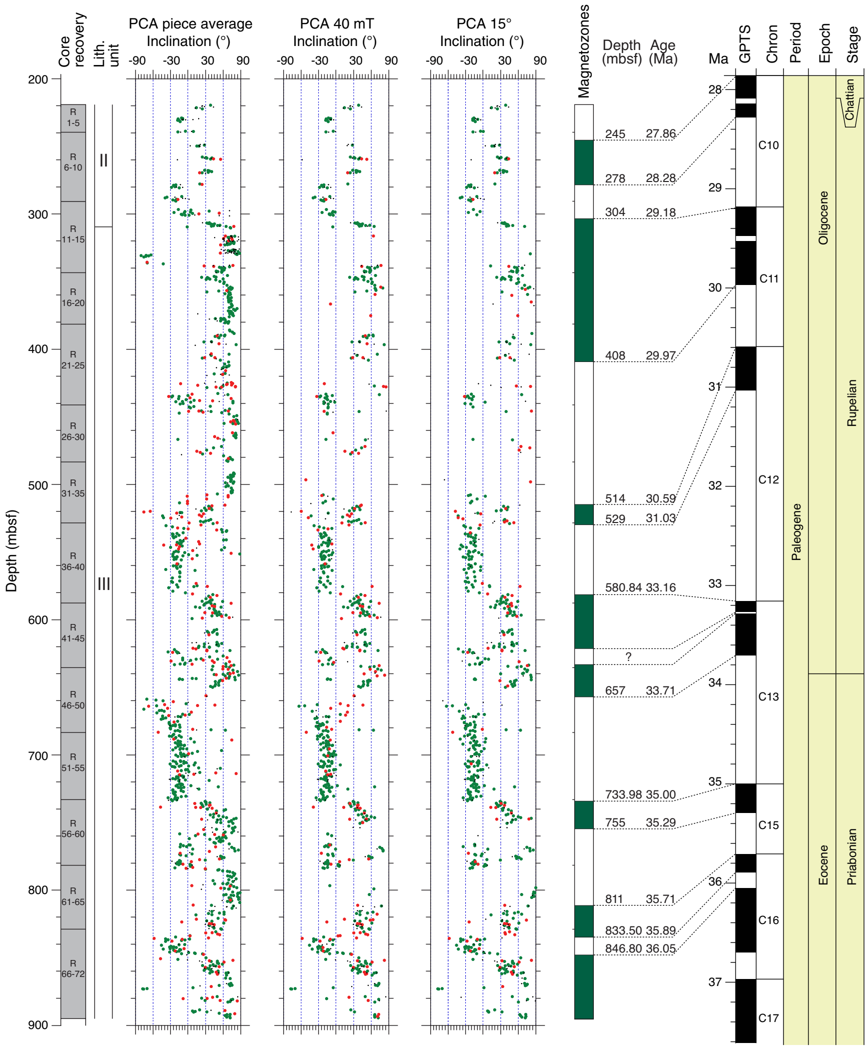

Figure F77. Archive-half core remanent inclination data and magnetostratigraphy, Hole U1438E.

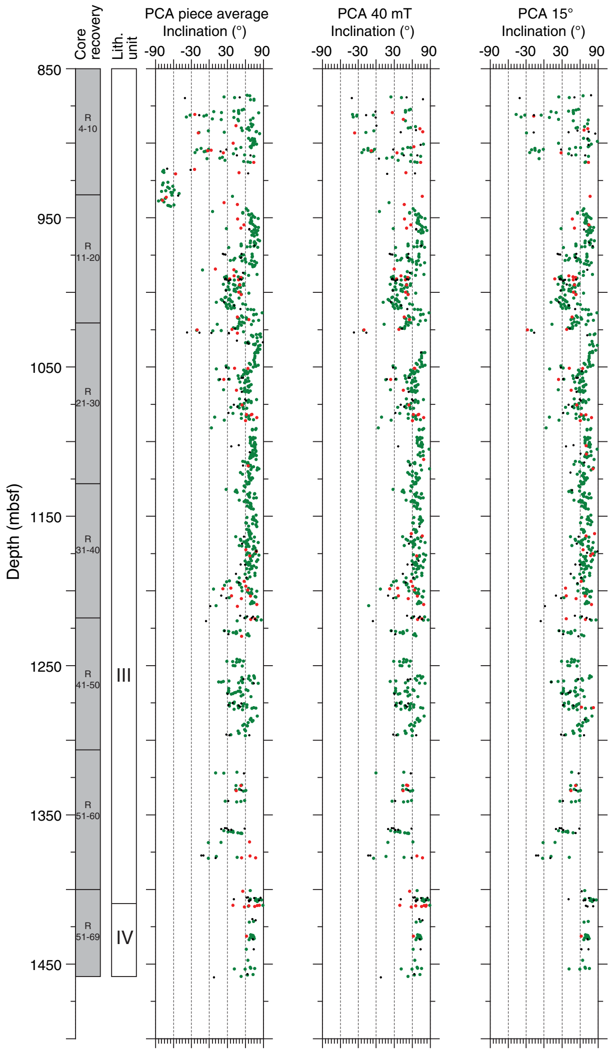

Table T16. Age-depth relationships for Hole U1438B, based on correlation between magnetozones and the geomagnetic polarity timescale. **Download table in .csv format.**

Figure F78. Age-depth model based on correlation between magnetozones and the geomagnetic polarity timescale of Gradstein et al. (2012) (Figures F72–F76), with corresponding calculated linear sedimentation rates, Holes U1438B and U1438D.

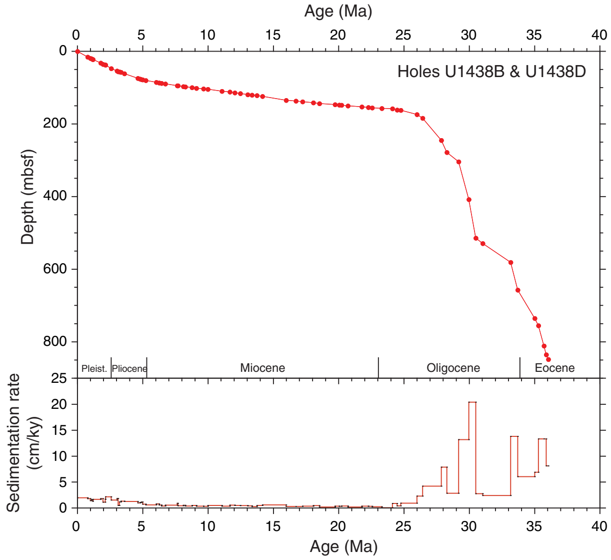

Figure F79. Log-log plot of NRM intensity vs. low-field magnetic susceptibility of archive-half core samples of basaltic basement rocks, Hole U1438E. Distribution of values compared to lines of constant Q (Königsberger ratio of remanent to induced magnetization; calculated for field of 32.2 A/m) shows that remanence is substantially greater than induced magnetization in most samples.

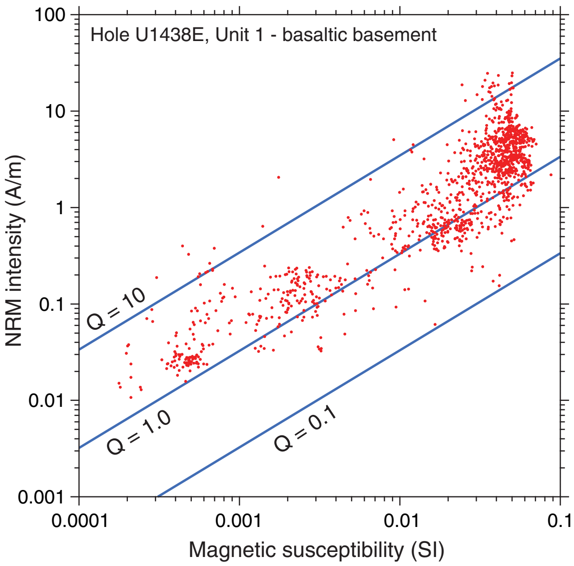

Physical properties and downhole measurements

At Site U1438, physical property and downhole measurements were made to help characterize lithostratigraphic units and provide a basis for linking lithostratigraphy to crossing seismic lines. In addition, with the logging results we have characterized the thermal state of the site and in turn estimated the heat flux from the lithosphere. We also estimated the strength of the sediments within the upper part of the site (Hole U1438B).

After the recovered cores reached thermal equilibrium with room temperature (~4 h), whole cores were scanned with the Whole-Round Multisensor Logger (WRMSL) to measure gamma ray attenuation (GRA) as a proxy for material density, magnetic susceptibility, and P-wave velocity. The whole rounds were then logged for natural gamma radiation (NGR) and thermal conductivity. After splitting the cores, the archive-half core sections were run through a digital imaging logger (Section Half Imaging Logger [SHIL]), magnetic susceptibility point analyzer, and color spectrophotometer on the Section Half Multisensor Logger (SHMSL). On working-half sections, shear strength and P-wave velocity were measured. Discrete samples were also taken from the working half, generally one per section, for measurements of thermal conductivity, moisture and density (MAD), and P-wave velocity. Details of all measurements made on the whole-round core sections, the working-half sections, and discrete samples are included in **Physical properties** in the Expedition 351 methods chapter (Arculus et al., 2015a).

Additionally, Holes U1438D–U1438F were logged. Several meters of overlap between each hole were measured to have a continuous record of the sediment physical properties and to compare and create a link between data from each hole. Because of hole conditions in Holes U1438D and U1438E, only data from the triple combo (see **Downhole measurements** in the Expedition 351 methods chapter [Arculus et al., 2015a]) tool string were collected (see **Operations**). Only Hole U1438F was measured with the entire set of tool strings available, leading to a complete data set from 90 to 700 mbsf. Finally, the third-party tool, the Göttingen Borehole Magnetometer (GBM), was run in Hole U1438E, potentially giving magnetic orientation data from 605 to 1200 mbsf when these data are processed postexpedition.

Logging data quality

From 90 to 160 mbsf, rapid variations in borehole diameter were observed and may result in underestimation of the density data and overestimation of the porosity data (Figure **F80**). From 160 to 300 mbsf, the hole diameter was smaller and smoother, and from 300 to 700 mbsf, the hole was in gauge. Both of these intervals provided the best conditions for logging, leading to acquisition of high-quality data. Deeper than 700 mbsf, the hole diameter was greater than 43 cm. Resistivity, gamma ray, and magnetic susceptibility are less affected by wide borehole diameter. Variations of hole size encountered in the upper 300 mbsf may reflect lithology. Throughout the logged intervals, gamma ray, resistivity, magnetic susceptibility, velocities, and Formation MicroScanner (FMS) images are all judged to be of good quality. In Holes U1438D and U1438F, the main pass of the triple combo was used as the depth reference, whereas we used the resistivity data for Hole U1438E. In general, all logging data show a good agreement with core data (Figures **F80**, **F81**, **F82**). Logging data also co-vary, confirming they are overall of good quality. Moreover, the data do not show gaps or jumps in values between

Figure F80. Summary of triple combo logs compared with logging and lithostratigraphic units.

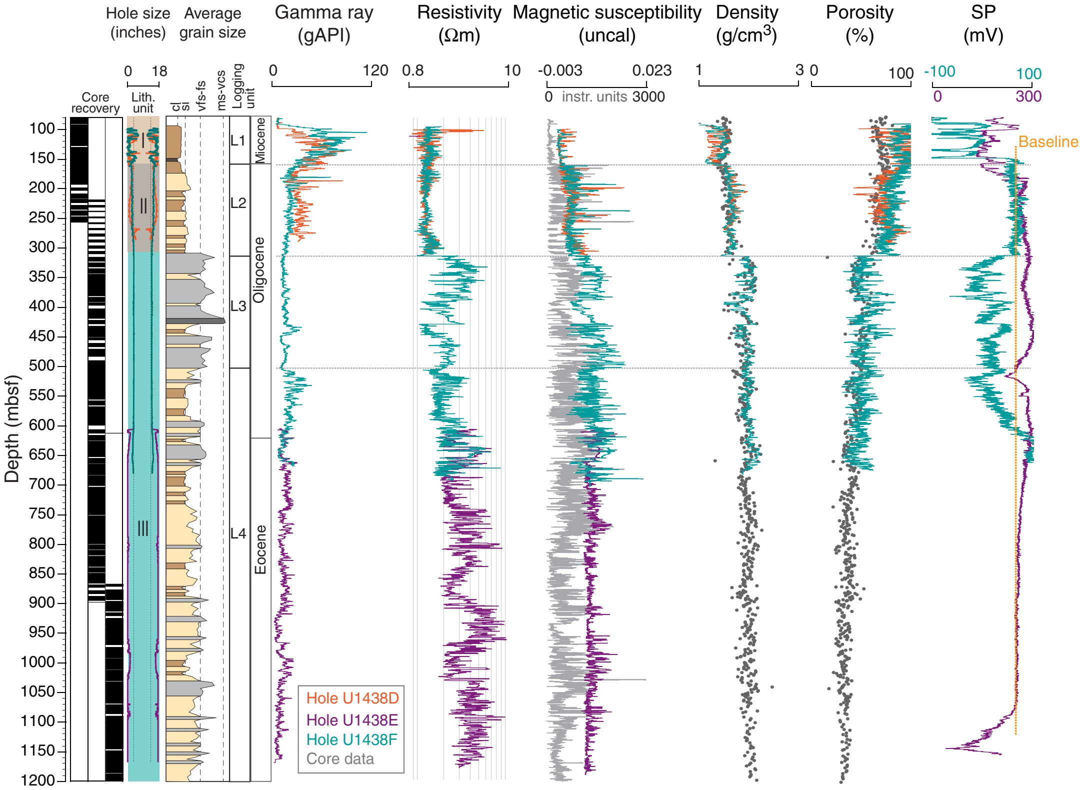

Figure F81. Summary of sonic velocities recorded with the FMS-sonic tool string. P-wave sonic velocities are compared with core data. Vertical seismic profile waveforms and one-way arrival time picks (red stars) for Hole U1438F are also shown.

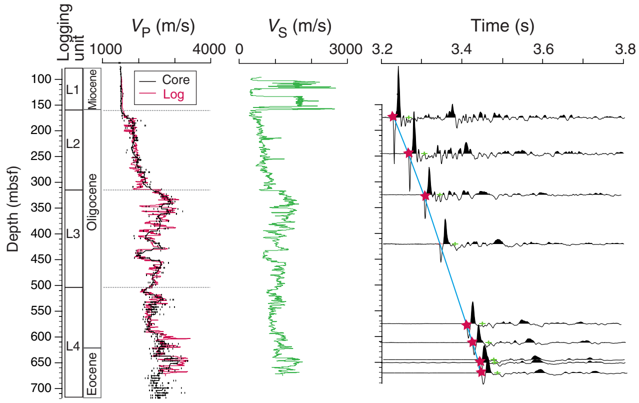

the different logged holes. Four logging units were defined. Logging Units 1 and 2 essentially correspond to lithostratigraphic Units I and II, whereas lithostratigraphic Unit III was divided into two logging units (3 and 4).

Density and porosity

Sample density and porosity were obtained by measuring the wet and dry density and dry volume of discrete samples as described in **Physical properties** in the Expedition 351 methods chapter (Arculus et al., 2015a).

Porosity decreases overall with depth at Site U1438 from 75% to 25% through Units I–IV, at which point, at the boundary with Unit 1, the porosity drops to a only few percent over 40 m (Figure **F83**). The reduction in porosity within Units I to IV is fit approximately by an exponential function with a decay constant of 1200 m, typical of the behavior seen for shales. With the overall reduction in porosity reflecting compaction and lithification of the sediments, deviations from the exponential allow identification of changes not simply related to compaction. Alongside this change in porosity

Figure F82. Summary of natural and spectral gamma radiation and correlation with core data. cl = clay, si = silt, vfs-fs = very fine sand–fine sand, ms-vcs = medium sand–very coarse sand.

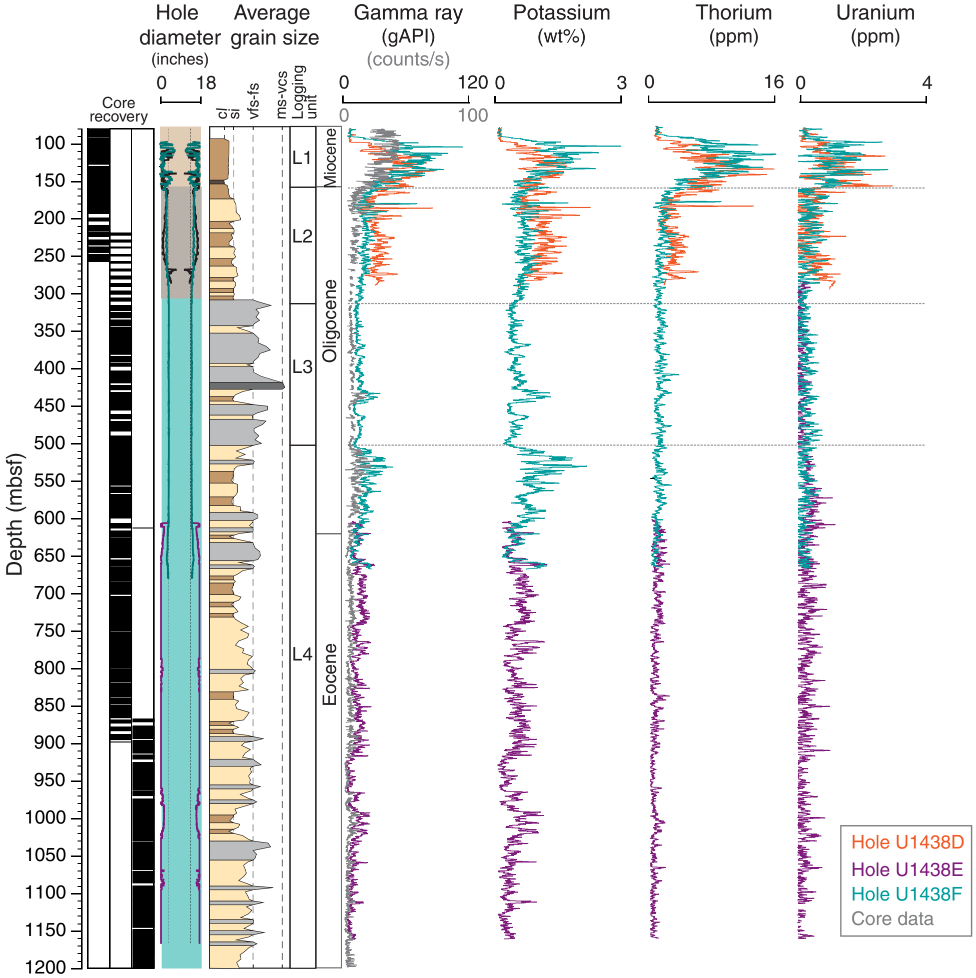

Figure F83. Physical properties, Holes U1438B (green), U1438D (red), and U1438E (blue). V_P was determined using *x*-direction caliper measurements on working halves. Bulk density (ρ_b), grain density (ρ_g), and porosity (ϕ) were measured on discrete samples with MAD method C. Small gray dots = GRA bulk density. Blue line through the porosity data = simple exponential function with a decay constant of 1200 m. Raw magnetic susceptibilities (κ_{MEAS}) and NGR were measured on whole rounds.

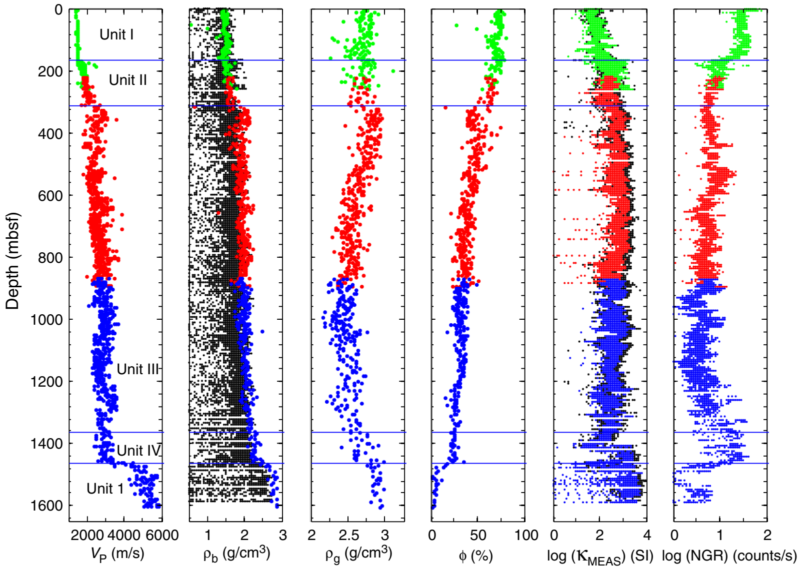

through the units, bulk density shows a small progressive increase from 1.45 g/cm^3 at the seafloor to 2.3 g/cm^3 at the boundary between Unit IV and Unit 1. Grain density shows important changes in value with depth that are more closely associated with variations in lithology.

Although porosity decreases as a whole with depth, we also find significant variations from this overall trend (Figure **F83**). One of the largest changes coincides with the boundary between Units II and III, at which bulk density and grain density change from 1.75 to 2.0 g/cm^3 and from 2.75 to 2.9 g/cm^3, respectively. These changes occur over 20 m just below the boundary between Unit II and III. The upper 40 m of Unit III is characterized by a reduction in porosity from 62% to 45%. Another major change occurs at the boundary between Unit III and IV and is most noticeable in grain density, which increases from 2.6 to 2.7 g/cm^3.

Other notable changes occur in the properties of the cores. Outside of the isolated reduction in porosity within the upper 40 m of Unit III, the porosity of this unit progressively decreases and is well fit by the aforementioned exponential decay. However, when the variance between discrete samples is accounted for, the average grain density reaches a minimum at ~800–900 mbsf with a grain density of 2.5 g/cm^3. The average grain density then slowly increases again to the base of Unit III, where the average value is about 2.6 g/cm^3.

The downhole logging data also decrease overall in porosity with depth at Site U1438 with a sharp decrease between logging Units 2 and 3 at 310 mbsf (Figure **F80**). All of these variations correspond with what is observed in the cores, even if porosity recorded by logging was slightly greater than porosity measured in the cores. The bulk density values measured in the logs are in good agreement with the bulk density measured on cores and display the same variations with notable changes at 160, 310, and 660 mbsf. These variations correspond to changes in lithology. In addition, porosity calculated from the density profile assuming a grain density of 2.8 g/cm^3 (from core data) is in agreement with the porosity obtained down the hole, except where the larger diameter of the upper part of the hole (upper 300 mbsf, Holes U1438D and U1438F) led to overestimation of the porosity measured with the APS sonde (see Downhole measurements in the **Expedition 351 methods** chapter [Arculus et al., 2015a]).

Sediment strength

The upper layers recovered from Hole U1438B are unconsolidated muds with little strength. Shear strength measurements were made with the automated vane shear (AVS) instrument in Unit I. Shear strength increased from 18 kPa at 2 mbsf to 70 kPa at 90 mbsf (Figure **F84**), reflecting progressive consolidation and partial lithification of sediments. Measurements were interrupted between about 90 and 160 mbsf, as the sediments were initially deemed to be too stiff to continue with the AVS, which in general requires undrained core samples. Measurements continued again between 160 and 170 mbsf because the mud layers there were judged to have sufficient pore water. Deeper in the hole, we found that shear strength ranged widely from 53 to 176 kPa, potentially depending on abundance of pore water.

Sonic and seismic velocities

P-wave sonic velocities were measured in a number of ways through the entire depth range recovered at Site U1438. In cores from Hole U1438B to 174 mbsf (Core 351-U1438B-20F), sonic velocities were obtained from both whole rounds and working-half core sections using calipers in the *x*-direction and bayonets in the *z*-direction, respectively. Sonic velocity measured using the bayonets did not give consistent values, and values faster than 1800 m/s in the shallow depth range of Hole U1438B were judged to be spurious and removed. Figure **F85** shows sonic velocities measured on the cores in different ways. In Hole U1438B, measurements of GRA with the WRMSL (small black dots), calipers in the *x*-direction (red dots), and bayonets in the *z*-direction (blue dots) gave consistent results. In Hole U1438D, sonic velocities were only measured in the *x*-direction with the caliper on the working-half section. In Hole U1438E, sonic velocities were measured using calipers (small red

Figure F84. Shear strength (σ_s) of sediments measured by automatic vane shear, Hole U1438B.

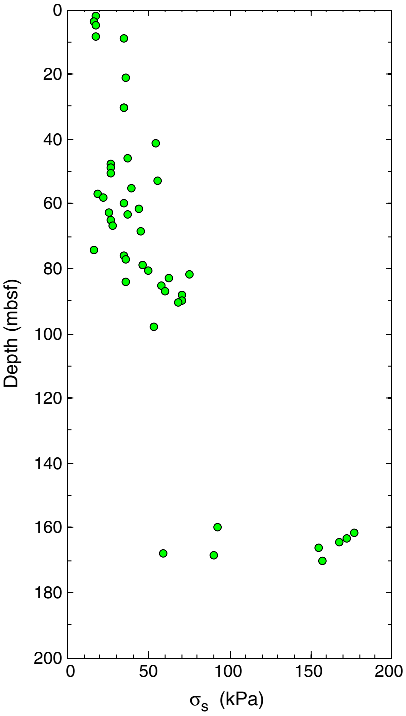

dots) and orientated cubes in the *x*-, *y*-, and *z*-directions (green dots). These final measurements were judged to be superior because the square edges of the cut cubes had good contact with the calipers (green dots), but we found these to be consistent with those on the working-half sections (small red dots). The anisotropy of the sonic velocities was also directly determined from these measurements.

The average sonic velocity is 1500 m/s to 160 mbsf (Core 351-U1438B-18H), consistent with unconsolidated mud. Velocity measurements from the whole rounds and from the caliper for the split sections are shown in Figure **F85**. Measured values in the *x*- and *z*-directions are in agreement, indicating the velocities are isotropic, consistent with the lack of any substantial horizontal layering in the muds. At ~160–170 mbsf, the sonic velocities start to increase from 1500 to 1900 m/s, and the increase is complete by about 190 mbsf. The change in velocity is associated with a change from mud to mudstone with clasts and is correlated with the transition from Unit I to II. The variation in P-wave sonic velocity within the depth interval 190–250 mbsf (Cores 351-U1438B-24X through 30X; Unit II) is between 1700 and 2000 m/s, where higher velocities are associated with mudstones with clasts and lower velocities are associated with mudstones without clasts. Three P-wave sonic velocity data points exceeding 2000 m/s between 170 and 190 mbsf may be artifacts, as there was not a substantially notable change in lithology within Cores 351-U1438B-20X through 23X. Sonic velocity of 1540 m/s at ~240 mbsf is also likely an artifact, as the corresponding core section (351-U1438B-29X-1) is severely broken up.

Figure F85. P-wave sonic velocities measured on cores, Holes U1438B, U1438D, and U1438E. Hole U1438B: small black dots = whole round measurements every 2.5 cm along the core section. Red dots = *x*-direction caliper measurements on working halves. Blue dots = *z*-direction bayonet measurements on working halves. Hole U1438D: *x*-direction caliper measurements on cores. Hole U1438E: small red dots = *x*-direction caliper measurements on working halves. Green dots = caliper measurements on cubes cut from working halves; value plotted is mean of *x*-, *y*-, and *z*-directions. Error bars = 2σ between the three measurements.

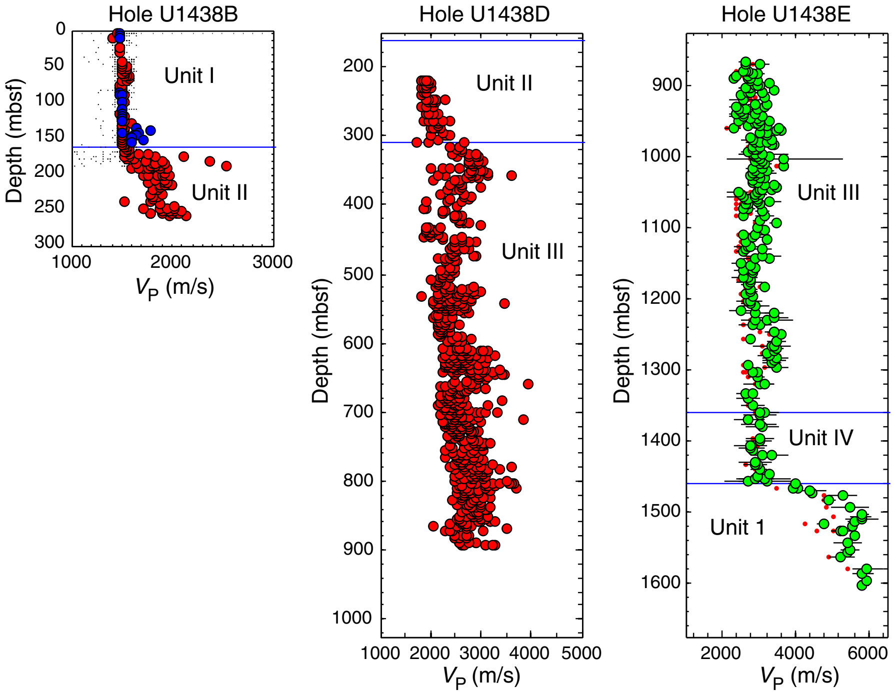

At 255 mbsf (Section 351-U1438B-30X-5), there is another increase in P-wave sonic velocity that is complete by ~340 mbsf (Section 351-U1438D-15R-4) (Figure **F85**); this velocity increase is associated with the appearance of Unit III (conglomerates with volcanic and sedimentary clasts) at 310 mbsf (Core 351-U1438D-12R). Within the interval of 310–900 mbsf, the velocities on average increase from about 2400 to 2800 m/s; however, there are distinct zones of higher velocity (around 2800–3200 m/s) around 320–360, 600–660, and 780–810 mbsf that correlate with the occurrence of tuffaceous sandstone, breccia, and conglomerate, also with density higher than mudstone and siltstone (grain density = ρ_g ~ 2.7–3.0 g/cm^3) (Figure **F85**). A higher velocity zone is also found around 520–540 mbsf that correlates with the occurrence of tuffaceous sandstone. Within this layer, there are sharp reductions in sonic velocity, most clearly shown at 540 mbsf (Sections 351-U1438D-36R-1 and 36R-2) (Figure **F85**), that correspond to an increase of tuffaceous mudstone as the dominant lithology.

P-wave sonic velocities within Unit III in Hole U1438E show a similar range of variation as found in Hole U1438D, ranging in value from 2400 to 3200 m/s (Figure **F85**). The most significant change in sonic velocity occurs in the depth range 1250–1300 mbsf, which is characterized by occurrence of siltstone as the dominant lithology. Sonic velocities between 1250 and 1300 mbsf also display a form of transverse anisotropy. The azimuthal variation in sonic velocities that is around a horizontal plane are generally around 2% and are much smaller than those between the horizontal and vertical planes, which are between 0% and 15% (Figure **F86**). The sonic anisotropic values are correlated with lithology; mudstones and fine sandstones with and without apparent bedding planes generally have higher sonic anisotropic values than the coarser sandstones. The apparent seismic anisotropy in the core data within Unit III is large enough to have an effect on the inference of structure from the seismic reflection profiles.

Figure F86. Anisotropy of sonic velocities, Hole U1438E. Left: percent difference in sonic velocities between the *x*- and *y*-directions. The cores are not oriented in the horizontal plane and so the absolute value ($|V_x - V_y|$) is shown. Right: percent difference between the mean horizontal values and the vertical P-wave sonic velocity, expressed as an absolute value.

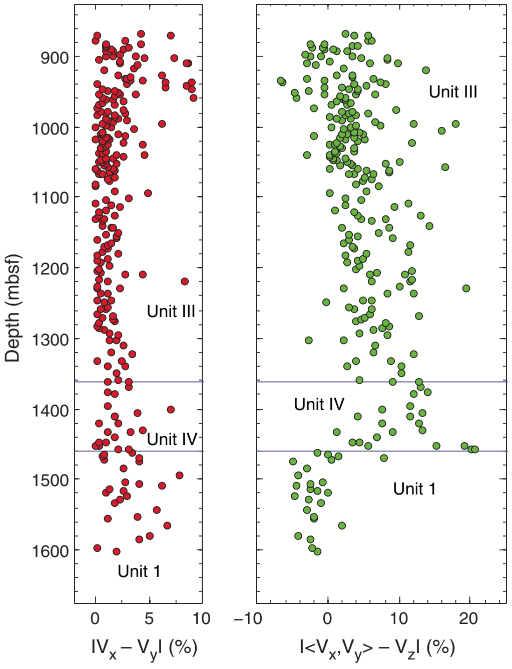

Within the lithologically diverse Unit IV, composed of mudstone, siltstone, and conglomerates, the average sonic P-wave velocity is around 2800 m/s. The start of Unit IV at 1361 mbsf is not characterized by a change in P-wave sonic velocity compared to overlying Unit III. The sample-to-sample variance in P-wave sonic velocities in this layer is smaller than that in overlying Unit III. However, within the top half of Unit IV, the apparent seismic anisotropy, in which horizontal velocities are 13% higher than the vertical velocities, is larger than that in Unit III near the Unit III/IV boundary (<10%) (Figure **F86**).

The start of Igneous Unit 1 at 1461 mbsf is characterized by an abrupt increase in P-wave sonic velocity (Figure **F85**). The first measurement of sonic velocity at 1461.4 mbsf (Core 351-U1438E-69R) has an average value of 3984 m/s. However, the sonic velocities rapidly increase to 5600 m/s over a depth range of 80 m. The apparent seismic anisotropy of Unit 1 rapidly decreases from nearly 20% above the boundary to near 0% below the boundary at 1461 mbsf. The large and rapid jump in sonic character within the core gives rise to a distinct and unambiguous seismic reflector.

P-wave velocities measured downhole were repeatable between logging runs and so were considered to be robust. The P-wave velocities obtained from logging also correlate well with the core data (Figure **F81**), which may sometimes be underestimated in comparison with in situ velocities because of removal of high-pressure conditions. The velocities obtained during logging show an increasing trend with depth, range from 1500 to 3500 m/s for the P-wave and from 300 to 3000 m/s for the S-wave, and exhibit distinct variations between the different logging units. The average P-wave velocity is 1500 m/s to 160 mbsf and then increases to an average velocity of 1850 m/s to 310 mbsf. At that depth, P-wave velocities increase again to a mean value of 2500 m/s. They slightly decrease from 420 to 590 mbsf, where they reach values around 2700 m/s. The interval between 420 and 460 mbsf is particularly low, with values at 2000 m/s. In addition to P-wave velocities, we recorded S-wave velocities during logging. Both lower and upper values of shear and compressional velocities are highly correlated. To 310 mbsf, S-wave velocities are slow and typical of water-saturated clay and shales (from 300 to 900 m/s). From 310 to 420 mbsf, S-wave velocities average around 1100 m/s and decrease to a mean velocity of 655 m/s in the 420–460 mbsf interval. From 460 to 540 mbsf, S-wave velocities increase again to about 1000 m/s and reach an average velocity of 1355 m/s at 590 mbsf. All of these velocities are reasonable and are in the ranges expected for the sediment types encountered at Site U1438.

Downhole temperature and thermal conductivity

Successful temperature measurements were made at seven depths using the APCT-3 from the mudline to 83.2 mbsf in Hole U1438B (see **Operations** for core numbers). The temperatures as a function of depth did not show any substantial deviation from a linear geothermal gradient of 77.6°C/km (Figure **F87**). We also made 28 measurements of thermal conductivity (k) on cores from Hole U1438B that were approximately evenly spaced to 100 mbsf and found they did not vary substantially, with a mean of 0.951 ± 0.046 W/(m·K). A combination of temperature measurements and thermal conductivity using Bullard-type analysis (see **Downhole measurements** in the Expedition 351 methods chapter [Arculus et al.,

Figure F87. Temperature, thermal conductivity (k), thermal resistance (Ω) and a Bullard plot from downhole measurements.

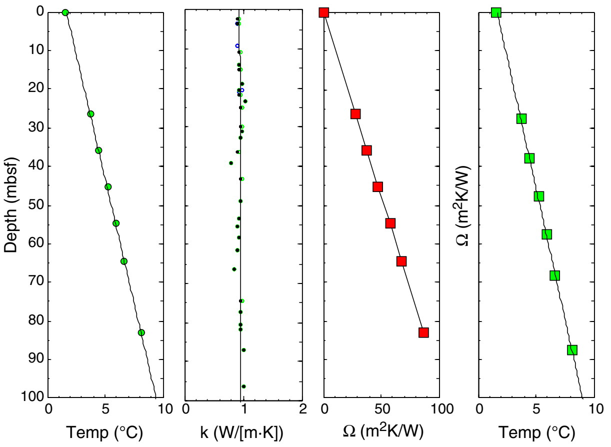

2015a]) indicated the thermal gradient did not change with depth in the upper part of Hole U1438B. This suggests the geotherm is undisturbed by local processes, such as sediment compaction, fluid flow within the porous sediments, or internal heat production from radioactive decay. With these thermal conductivities measured on the recovered core, the calculated heat flow is 73.7 mW/m^2. In addition, thermal conductivity was also measured throughout Holes U1438A, U1438B, U1438D, and U1438E (Figure **F88**).

In Unit I, thermal conductivity is constant within error between about 0.9 and 1 W/(m·K). At the Unit II/III boundary, thermal conductivity jumps by a small amount from about 0.95 to 1.0 W/(m·K) and then through Unit III slowly increases from 1.0 to about 1.4 W/(m·K) at 1200 mbsf. The rate of increase in thermal conductivity increases with depth below 1200 mbsf. The variance in measured values precludes any assessment of a significant change in the rate of increase of thermal conductivity with depth at the Unit IV/Unit 1 boundary. The increase in thermal conductivity with depth in Unit III is mostly controlled by the decrease in the porosity of the mud and sand in this unit (Figure **F83**).

Color spectrometry

Reflectance of visible light from the archive-half sections was measured with the automated SHMSL. Spectral data are routinely reduced to the L*a*b* color space, in which L* is luminescence (light/dark), a* is the red–green value, and b* is the blue–yellow value (see **Physical properties** in the Expedition 351 methods chapter [Arculus et al., 2015a]). To 160 mbsf (Unit I), three major peaks in a* and L* values at 80–100, 125–140, and ~160 mbsf are characterized by the occurrence of thick light brown mud layers (Figure **F39**). Between 160 and 310 mbsf (Unit II), a* and L* values are relatively uniform where thick tuffaceous mudstone dominates. Below the Unit II/III boundary at 310 mbsf, L* and a* values progressively decrease. These color spectrometric changes are related to the occurrence of sandstone and conglomerate in Unit III. Peaks of L* values observed at ~510, 560, and 580 mbsf correspond to negative peaks of a* values and average particle sizes. These negative peaks are related to the occurrence of green-colored tuffaceous siltstone and/or mudstone. Below 600 mbsf, major peaks of a* values occur at ~630, ~730, ~880, and ~1030 mbsf and are correlated with the occurrence of red mudstone. Oscillation of a* values observed deeper than 1200 mbsf (Units III–IV) originates from the frequent occurrence of red and green intercalated layers.

Figure F88. Thermal conductivity measured using discrete samples.

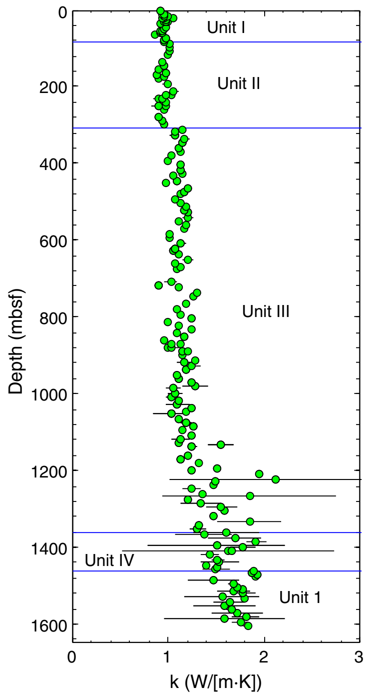

Natural gamma radiation

Some of the changes evident in the sonic velocities, porosity, and density, and their correlation with unit boundaries and grain size, are evident in the NGR data (Figure **F83**). Overall, Unit I is characterized by both large average NGR as well as large variations in NGR with depth, with the highest levels of NGR, 25 and 50 counts/s, occurring within the upper 10 m of Hole U1438B. There is a strong decay in the NGR within this upper layer of unconsolidated mud. Outside of this thin, high-NGR layer, Unit I can be divided into two regions. In the upper region above 70 mbsf (but below the upper 10 m of mud), NGR is around 30 counts/s, whereas in the region between 70 and 160 mbsf (Cores 351-U1438B-9H through 17H), NGR is much higher and characterized by readings of about 40 counts/s. These variations in NGR reflect compositional variations in U, Th, and K and are more clearly evident in the downhole logging data (Figure **F80**). The upper 160 m section, characterized by uniform but low P-wave sonic velocities (as detailed above), has higher NGR compared to the region deeper than 160 mbsf, likely associated with the higher mud-to-sand ratio of the upper layer.

The Unit I/II boundary (160 mbsf) is associated with a substantial decrease in NGR, with Unit II having values around 8–10 counts/s. The change in NGR reflects a compositional change from a unit dominated by mud and clay to one with mudstone, siltstone, and fine sandstone and with much smaller concentrations of K, Th, and U, as evident from downhole logging (Figure **F82**). The unit boundary is also characterized by a small increase in grain density (but not bulk density) and a small increase in porosity. Within the sandstones, mudstones, and breccia-conglomerates of Unit III, NGR oscillates between 3 and 24 counts/s. NGR reaches a minimum between 920 and 990 mbsf (Cores 351-U1438E-10R through 17R), with values of 2–5 counts/s. Some of the largest NGR values occur within the lowest parts of Unit III from 1290 mbsf (Core 351-U1438E-49R) to the base of Unit III (Section 55R-3), where NGR increases from 4 counts/s to about 25 counts/s over 70 m (Figure

F83). On average, Unit IV, composed of mudstone, siltstone, sandstone, and conglomerates, has relatively high NGR with values of 15–25 counts/s, but still less than those of Unit I. These elevated values indicate a distinct change in the trace element composition of Unit IV in comparison with the average of Unit III.

NGR drops abruptly at the boundary between Unit IV and Unit 1 to 2–5 counts/s within the basement. Across the sedimentary rock/basement boundary, the drop in NGR is much more abrupt than that evident in P-wave velocity and porosity, indicative of an abrupt change in composition but a gradual change in the physical characteristics of the basement rock.

In the downhole logging data, from ~90 to 160 mbsf (logging Unit 1), gamma ray data have high values (average = 58 gAPI). Gamma radiation decreases to values averaging around 22 gAPI from 160 to 300 mbsf (logging Unit 2). Gamma ray values from deeper intervals average around 10 gAPI to 1200 mbsf with increases to 30 gAPI in the 420–450 and 500–600 mbsf intervals (Figure F82). Potassium generally shows high concentrations in Unit 1 (~1.3%) and in the intervals from 420 to 450 and from 500 to 580 mbsf (Figure F82) but decreases deeper in the hole, eventually reaching less than 1% with few exceptions. Thorium (Th) and uranium (U) share these same general concentration trends, but are present in high concentrations (Th = 8 ppm; U = 1.1 ppm) in logging Unit 1 and then decrease to average values of ~1.6 ppm (Th) and 0.3 ppm (U) in logging Unit 2 (Figure F82). The high radiation present in logging Units 1 and 2 may reflect the presence of discrete ash layers described throughout lithostratigraphic Units I and II in the cores (see **Lithostratigraphy**). These layers are characterized by a large increase in total gamma radiation and, particularly, in thorium content (Figure F82). The logging data might also indicate ash layers that cannot be visually observed in the cores (Figure F89; blue dotted lines) and therefore may help to refine the eruptive volcanic history of the region around the site.

Magnetic susceptibility

Magnetic susceptibility is an additional tool used in identification of compositional variation and varies primarily in response to the type and concentration of magnetic grains. Loop and point magnetic susceptibility (κ_{MEAS}) were measured on both the whole-round cores (with the WRMSL) and the archive-half sections (with the SHMSL), respectively (Figure F83). Downhole logging also recorded magnetic susceptibility data; both logs and laboratory measurements show the same variations (Figure F80).

Figure F89. NGR, K, Th, and U content and comparison with ash layers described in the cores, Hole U1438D. Dashed lines = ash layer that may have not been described in the cores.

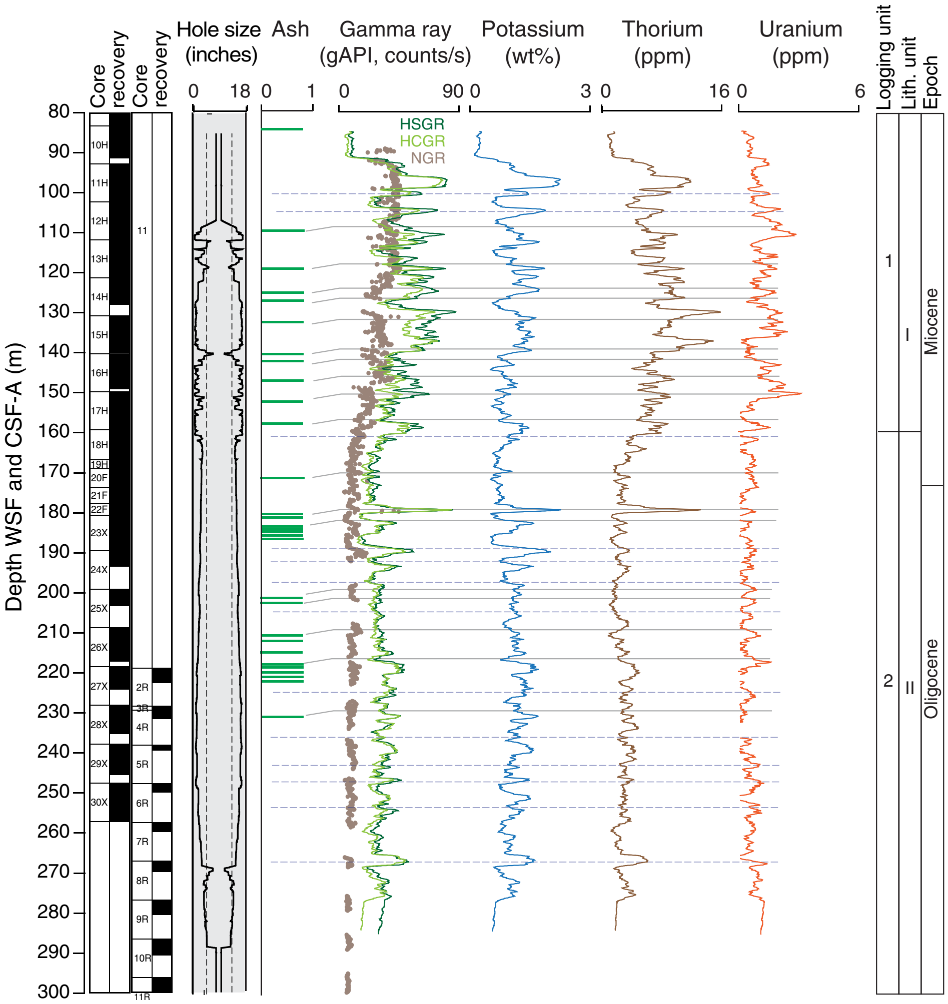

The upper 160 m (Unit I) has the lowest average magnetic susceptibilities of the entire site, which reflects the lithologic dominance of mud. The Unit I/II boundary (160 mbsf) is associated with a sharp increase in magnetic susceptibility that is correlated with the small increase in grain density and porosity described above. This reflects the more coarse grained nature of Unit II. The Unit II/III boundary is also characterized by a steep increase in magnetic susceptibility that stays high but variable. The oscillation of magnetic susceptibility through Units II and III is correlated with average grain size such that those core sections with higher sand and gravel relative to mud have higher magnetic susceptibility. These variations might be related to the alternations of mud and coarser material described within Unit III.

One of the largest changes downhole in magnetic susceptibility is a steep drop within Unit IV (Figure **F83**). The reduction is associated with the reappearance of mud at the top of Unit IV. Magnetic susceptibility jumps at ~1405 mbsf (Core 351-U1438E-61R) and increases to higher values in the mafic basement rocks of Unit 1.

Göttingen Borehole Magnetometer

Variations in magnetic flux density determined from the GBM data (Figure **F90**) show good correlation between data acquired on downward and upward passes. During data acquisition on both passes (downlogs and uplogs), the GBM followed a stable course with a constant and slow rotation inside the hole. However, there were a few sections with increased rotational velocity due to the release of built-up cable torque, creating “spikes” in the data. While running the uplog in the upper part of the open hole, these spikes developed into a constant oscillation. Given the fact that rotational velocities did not appear to be severely high and because of tight scheduling, the pulling speed was not reduced. Rotational rates during the spike events and oscillations in the later part of the uplog exceeded 40°/s, outranging the limits of the fluxgates’ low-pass filters and resulting in incorrect measurement of the horizontal component of the magnetic flux density in these areas. This affects 12% of the downlog data and 24% of the uplog data but may be reduced by combining intervals of undisturbed data during postexpedition processing. The orientation measurements of the GBM are not influenced because of their higher acquisition rate. Additionally, five major data losses of approximately 1 min each occurred during operations. As a result, the second heading measurement at the end of the logging run cannot be used for data correction. This may be compensated for in postcruise processing by using data acquired at the bottom of the hole and comparing the downlog data to the undisturbed parts of the uplog data. Nevertheless, these problems only appear within sharp defined regions, and the data quality in the unaffected areas is good.

Two data sets were retained following logging operations. The first contains the raw data from the GBM, and the second contains the calibrated magnetic flux density over depth. These data were depth corrected to the susceptibility from the triple combo tool string and split into vertical and horizontal components using the inclinometer data (Figure **F90**).

Figure F90. Summary of magnetic flux densities obtained with the Göttingen Borehole Magnetometer and comparison with magnetic susceptibility obtained by logging. IGRF = International Geomagnetic Reference Field.

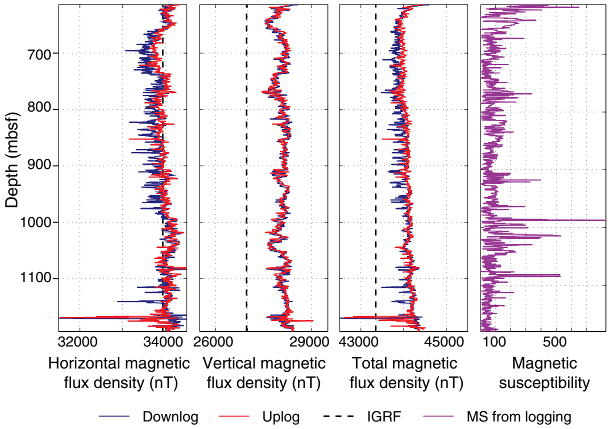

Self-potential and resistivity

Self potential

Self-potential (SP) data repeat between the different logging passes, display major variations in Hole U1438F at the transitions between units, and are inversely correlated with resistivity indicative of good quality measurements. SP data are high and constant within logging Unit 2; these values are considered the baseline for other measurements (Figure **F80**). At 310 mbsf, SP decreases by about 40 mV and stays at this level to 385 mbsf, where an increase of about 20 mV occurs. At ~510 mbsf, SP data show an increasing trend and reach values 20 mV above the baseline. In Hole U1438E, SP data do not display meaningful variations, except between 1100 and 1200 mbsf, where a large decrease is observed.

Resistivity

Resistivity data were obtained in the three logged holes and range from 1.5 to 10.0 Ωm (Figure **F80**). The data show good agreement and an overall increasing trend with depth. Logging Unit 1 displays the lowest resistivity measured for the site (average = ~1.8 Ωm). The transition between logging Units 2 and 3 is characterized by a large increase in resistivity up to an average of 3.5 Ωm. At 399 mbsf, resistivity values are lower (~2 Ωm). From 580 to 1200 mbsf, values increase again and show intervals of low and high values that might be related to the alternating, normally size graded layers described in cores (see **Lithostratigraphy**).

Formation MicroScanner Images

FMS images reveal differences in textures and lithology throughout Hole U1438F. Bedding has been observed and picked, allowing determination of the orientation of structures observed in the resistivity images (Figure **F91**). The FMS images contain meter-scale alternations of high- and low-resistivity units. All alternations correlate well with resistivity data from the triple combo and can be related to changes in lithology. To 310 mbsf, the sediments appear

Figure F91. Examples of dynamically processed FMS images, Hole U1438F.

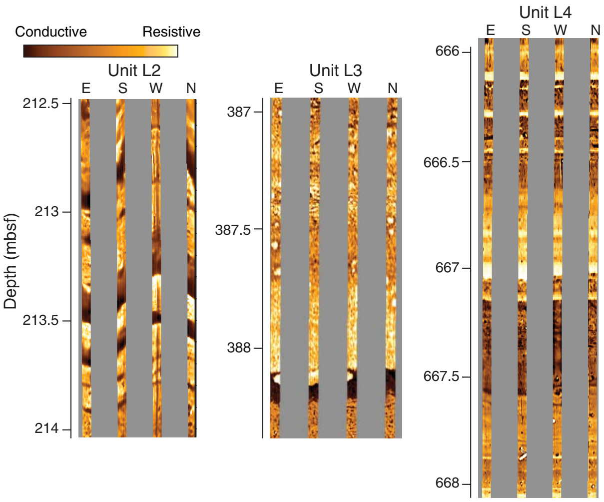

to be more conductive and display few features. FMS images of deeper intervals show that the sediments are more resistive, with very resistive layers that might relate to sand or ash. Some clasts are also visible in this interval. Dipping beds are observed from 206 to 300 mbsf. Deeper than 300 mbsf, the sediments are very resistive and are more or less horizontally bedded. The beds are several meters in height and show a gradation within them from very resistive layers at the bottom to more conductive at the top.

References

Acton, G.D., Okada, M., Clement, B.M., Lund, S.P., and Williams, T., 2002. Paleomagnetic overprints in ocean sediment cores and their relationship to shear deformation caused by piston coring. *Journal of Geophysical Research: Solid Earth,* 107(B4):2067–2081. **http://dx.doi.org/10.1029/2001JB000518**

Arculus, R.J., Ishizuka, O., Bogus, K., Drab, L., Aljahdali, M.H., Bandini-Maeder, A.N., Barth, A.P., Brandl, P.A., do Monte Guerra, R., Gurnis, M.C., Hamada, M., Hickey-Vargas, R.L., Jiang, F., Kanayama, K., Kender, S., Kusano, Y., Li, H., Loudin, L.C., Maffione, M., Marsaglia, K.M., McCarthy, A., Meffre, S., Morris, A., Neuhaus, M., Savov, I.P., Sena Da Silva, C.A., Tepley, F.J., III, van der Land, C., Yogodzinski, G.M., and Zhang, Z., 2015a. Expedition 351 methods. *In* Arculus, R.J., Ishizuka, O., Bogus, K., and the Expedition 351 Scientists, *Proceedings of the International Ocean Discovery Program, Expedition 351: Izu-Bonin-Mariana Arc Origins:* College Station, TX (International Ocean Discovery Program). **http://dx.doi.org/10.14379/iodp.proc.351.102.2015**

Arculus, R.J., Ishizuka, O., Bogus, K., Drab, L., Aljahdali, M.H., Bandini-Maeder, A.N., Barth, A.P., Brandl, P.A., do Monte Guerra, R., Gurnis, M.C., Hamada, M., Hickey-Vargas, R.L., Jiang, F., Kanayama, K., Kender, S., Kusano, Y., Li, H., Loudin, L.C., Maffione, M., Marsaglia, K.M., McCarthy, A., Meffre, S., Morris, A., Neuhaus, M., Savov, I.P., Sena Da Silva, C.A., Tepley, F.J., III, van der Land, C., Yogodzinski, G.M., and Zhang, Z., 2015b. Expedition 351 summary. *In* Arculus, R.J., Ishizuka, O., Bogus, K., and the Expedition 351 Scientists, *Proceedings of the International Ocean Discovery Program, Expedition 351: Izu-Bonin-Mariana Arc Origins:* College Station, TX (International Ocean Discovery Program). **http://dx.doi.org/10.14379/iodp.proc.351.101.2015**

Bolli, H.M., and Saunders, J.B., 1985. Oligocene to Holocene low latitude planktic foraminifera. *In* Bolli, H.M., Saunders, J.B., and Perch-Nielsen, K. (Eds.), *Plankton Stratigraphy* (Vol. 1): *Planktic Foraminifera, Calcareous Nannofossils and Calpionellids:* Cambridge, UK (Cambridge University Press), 155–262.

Cande, S.C., and Kent, D.V., 1995. Revised calibration of the geomagnetic polarity timescale for the Late Cretaceous and Cenozoic. *Journal of Geophysical Research: Solid Earth,* 100(B4):6093–6095. **http://dx.doi.org/10.1029/94JB03098**

Cardozo, N., and Allmendinger, R.W., 2013. Spherical projections with OSXStereonet. *Computers & Geosciences,* 51:193–205. **http://dx.doi.org/10.1016/j.cageo.2012.07.021**

Egeberg, P.K., and the Leg 126 Shipboard Scientific Party, 1990. Unusual composition of pore waters found in the Izu-Bonin forearc sedimentary basin. *Nature,* 344(6263):215–218.

Fisher, R.A., 1953. Dispersion on a sphere. *Proceedings of the Royal Society of London, Series A,* 217:295–305.

Gieskes, J.M., and Lawrence, J.R., 1981. Alteration of volcanic matter in deep-sea sediments: evidence from the chemical composition of interstitial waters from deep sea drilling cores. *Geochimica Cosmochimica Acta,* 45(10):1687–1703. **http://dx.doi.org/10.1016/0016-7037(81)90004-1**

Gradstein, F.M., Ogg, J.G., Schmitz, M.D., and Ogg, G.M. (Eds.), 2012. *The Geological Time Scale 2012:* Amsterdam (Elsevier).

Hawkesworth, C.J., and Elderfield, H., 1978. The strontium isotopic composition of interstitial waters from Sites 245 and 336 of the Deep Sea Drilling Project. *Earth and Planetary Science Letters,* 40(3):423–432. **http://dx.doi.org/10.1016/0012-821X(78)90165-6**

Holbourn, A., Henderson, A.S., and MacLeod, N., 2013. *Atlas of Benthic Foraminifera:* Chichester (John Wiley & Sons, Ltd.). **http://dx.doi.org/10.1002/9781118452493**

Ishizuka, O., Tani, K., Reagan, M.K., Kanayama, K., Umino, S., Harigane, Y., Sakamoto, I., Miyajima, Y., Yuasa, M., and Dunkley, D.J., 2011. The timescales of subduction initiation and subsequent evolution of an oceanic island arc. *Earth and Planetary Science Letters,* 306(3–4):229–240. **http://dx.doi.org/10.1016/j.epsl.2011.04.006**

Jenner, F.E., and O'Neill, H.St.C., 2012. Analysis of 60 elements in 616 ocean floor basaltic glasses. *Geochemistry, Geophysics, Geosystems,* 13(2):Q02005. **http://dx.doi.org/10.1029/2011GC004009**

Japan National Oil Corporation, 1998. *Technology Research Center Report: Deep Sea Survey Technologies for Natural Resources.* (in Japanese).

Kaiho, K., 1992. Eocene to Quaternary benthic foraminifers and paleobathymetry of the Izu-Bonin arc, Legs 125 and 126. *In* Taylor, B., Fujioka, K., et al., *Proceedings of the Ocean Drilling Program, Scientific Results,* 126: College Station, TX (Ocean Drilling Program), 285–310. **http://dx.doi.org/10.2973/odp.proc.sr.126.137.1992**

Kennett, J.P., and Srinivasan, M.S., 1983. *Neogene Planktonic Foraminifera: A Phylogenetic Atlas:* Stroudsburg, PA (Hutchinson Ross).

Marsaglia, K.M., and Tazaki, K., 1992. Diagenetic trends in Leg 126 sandstones. *In* Taylor, B., Fujioka, K., et al., *Proceedings of the Ocean Drilling Program, Scientific Results,* 126: College Station, TX (Ocean Drilling Program), 125–138. **http://dx.doi.org/10.2973/odp.proc.sr.126.123.1992**

Martini, E., 1971. Standard Tertiary and Quaternary calcareous nannoplankton zonation. *In* Farinacci, A. (Ed.), *Proceedings of the Second Planktonic Conference, Roma 1970:* Rome (Edizioni Tecnoscienza), 2:739–785.

Pälike, H., Lyle, M.W., Nishi, H., Raffi, I., Ridgwell, A., Gamage, K., Klaus, A., Acton, G., Anderson, L., Backman, J., Baldauf, J., Beltran, C., Bohaty, S.M., Bown, P., Busch, W., Channell, J.E.T., Chun, C.O.J., Delaney, M., Dewangan, P., Dunkley Jones, T., Edgar, K.M., Evans, H., Fitch, P., Foster, G,L., Gussone, N., Hasegawa, H., Hathorne, E.C., Hayashi, H., Herrle, J.O., Holbourn, A., Hovan, S., Hyeong, K., Iijima, K., Ito, T., Kamikuri, S., Kimoto, K., Kuroda, J., Leon-Rodriguez, L., Malinverno, A., Moore, T.C., Jr., Murphy, B.H., Murphy, D.P., Nakamura, H., Ogane, K., Ohneiser, C., Richter, C., Robinson, R., Rohling, E.J., Romero, O., Sawada, K., Scher, H., Schneider, L., Sluijs, A., Takata, H., Tian, J., Tsujimoto, A., Wade, B.S., Westerhold, T., Wilkens, R., Williams, T., Wilson, P.A., Yamamoto, Y., Yamamoto, S., Yamazaki, T., and Zeebe, R.E., 2012. A Cenozoic record of the equatorial Pacific carbonate compensation depth. *Nature,* 488(7413):609–614. **http://dx.doi.org/10.1038/nature11360**

Pearson, P.N., Olsson, R.K., Huber, B.T., Hemleben, C., and Berggren, W.A. (Eds.), 2006. *Atlas of Eocene Planktonic Foraminifera.* Special Publication - Cushman Foundation for Foraminiferal Research, 41.

Reagan, M.K., Ishizuka, O., Stern, R.J., Kelley, K.A., Ohara, Y., Blichert-Toft, J., Bloomer, S.H., Cash, J., Fryer, P., Hanan, B.B., Hickey-Vargas, R., Ishii, T., Kimura, J.-I., Peate, D.W., Rowe, M.C., and Woods, M., 2010. Fore-arc basalts and subduction initiation in the Izu-Bonin-Mariana system. *Geochemistry, Geophysics, Geosystems,* 11(3):Q03X12. **http://dx.doi.org/10.1029/2009GC002871**

Salisbury, M.H., Shinohara, M., Richter, C., et al., 2002. *Proceedings of the Ocean Drilling Program, Initial Reports,* 195: College Station, TX (Ocean Drilling Program). **http://dx.doi.org/10.2973/odp.proc.ir.195.2002**

Salisbury, M.H., Shinohara, M., Suetsugu, D., Arisaka, M., Diekmann, B., Januszczak, N., and Savov, I.P., 2006. Leg 195 synthesis: Site 1201—a geological and geophysical section in the West Philippine Basin from the 660-km discontinuity to the mudline. *In* Shinohara, M., Salisbury, M.H., and Richter, C. (Eds.), *Proceedings of the Ocean Drilling Program, Scientific Results,* 195: College Station, TX (Ocean Drilling Program), 1–27. **http://dx.doi.org/10.2973/odp.proc.sr.195.113.2006**

Savov, I.P., Hickey-Vargas, R., D'Antonio, M., Ryan, J., and Spadea, P., 2005. Petrology and geochemistry of west Philippine basin basalts and early Palau-Kyushu arc volcanic clasts from ODP Leg 195, Site 1201D: implications for the early history of the Izu-Bonin-Mariana arc. *Journal of Petrology,* 47(2):277–299. **http://dx.doi.org/10.1093/petrology/egi075**

Tauxe, L., and Kent, D.V., 2004. A simplified statistical model for the geomagnetic field and the detection of shallow bias in paleomagnetic inclinations: was the ancient magnetic field dipolar? *In* Channell, J.E.T., Kent, D.V., Lowrie, W., and Meert, J.G. (Eds.), *Timescales of the Paleomagnetic Field.* Geophysical Monograph, 145:101–115. **http://dx.doi.org/10.1029/145GM08**

Teagle, D.A.H., Ildefonse, B., Blum, P., and the Expedition 335 Scientists, 2012. *Proceedings of the Integrated Ocean Drilling Program*, 335: Tokyo (Integrated Ocean Drilling Program Management International, Inc.). **http://dx.doi.org/10.2204/iodp.proc.335.2012**

Thompson, R., and Oldfield, F., 1986. *Environmental Magnetism:* London (Allen and Unwin).

Torres, M.E., Marsaglia, K.M., Martin, J.B., and Murray, R.W., 1995. Sediment diagenesis in western Pacific basins. *In* Taylor, B., and Natland, J. (Eds.), *Active Margins and Marginal Basins of the Western Pacific.* Geophysical Monograph, 88:241–258. **http://dx.doi.org/10.1029/GM088p0241**

van Morkhoven, F.P.C.M., Berggren, W.A., Edwards, A.S.,and Oertli, H.J., 1986. Cenozoic cosmopolitan deep-water benthic foraminifera. *Bulletin des Centres de Recherches Exploration-Production Elf-Aquitaine,* 11.

Wei, W., Kastner, M., and Spivack, A., 2008. Chlorine stable isotopes and halogen concentrations in convergent margins with implications for the Cl isotopes cycle in the ocean. *Earth and Planetary Science Letters,* 266(1–2):90–104. **http://dx.doi.org/10.1016/j.epsl.2007.11.009**